Declaration

I confirm that this is my own work and the use of all material

from other sources has been properly and fully acknowledged.

(AZIM ZALIHA BINTI ABD AZIZ)

Acknowledgement

In the name of God

First and foremost I am forever grateful to my beloved husband, Mohd. Rizon Juhari, who instilled in me the love for knowledge and wisdom, who has been with me through thick and thin. To my dearest son, Adrian Iqbal Alfariz, I may not have everything in life but I am blessed enough to have you by my side throughout this journey. You are my pillar of strength and without you I would not have had the courage and conviction to pursue this journey.

To my beloved mother, Ramlah Shariff, thank you for teaching me all the attributes that I needed during the most difficult times of my journey. To my late father, Abd Aziz Abd Rahim, who through his conduct, taught me the meaning of patience, perseverance and inner strength. To my late brother, Aizi Rafeezul, your love and spirit will always be in my heart. May Allah bless the two of you, *Abah* and *Abang*. To my sisters, Azim Zuliana, Ainal Marziah and Ainal Amirah, thank you for your words of encouragement, moral support and prayers.

To Dr Hong Wei, my supervisor, who supported me with her knowledge, expertise and dedication throughout the whole course of my PhD. Thank you for believing in me at times when I myself did not have such confidence in my abilities.

To all my families and friends, thank you for listening to all my woes, frustrations, and also my excitements. Thank you for your love and encouragement.

Abstract

Computer vision is an image understanding discipline that studies how to reconstruct, interpret and understand a 3D scene from its 2D images. One of the goals is to automate the analysis of images through the use of computer software and hardware. Meanwhile, biometrics refer to the automated authentication process that rely on measureable physical characteristics such as individual's unique fingerprints, iris, face, palmprint, gait and voice. Amongst these biometric identification schemes, face biometric is said to be the most popular where face authentication systems have been rapidly developed mainly for security reasons. However, the resistance of face biometric system to spoofing attack, which is an act to impersonate a valid user by placing fake face in front of the sensor to gain access, has become a critical issue. Thus, anti-spoofing technique is required to counter the attacks.

Different materials have their own reflection properties. These reflection differences have been manipulated by researches for particular reasons such as in object classification. Many ways can be used to measure the reflection differences of each object. One of them is by using polarised light. Since none of the existing studies applied polarised light in face spoofing detection, therefore in this thesis, polarisation imaging technique was implemented to distinguish between genuine face and two types of spoofing attacks: printed photos and iPad displayed faces. From the investigations, several research findings can be listed. Firstly, unpolarised visible light could not be used in a polarisation imaging system to capture polarised images for designated purpose. Secondly, polarised light is able to differentiate between surface and subsurface reflections of real and fake faces. However, both of these reflections could not be used as one of the classification methods between real face and printed photos. Thirdly, polarised image could contribute to enhance the performance of face recognition system against spoofing attacks in which the newly proposed formula, SDOLP3F achieves higher accuracy rate. Next, near infrared (NIR) light in a polarisation imaging system do not provide significant differences between real face and the two face attacks.

Apart from polarised spoofing face detection analysis, experiments to investigate the accuracy of depth data captured by three depth sensors was carried out. This investigation was conducted due to the concerns over the stability of the depth pixels involved in 3D spoofing face reconstruction in a publicly available spoofing face database known as 3DMAD. From the analysis, none of the three depth sensors which are the Kinect for Xbox 360, Kinect for

Windows version 2.0 and Asus Xtion Pro Live are suitable for 3D face reconstruction for the purpose of spoofing detection due to the potential errors made by the fluctuated pixels.

As a conclusion, polarisation imaging technique has the potential to protect face biometric system from printed photos and iPad displayed attacks. Further investigations using the same polarised light approach could be carried out on other future work as proposed at the end of this thesis.

Table of Contents

List of Tables

List of Figures

List of Abbreviations

2D	:	Two dimensional
3D	:	Three dimensional
AC	:	Accuracy rate
BC	:	Bimodality coefficient
DOP	:	Degree of polarisation
F_0	:	Genuine face polarised image at 0^0 polarisation angle
F_{45}	:	Genuine face polarised image at 45^0 polarisation angle
F_{90}	:	Genuine face polarised image at 90^0 polarisation angle
F_{135}	:	Genuine face polarised image at 135^0 polarisation angle
F_{pol}	:	Genuine face polarisation image
FaPs	:	Face-Photo-Spoof dataset
FPR	:	False positive rate
HDS	:	Hartigan's dip statistic
I_{max}	:	Image with maximum intensity
I_{min}	:	Image with minimum intensity
I_{pol}	:	Polarisation image
I_{SDOLP}	:	Stokes degree of linear polarisation image
iP_0	:	iPad displayed face polarised image at 0^0 polarisation angle
iP_{45}	:	iPad displayed face polarised image at 45^0 polarisation angle
iP_{90}	:	iPad displayed face polarised image at 90^0 polarisation angle
iP_{135}	:	iPad displayed face polarised image at 135^0 polarisation angle
iP_{pol}	:	iPad displayed face polarisation image
kt	:	Kurtosis
mn	:	Mean
mod	:	Density of distribution mode
n	:	Sample size
NIR	:	Near infrared
nm	:	Nanometres
P_1	:	Polariser 1
P_2	:	Polariser 2
P_3	:	Polariser 3

$px_1 - px_{12}$	:	Depth pixels
PDF	:	Probability density function
PF_{pol}	:	Printed photo face polarisation image
RGB	:	Red green blue image format
R_1	:	Genuine face of subject 1 under preliminary experiments
R_2	:	Genuine face of subject 2 under preliminary experiments
R_{sur}	:	Surface reflection
R_{dif}	:	Diffuse reflection
SDOLP	:	Stokes degree of liner polarisation
SDOLP3F	:	Stokes degree of liner polarisation fast fusion formula
sk	:	Skewness
S_0	:	Stokes component 1
S_1	:	Stokes component 2
S_2	:	Stokes component 3
th	:	Threshold
TPR	:	True positive rate
$\bar{x}$	:	Mean intensity
σ	:	Standard deviation
α	:	SDOLP3F component

Chapter 1: Introduction

1.1 Biometrics Face Recognition System

Computer vision is an image understanding discipline that studies how to reconstruct, interpret and understand a three-dimensional (3D) scene from its two-dimensional (2D) images. One of the goals is to automate the analysis of images through the use of computer software and hardware. Generally, automation can improve image analysis performances, reduce operating costs and also improve safety in some applications. For instance, a large number of images from a 24 hour security surveillance system at an airport will take time to be manually analysed. Therefore, computer vision applications are indispensable to assist in analysing images. There are several steps to analyse computer-based images. Firstly, standard 2D images are captured from the 3D world by using digital devices such as digital camera, tablet or mobile phone. Secondly, the recorded images are processed using computer software to reduce the input data and build informative features. The extracted features are then manipulated in various applications, for example face or object recognition analysis within the world of biometric community.

Biometrics refer to the automated recognition of individuals based on their physiological and/or behavioural characteristics [Jain et al. (2004)]. Examples of biometric characteristics are deoxyribonucleic acid (DNA), ear, face, fingerprint, gait, iris, keystroke, odour, palmprint, retinal scan, signature and voice. Each of the characteristics has its own strengths and weaknesses. The choice of a biometric trait depends on the purpose of the biometric application. Biometric traits are generally inherent to an individual, thus can be used to identify individuals in a biometric system. For instance, fingerprint verification system is usually used to gain access to premises, whereas iris or face recognition is mostly applied in verification system such as border access control for security and immigration. Due to the high demand on these biometric applications, fingerprint, face and iris have been the three most popular and mature modalities among the others [Jain et al. (2016)]. Moreover, the availability

of large fingerprint, iris and face databases, which have been collected by various agencies all over the world, has also led to the demand.

In the history of biometric research, face is the second largest deployed biometric at world level in terms of market quota right after fingerprints [Galbally et al. (2014)]. In addition, face biometric trait is said to have the highest impact from an economic and a social point of view. Thus, automatic face authentication systems have been rapidly developed mainly for security reasons. However, the resistance of this rapidly emerging technology to external attacks has become a critical issue. In particular, spoofing is an attack where photograph, video or mask of a valid user is presented in front of a face recognition system as trial to gain access. The number of spoofing attacks on face recognition system has become a huge concern among the biometric community. In this scenario, the face biometric data of a valid user can be easily obtained without physical contact either by capturing using a camera or by downloading through the internet [Bagga and Singh (2016)].

Facial recognition systems can be classified into two categories: 2-dimensional (2D) and 3-dimensional (3D) face recognition systems [Nixon et al. (2008)]. 2D face recognition systems process two-dimensional face image, while 3D facial recognition systems require complex technique such as patterned illumination light to develop a 3D face representation. Spoofing attacks toward 2D facial recognition systems could be in the simplest form either by using a photograph or image displayed on a portable screen. 3D sensing is said to have better protection against spoof attempts since the attacks must be in three dimensional form such as a 3D face mask. Face recognition systems can be conventionally spoofed by presenting a photograph, playing a video or wearing a 3D face mask of a genuine user in front of the sensor [Biggio et al. (2012)]. Moreover, photograph and video representations are the most common, cheapest and easiest spoofing attacks to deceive face recognition systems [Chakka et al. (2011)]. Countering these face biometric attacks are vital to avoid impostors from gaining access to any security or biometric systems.

1.2 Face Spoofing Countermeasures

An anti-spoofing technique is a method used to distinguish between authentic user and fake trait. Biometric face anti-spoofing techniques may be classified into three categories: (1) sensor-level techniques; (2) feature-level techniques; and (3) score-level techniques [Bagga and Singh (2016)]. The sensor-level techniques are basically hardware-based techniques in which some specific devices are added to these methods. The hardware-based approaches generally measure one of three characteristics: intrinsic properties (e.g., physical properties); signals of a living body (e.g., pulse, blood pressure); and responses to external stimuli given to the user. The feature-level techniques are also known as software-based techniques. In these methods, the image of a face is firstly captured by a biometric sensor. Features of the image are extracted and subsequently used to differentiate between genuine and fake faces. The third category, which is the score-level techniques suggests fusion strategies to enhance the performance of the sensor-level and feature-level techniques. The score-level methods are much less common as compared to the sensor-level and feature-level techniques [Galbally et al. (2014)]. Figure 1.1 presents the general classification of face anti-spoofing techniques.

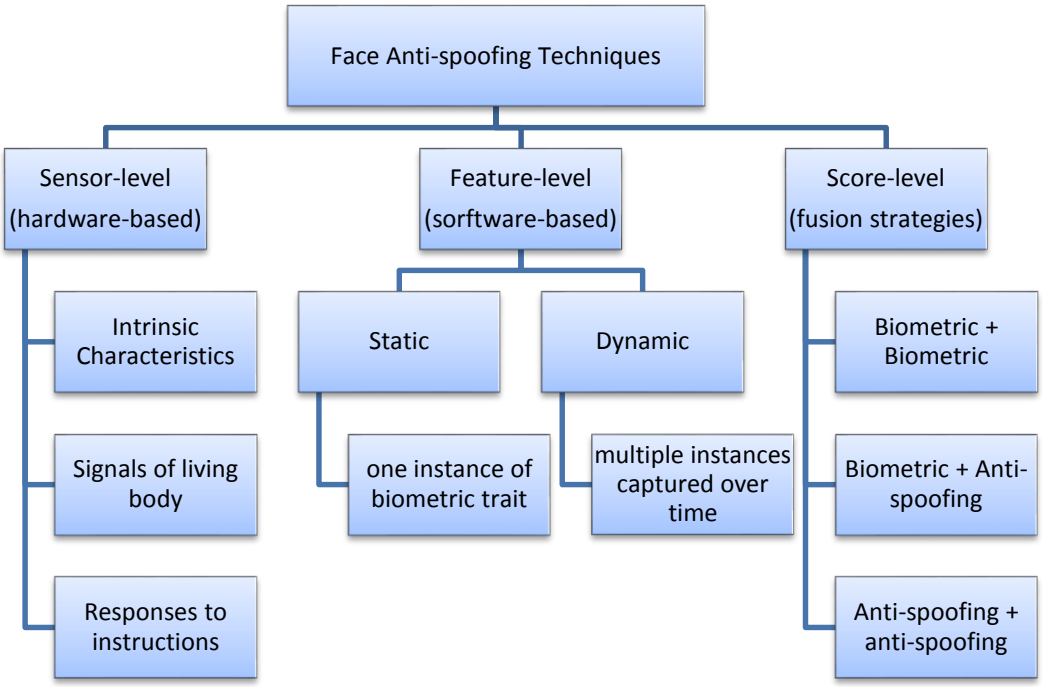

Figure 1.1: The general classification of spoofing countermeasure techniques

Present studies on face anti-spoofing methods can be classified into one of these categories depending on the purpose of the proposed techniques. Hardware-based techniques require additional devices to be attached to the sensor in order to detect particular signs as listed above. For instance, a device can be attached to the sensor to detect blood pressure or heart beats. Other than the cost factor, sensor-level methods also require the user to be very cooperative. Meanwhile, the score-level techniques proposed fusion strategies to increase the level of resistance against spoofing attacks. Score-level techniques are designed to support sensor-level and feature-level techniques [Galbally et al. (2014)]. Software-based or feature-level methods are the most popular anti-spoofing techniques among the face biometric community due to the highest number of studies compared with the other two techniques.

Basically, feature-level spoofing countermeasures attempt to detect genuine users based on several analyses. Akhtar and Foresti (2016) pointed out that anti-spoofing techniques can be classified into three categories: (1) motion based methods; (2) texture based methods; and (3) hardware based methods. Määttä et al. (2012) claimed that the countermeasure methods are based on four categories: (1) liveness based analysis; (2) motion based analysis; (3) texture and reflectance based analysis; and (4) multi-modal analysis. Other than that, Bagga and Singh (2016) concluded four types of anti-spoofing techniques: motion based, texture based, life sign detection based and optical flow based techniques. Although there are various categories that have been made to classify anti-spoofing techniques, it can be concluded that the countermeasures belong to four main categories, which are motion-based analysis, texture-based analysis, reflectance-based analysis and other cues-based analysis.

Motion-based method analyse liveness signs such as head movement, eye blinking or lips movement to detect genuine faces. Texture-based analysis examines skin texture under assumption that skin textures of real faces such as pigments and surface geometry, are different from the spoof attacks. The differences of reflection properties among materials have been used as a cue in reflectance-based technique. The fourth category includes spoofing countermeasures that fall outside the first three categories, for instance the optical flow field and image distortion analyses. Despite the great amount of research that have been carried out to counter spoofing attacks, it is hard to select one technique over the other as the most resistant countermeasure against spoofing attempts on face recognition systems.

Generally, the process of distinguishing genuine and fake faces is similar to object classification process. Reflectance properties of each object surfaces may be used as cue to differentiate between them. In reflectance-based object recognition systems, one of the methods that could be implemented to classify between two different objects is by using polarized light. Polarisation is a unique characteristic of transverse wave in which the phenomenon of vibration and propagation directions are asymmetry [Zhao et al. (2016)]. A considerable amount of literature on polarization technique to distinguish between: (1) metal and dielectric surfaces [Sarkar et al. (2011), Wolff (1990)]; and (2) transparent and opaque objects [Mahendru and Sarkar (2012)]. Several parameters such as the Fresnel coefficients, the Stokes parameters and the degree of polarization was applied in the studies mentioned to measure the differences. However, the impact of polarization imaging on the degree of polarization for human skin is not yet clear.

Human skin consists of various layers structures which contribute to the production of multiple reflections: surface and subsurface (diffuse) reflections. Polarized light is one of the methods that could be used to differentiate between the two reflections. In the world of cosmetic, reflections are separated to classify the age skin groups [Matsubara (2012)]. Other than that, polarization technique has also been applied on human skin analysis in the field of biomedical in order to study several types of skin diseases by splitting the two reflections [Jacques et al. (2002), Bin et al. (2007)]. Although extensive research has been carried out, no single study has been done by the face biometric research community which apply the polarization classification technique to distinguish between real human face and spoofing attacks.

Since 2D face recognition systems have been regularly attacked by photograph or video display, the reflection properties of both spoof traits could be a cue to counter the attacks. Photo attack is usually a printed photo on a piece of paper while video display attack is executed by displaying a video sequence on a device such as laptop, tablet or hand phone. The question whether the surface or subsurface reflection can be used to classify between genuine faces, photographs and video displays will be determined by the polarization method. The second issue to be highlighted is the degree of polarization owned by genuine faces and fake faces. To measure the degree of polarization, the Stokes parameters and the degree of polarization may be applied as the parameters. The details of these two measurements will be

explained in the next chapter. Other than that, it is interesting to investigate on the effects of using NIR polarization on the degree of polarization for all subjects.

Another issue to be pointed out is the use of 3D face mask against 2D, 2.5D or 3D face recognition systems. A 3D face mask which mimics a real face could easily deceive the systems. Several studies have conducted anti-spoofing techniques against 3D mask attacks on 2D, 2.5D or 3D face recognition systems. Face mask images from a publicly available database known as 3DMAD have been used as spoofing attempts. The images in the database was captured by using a depth sensor, Kinect for XBOX 360. Researchers have analysed the depth data as trials to differentiate between genuine faces and the 3D face masks. Thus, the accuracy of the depth pixels is somewhat doubtful whether it could affect the results. To address this concern, this study focuses on the depth pixels fluctuations captured by various depth sensors.

The aim of this research is to examine the problem of 2D face spoofing attacks on 2D face recognition systems. The methodological approach taken in this study is based on the reflectance properties by using polarization images. This proposed method is believed to handle various types of spoofing attacks other than printed photo paper and iPad image display.

1.3 Research Questions

Motivated by the listing issues in Section 1.2, this thesis intends to distinguish between genuine facial skin and other materials as protection from face recognition systems against spoofing attacks. Particularly, this study will examine five main research questions:

1. What are the effects of using normal visible light on a polarisation imaging system in which a polarizer is mounted only in front of the camera lens on the degree of polarisation among the genuine and fake faces?

2. What is the impact of using polarized visible light in a polarisation imaging system to separate between the surface and subsurface reflections of each material as one of the classification methods?

3. How do polarised images correlate with the spoofing face detection performance in a face recognition system?

4. What are the effects of implementing polarized near infrared (NIR) light in the polarisation imaging system on polarisation images between genuine faces and non-genuine traits?

5. What is the relationship between multiple versions of depth sensors and the sensor-subject distances with the fluctuations of centre depth pixels and pixels at the edges of the subject?

1.4 Research Methodology

To the best of the author's knowledge, there is no publicly available polarized image database that could be used for the proposed research. Therefore, polarized images for this study were self-collected by using self-developed polarization imaging system located in Virtual Reality Computer Lab, Department of Computer Science University of Reading. Two types of light sources were used (one at a time) which are visible and near infrared lights to investigate the impact on the polarization images. Linear polarizer was mounted in front of each light source and also in front of the camera lens. The linear polarizer in front of the camera lens was coupled with an angle rotator used to adjust the polarization angles during the recording processes. Subjects were randomly selected among members of the department. To create the spoofing attacks, the original image of each subject, which was captured under normal visible light was printed on an A4 matte paper. The second spoofing attempt was carried out by displaying face images of the subjects on an iPad.

By using the degree of polarization (DOP) and the Stokes parameters, two types of images were generated which have been named as I_{pol} and I_{SDOLP}, respectively. These images were then analysed using six measures: the mean, the standard deviation, the kurtosis, the skewness, the bimodality coefficient and the density of the distribution mode. Significant thresholds are assigned to each individual measurement as an indicator for genuine or fake faces. Two of the measures with the highest accuracy rates were selected to be fused in the newly proposed formula known as the Stokes degree of linear polarization fast fusion formula (SDOLP3F). The scores of the SDOLP3F indicate which one are the real faces or the spoofing attacks. Figure 1.2 illustrates the proposed anti-spoofing face detection framework.

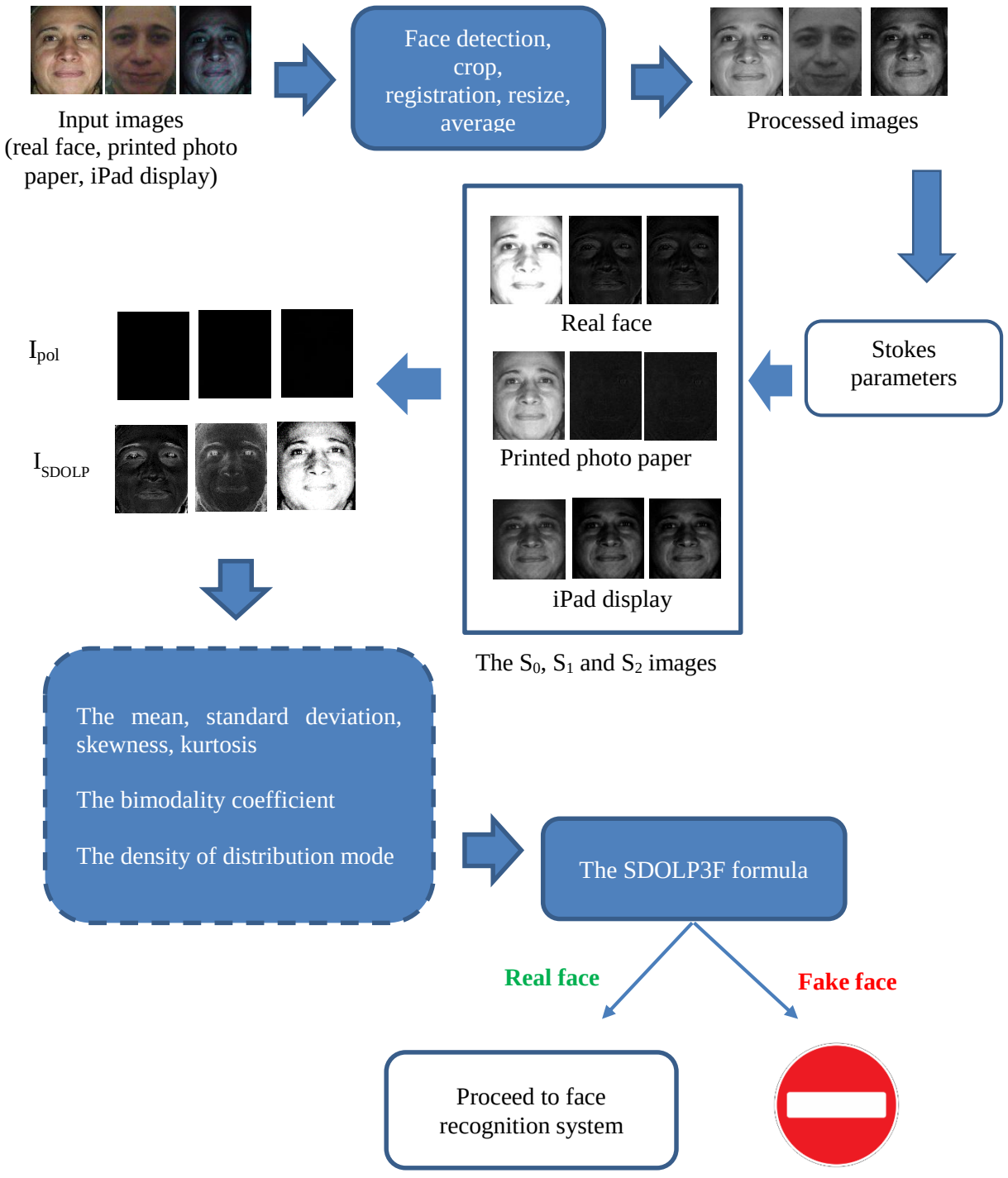

Figure 1.2: The proposed anti-spoofing face detection framework

1.5 Thesis structure

This study provides an exciting opportunity to advance the knowledge of the advantages of polarised reflectance as one of the face anti-spoofing methods. It is beyond the scope of this study to examine the 3D mask attacks on face recognition systems due to unavailability of polarised 3D face mask database. Apart from that, the number of subjects involved in self-collected polarisation dataset throughout this thesis is relatively small with only 37 participants. This thesis is composed of seven themed chapters, including this introductory chapter. Chapter Two begins by laying out the theoretical dimensions of the research, and looks at how previous investigations were carried out to counter the face spoofing attacks. An introduction to polarised image, polarisation angles, polarisation axes and polarisation imaging system is presented in Chapter Three. Apart from that, two parameters used in the analysis throughout this thesis which are the Stokes parameters and the degree of polarisation (DOP) are also introduced in Chapter Three. Before proceeding to spoofing face detection using polarised light in a polarisation imaging system, preliminary experiments which used unpolarised visible light source were carried out and explained in Chapter Three. The aim of these experiments was to investigate the impact of using unpolarised light source in a polarisation imaging system on spoofing face detection.

Chapter Four presents the findings of this research, focusing on the three key themes: (a) differences of surface and subsurface images between the subjects; (b) polarisation images as the classification parameter between real and fake subjects; and (c) newly proposed fusion formula at score level to distinguish between the materials. The findings in this chapter proved that polarised light source is a requirement in a polarisation imaging system for designated purposes. As in this study, the aim is to detect two types of spoofing face attacks: printed photos and iPad displayed faces. In Chapter 5, further research was conducted by using a single wavelength polarised light source or also known as near infrared (NIR) light in a polarisation imaging system. By using NIR light with 850 nanometre (nm) wavelength, images of genuine subjects and spoofing faces were recorded. These images were analysed based on the same three approaches as in Chapter 4. Surprisingly, polarised images captured under NIR polarised light do not provide significant differences between real and fake faces.

Chapter 6 presents analysis on the accuracy of depth pixels recorded by three different versions of depth sensors: (1) Microsoft Kinect for Xbox 360; (2) Microsoft Kinect for

Windows version 2; and (3) ASUS Xtion Pro Live. The analysis in this chapter was carried out due to the existence of 3D face spoofing database used to attack face biometric system. The images of 3D fake faces in the database were recorded using one of the depth sensors. The database has been used by researchers particularly in studies to differentiate between real and spoofing faces. Thus, the accuracy of the depth data has become the main concern which triggering the experiments throughout Chapter 6. The results conclude that none of the three depth sensors are suitable for 3D face reconstruction for the purpose of spoofing detection due to the potential errors made by the fluctuated pixels.

The final chapter draws upon the entire thesis, tying up the various theoretical strands in order to propose a polarization method to combat the spoofing attacks on face recognition systems, and includes a discussion of the implication of the findings to future research into the area of anti-spoofing face detection techniques.

Chapter 2: Literature Review

2.1 Face Spoofing Countermeasures

There is a large volume of published studies describing the role of anti-spoofing techniques to reduce spoofing impact on face recognition performances. Feature-level technique is the most popular spoofing countermeasure method compared to sensor-level and score-level techniques based on the number of published studies. Conventionally, feature-level face spoofing countermeasures can be classified into three main categories: motion-based analysis, texture-based analysis and reflectance-based analysis. Motion-based spoof countermeasure analyse liveness signs of subjects such as eye blinking and lip movements in order to classify between real and fake traits. The texture-based analysis differentiates between genuine face and fake face based on the texture features such as surface geometry. It is assumed that the texture features produced by fake face will definitely be different than the texture features generated by the real face. While reflectance-based analysis examines the reflection disparity between genuine face and spoof attacks.

2.1.1 Motion-based countermeasures

Two-dimensional (2D) face recognition system process 2D face images. Thus, spoofing attacks toward the 2D facial recognition system could be in the form of photograph or video display of a valid user. Several attempts have been carried out to defend the face recognition system against spoofing attempts by checking on liveness or motion signs. Frischholz and Werner (2003) introduced a head pose estimation technique on a single camera input. A genuine subject was required to move his head accordance with the designated direction by the system. It has been proven that a photograph failed to respond to the challenged-response test. This technique, however, requires full cooperation of the subjects and also time consuming.

Eye blinks are another sign of liveness that could be used to differentiate between genuine face and fake face traits. To detect a movement sign on a genuine user, Jee et al. (2006) conducted a method to detect eyes in image sequence. Firstly, the centre point of each eye was

detected then the face region was normalized. The eye regions were binarized and compared between the image sequences. The variation was calculated using Hamming distance method to determine whether it is a real face or a photograph attack. Another similar study was carried out by Pan et al. (2007) by adopting eye-blinks as a clue for anti-spoofing. Pan et al. (2007) modelled eye-blinks behaviour of 20 individuals in order to differentiate between facial photograph and live subjects. However, anti-spoofing techniques based on eye blinks may not work on a video attack where the action of eye blinking can be recorded and displayed in front of the camera as a mean of spoofing. In addition, the face recognition systems could be challenged with perforated eyes photograph.

Recently, Singh and Arora (2017) proposed face liveness detection by considering eye-blink and mouth movements. Three datasets were used: ZJU Eyeblink; Print-Attack Replay; and self-developed dataset. Eye-blink indicator was applied to detect liveness faces in the first two datasets. For the self-developed dataset, eye-blink and lips movement have been considered. However, the existing face recognition systems that rely on eye blinks, lips movements and motion analysis, as discussed above are no longer relevant. Liveness detection based on eye blinking and lips movement was deceived using perforated mask in the eyes and mouth. While for motion based counter spoofing, it was challenged with recorded video playback in front of the camera.

2.1.2 Texture-based countermeasures

Texture based analysis is generally faster to classify fake biometric traits [Akhtar and Foresti (2016)]. This method examines the skin texture under assumption that skin textures of real faces such as pigments and surface geometry, are different than the spoof attacks. One study by Määttä et al. (2011) claimed that photo print contains printing quality defects that can be identified by examining the texture of single image to differentiate between a live person and a photo print. They proposed a method which uses multi-scale local binary pattern (LBP) to analyse the micro-texture patterns of facial images. One limitation of this proposed method is the requirement of sharp input image to make the photos look exactly the same as the live subjects.

Schwartz et al. (2011) applied low-level feature descriptors such as shape, colour and texture to detect non-live samples. These features descriptors were integrated with weighting scheme based on the partial least squares (PLS). However, the proposed method suffers from image misalignment which affects the accuracy of spoofing detection. In a study by Wang et al. (2013), a method to counter spoofing attacks was proposed by recovering sparse 3D facial structure. Face images were captured from more than two viewpoints, and then several key frames were selected. The sparse 3D facial structure was recovered from the selected key frames. The results show that photo paper attacks can be detected even if the photo paper is warped vertically or horizontally. This technique, however, needs cooperation from the subjects for the recording process since more than two viewpoints are required.

Singh et al. (2013) suggest a second order gradient based technique to detect genuine faces from a single face image. Two self-developed databases were introduced, which are: (a) real face image database; and (b) fake face image database consisting of a set of dummy face images, colour imposed face images and masked face images. The second order gradient method was applied for feature extraction on all images in both databases. This investigation suffers from the own-developed databases. Firstly, the use of mannequins as the dummy face which do not represent the appearance of real faces. Other than that, the colour imposed and the mask faces databases were developed by applying synthetic colour and tampering cosmetic cream onto the face surface. These materials were not identical to the real skin colour. Thus, the results from the experiments can be disputed.

Boulkenafet et al. (2015) argue that the colour reproduction of fake faces is limited compared to genuine faces. Thus, the authors proposed a spoof countermeasure by analysing images from three different colour spaces: RGB, HSV and YC_bC_r. LBP was used to extract features from the individual image channel. The experiments was carried out using CASIA-FA and Replay-Attack databases which include video attacks, warped photo attacks, and cut photo attacks. The results show that the combination features of HSV and YC_bC_r colour spaces achieve lowest HTER values in Replay-Attack database but the values increased when tested with other databases. Although the proposed method showed excellent results compare with other colour channel images, the technique is not flexible to be applied in various databases as images in each database are captured using different light sources.

Recently, Akhtar and Foresti (2016) highlight the need to find a discriminative and computationally inexpensive features and methods for spoof attacks. A single image was randomly selected from a video sequence. The image was divided into non-overlapping local patches which were then ranked by using seven novel methods: dend-clustering, cluster pairing, cluster space, MAXDIST, IQA, diversity filter and intensity-based patch of interest. Features of the discriminative patches were selected to be fed into classifier to be determined as genuine face or spoof attack. The method requires only one image as an input to the analysis. Although the results show the feasibility to use only certain face image patches instead of whole face image for better classification accuracy rate, the use of only one input image is doubtful. One single image might suffer from noises such as blurriness.

With the deployment of latest technologies, for example the 3D scanners and printing technology, the creation of face masks has become much easier. The facial masks that really mimic the real user faces with duplicate texture features could be produced using materials such as silicone, plastics, resin, rubber or latex Steiner et al. (2016). With the addition of paint or makeup makes the appearance of 3D facial mask nearly identical to a real face. It has become more challenging to classify between genuine faces and the 3D facial masks due to the identical surface properties. Many approaches have been proposed to address the 3D masks attacks. In response to the challenge, Kose and Dugelay (2013b) adopted the multi-scale LBP technique proposed by Määttä et al. (2011), to detect mask attacks using a non-public 3D MORPHO mask spoofing database. The countermeasure was carried out in two parts: on the texture images and on the depth maps. The results showed that both texture and depth characteristics provided enough information to detect mask attacks.

For further verification on the effectiveness of the texture based technique to detect mask attacks in face recognition systems, Kose and Dugelay (2013a) examined the performance evaluation based on three methods which were: a) warping parameters (WP) which uses pre-processed 3D scan shape images (without texture) as input; b) local binary pattern (LBP) which used 2D texture images as input; and local binary pattern-depth (LBP-depth) which utilizes depth maps estimated from the 3D scan shape images as input. The results indicated that LBP applied on texture images was the most robust against mask attacks compared to WP and LBP-depth. Although the results in both studies [Kose and Dugelay (2013a), Kose and Dugelay (2013b)] illustrated the robustness of the LBP texture analysis to distinguish between genuine faces and 3D masks, the number of subjects and masks in the

database was relatively small. There were 20 genuine subjects in which 3D face masks were manufactured for only 16 of the subjects. Apart from that, the material used to create the masks were not discussed which could be an important cue for spoof detection.

Analysis on 3D mask attacks was then carried out by Erdogmus and Marcel (2013). Images from the first publicly available 3D spoofing database known as 3D Mask Attack Database (3DMAD) were used. Local Binary Pattern (LBP) based method was analysed using colour and depth image. The results were then compared with three more LBP extensions: (1) transitional (tLBP); (2) direction-coded (dLBP); and (3) modified (mLBP). The results suggest that per-block based LBP features with LDA provided more accurate results for both colour and depth images. However, the depth images in the 3DMAD database were recorded using a consumer depth sensor in which the accuracy of the depth pixels was uncertain.

The number of studies on 3D face mask anti-spoofing techniques is limited considering the availability of 3D face spoofing database. To the best of the author knowledge, there is only one 3D face spoofing database that is publicly available which is known as 3DMAD. From the discussion above, LBP was applied in the investigations to analyse the texture differences between 3D masks and the genuine faces. With the limitation of the database, different types of approaches to combat 3D mask attacks should be interesting in further studies.

2.1.3 Reflectance-based countermeasures

In addition to the texture-based analysis on 3D face masks, Kose and Dugelay (2013c) carried out an investigation on the surface reflectance of images taken from the spoofing MORPHO 3D masks database. The images were first decomposed into illumination and reflectance components by using variational retinex algorithm proposed by Almoussa (2008). The results reported that the 3D face mask reflectance component is higher than the real face. In addition, the results were compared with the other two countermeasures that have been carried out in previous studies by Kose and Dugelay (2013b). The proposed reflectance-based resulted as the highest accuracy rate among the others.

To detect the existence of human skin in a monitoring area, Kanzawa et al. (2011) employed a method based on spectroscopy, which each substance has its own unique reflection properties. The processing method was divided into two regions: visible light (Vis) and near-infrared (NIR). In visible light region, YC_bC_r colour space was used to specify pixel whose colour is similar as a skin, while in a NIR region, the reflectance difference between images in two different wavelengths is used to determine human skin. Both characteristics of human skin in the Vis and NIR regions were combined as the detection method. One of the limitations with this method was that it did not compare between materials that have similar colour as real human skin.

In a study which set out to distinguish between human faces and mask materials: silicone, latex and skin-gel; Kim et al. (2009) found a stable reflectance disparity at 850 nm wavelength of light. The albedo of the forehead region was measured using both photometric stereo and radiance methods. The reflectance method showed a greater reflectance contrast with a single 2D image compared to photometric stereo method that required many 2D images. Apart from that, cosmetic was found to give minimum effects to the reflectance results. The aim of this study, however, was more to materials classification rather than spoofing detection since the materials used were not in the form of face masks.

Zhang et al. (2011) used near infrared (NIR) light to differentiate between genuine face and face masks: silica gel; rubber; photo; and video replay. Two discriminative wavelengths which are, 850nm and 1450nm was able to classify surface reflectance of the materials. Singh et al. (2013) suggested a second order gradient based technique to detect face tampering from a single face image. Two self-developed databases were introduced: (a) real face image database; and (b) tampered face image database consists of a set of dummy face images, colour imposed face images and masked face images. Although these two studies successfully separated the real face from the other materials, the classification accuracy is doubtful because there was no existence of face mask.

2.1.4 Other cues-based countermeasures

Apart from motion-based, texture-based and reflectance-based anti-spoofing techniques, there are several countermeasures that fall outside these three main categories. One of them is the optical flow field which is the apparent movement of image intensity pattern. Bao et al. (2009) argued that the light in optical flow field generated by movements of three-dimensional genuine face were different compared to the movements generated by two-dimensional objects such as a planar photograph. The optical flow field motion was the sum of four movement types: rotation, translation, moving and swing movements. Another study that apply similar optical flow field technique was proposed by Kollreider et al. (2005). The proposed method measured the trajectories of selected part of the face from the short sequence of images using a simplified optical flow analysis followed by a heuristic classifier. Three regions of genuine faces and photographs were observed: the face centre; the nose and the eyes; and the ears. Although the optical flow field technique showed good classification performances, the method was sensitive to any changes on the illumination. Besides, the techniques were not user-friendly when the user needed to amplify his gestures for detection. In addition, the method assumed that the fake face is on a planar plane thus vulnerable to photo bending attacks.

In 2015, Wen et al. proposed a spoofing countermeasure method based on image distortion analysis (IDA). The spoof images were argued to have major distortions compared to the genuine face images in four types of feature: specular reflection, image blurriness, image chromaticity and colour diversity. These four features were concatenated together which resulted in 121 dimensions of IDA feature vector. The proposed approach performs better than state-of-the-art methods. One year later, Inhan et al. (2016) argued that genuine and spoofing images varied from three perspectives: different light effects; various surface structure; and image distortions. The proposed method distinguished between genuine and fake traits by concatenating three features. Firstly, the highlight or specular reflection of the image was removed by using highlight removal algorithm. LBP was used to extract the texture cues from the highlight removed image. Secondly, the texture of the original image was extracted. Lastly, by implementing the image distortions method previously introduced by Wen et al. (2015), the blurriness, chromatic moment and colour diversity features were utilized. The authors claimed that the proposed methods achieved the best performances in most intra-database and cross-database testing.

Fusion of multiple biometric traits has become another approach to protect face recognition systems against spoofing attacks. In 2008, Kollreider et al. proposed a combination of 3D properties and eye-blinking or mouth movements to combat three types of attacks: photograph; photograph wrapped over face with perforated eyes/mouth; and video display. The 3D spoofing countermeasure detected live faces based on nose peak compared to a photograph. This technique, however, can be challenged with perforated 3D face mask where both nose peak and eye-blinking exist. In another fusion technique, Tronci et al. (2011) claimed that both static and video analysis must be combined to give more information of the subjects for a more robust classification. Seven visual features were used under static analysis while the video analysis used two clues such as eye blinks and movements. Then, fusion was performed at score level to determine genuine faces and fake faces. This technique, however, suffers from the low number of eye blinks.

Yan et al. (2012) proposed fusing methods by combining three clues: (1) non-rigid motion analysis; (2) face-background consistency analysis; and (3) the effect of image banding analysis. Eye-blink is the non-rigid motion required in this study. The face-background consistency for the genuine face should be lower than the photo or video attack. The banding effect on each subject was determined by using Harr wavelet decomposition. Fake traits have higher median estimator values than the genuine faces. These analyses was carried out using INDIAP Print-Attack database and self-collected database. Finally, the results from these three analyses were fused to get the fusion results which achieved state-of-the-art results. A better study would examine the effect of head or lips movements on the non-rigid motion and face-background consistency analyses. Komulainen et al. (2013) highlighted the need to fuse the motion and micro-texture analysis under several types of scenic face attacks to improve spoofing countermeasure performance. Results of each individual countermeasure were fused at score level which show significantly improved fusion result. Unfortunately, the motion analysis was challenged by hand-shake photo attacks and thus caused confusion in the classification results.

From the discussion of the proposed fusion of multiple countermeasures above, it can be seen that the combination of multi-cues is a promising approach [Feng et al. (2016)]. Apart from that, previous studies based on single cue also showed best performances. Although it is hard to select one technique over the other, the main key to be considered is the structure of

the genuine face. Thus, the next section will discuss the physical structure of human skin and the optical properties resulting from the skin surface.

2.2 Human Skin

The results from previous studies in Section 2.1.3 reported on the discriminative differences of the reflections between real and fake faces. Each of the subjects had its own reflection property which could be manipulated in the ongoing face spoofing detection analysis. The understanding of human skin reflectance is vital so that it can be used as classification parameter in face spoofing detection. Physically, skin structure consists of three layers: the epidermis layer; the dermis layer; and the fat layer [Li et al. (2009, So-Ling and Ling (2001)]. The epidermis is the outermost layer of the skin. It contains particles called melanin which act as absorption and scattering agents. The quantity of melanin in the epidermis determines the skin colour of a human. For instance, fair skin colour has less amount of melanin compared to black skin colour [Zaidi (2016)]. The second layer is known as dermis which is a thick layer underneath the epidermis layer. The dermis contains haemoglobin which is carried by blood cells. The third layer is the deepest layer made of fat and connective tissue, known as subcutaneous tissue. Figure 2.1 illustrates the structure of the skin layers which was depicted by [Hoffman (2014)].

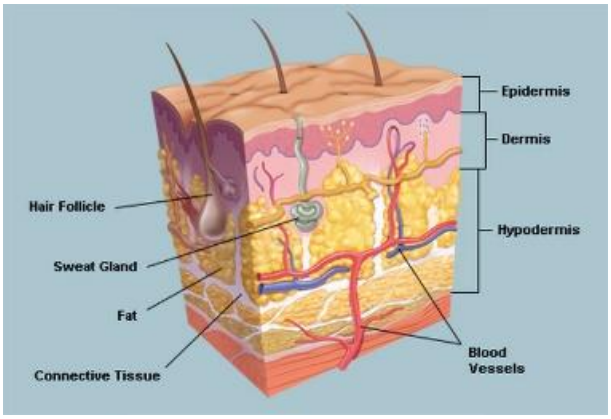

Figure 2.1: The structure of human skin. Source: Hoffman (2014)

Due to multilayers structures, skin consists of more than one reflection. Kollias (1996) indicated that the change in index of refraction, η as a factor to the multiple reflections of light from skin surface. For instance, the index of refraction for air and skin was 1 and 1.45, respectively. Therefore, when normal light beam strikes on skin surface, some of the incident light was reflected at the air-skin surface due to the differences in the index of refraction, η of each medium. Normal light wave vibrates in multi-directions from the light source. Because of the multi-directional vibrations, normal light wave is also known as unpolarised light.

The first reflection at the air-skin surface is called surface reflection. Approximately, the reflected beam is about 4-8% of the incident light while the remainder enters and traverses into the epidermis and dermis layers. The light is then absorbed and scattered by the epidermis and the dermis pigments before re-emerged through the skin surface into the air. This second reflection is known as subsurface or diffuse reflection. Figure 2.2 illustrates the interaction of normal light beam when it strikes on the skin surface. From the image in Figure 2.2, it can be seen that the particles such as melanin, collagen and haemoglobin in the epidermis and the dermis layers act as scattering and absorption agents on the light wave that penetrates through the layers.

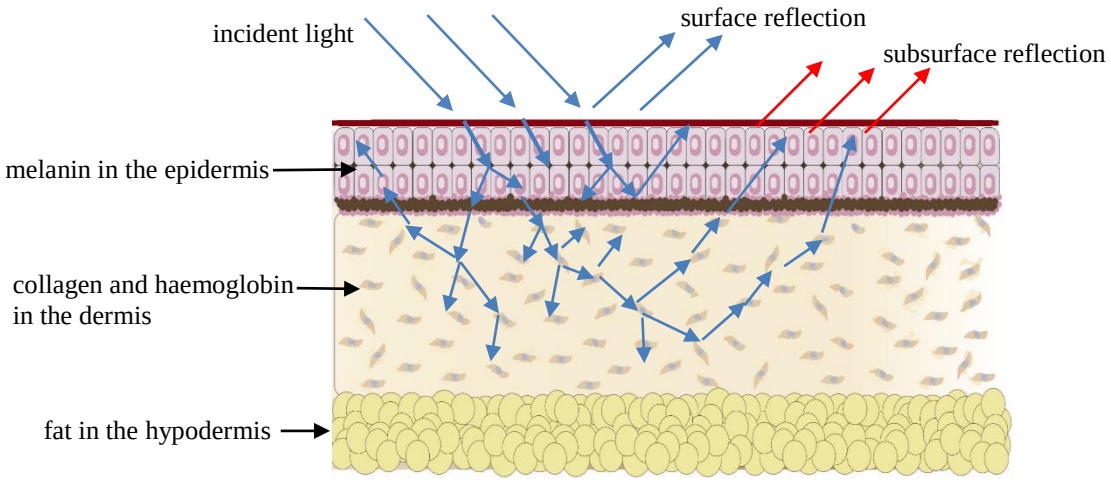

Figure 2.2: The interaction of light when hits the skin surface.
Source: Sullivan et al. (2013)

So far, this section focussed on the human skin structure and its multi-reflections properties when normal light wave strikes on the skin surface. As mentioned above, normal light wave vibrates in more than one direction towards a material surface. Despite normal light wave, the next section will discuss on light wave that vibrates only in single direction. This type of light wave is known as polarised light. In addition, the interaction of polarised light and skin surface will be described. Due to some advantages, polarised light have been used in studies for various purposes such as material classification and skin anatomy. These applications are discussed in detail in the next section.

2.3 Polarised Light

Light is made up of photons, which are packets of electromagnetic waves [Kollias (1996)]. Each photon is characterized by its frequency and wavelength. Originally, natural light wave received from the sun, fluorescent tubes, lamps and etc. vibrates in many directions [Sirohi (1993)]. The multi directional light wave is known as unpolarised light. Once the unpolarised light hits a surface, it is turned into polarised light: partially or completely polarised. Polarised light wave vibrates in only one direction depending on the angle of the incidence light and the surface material. For instance, according to Malus's Law, when a beam of white light hits a plate of glass at an angle, for example at an angle of incidence of 45^0, the reflected light beam polarized with a reflection angle is the same as the angle of incidence [Collett (2005)]. Figure 2.3 illustrates the interaction of natural light when it hits on a plate of glass at an incident angle θ_i and the light is reflected at reflection angle θ_r.

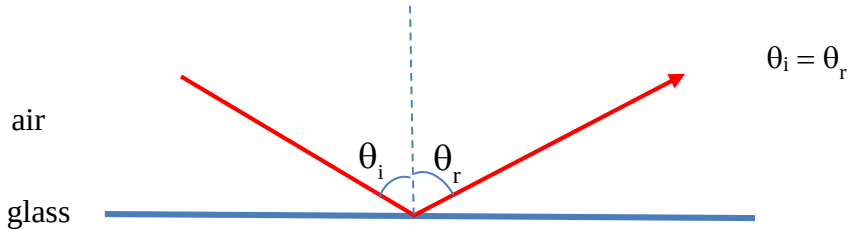

Figure 2.3: A light wave hits a glass surface at a Brewster's angle, θ_i

Polarisation is a process where unpolarised light turns to polarised light. Polarisation can be classified into two categories: (a) polarisation through natural process; and (b) polarisation by using additional device. Polarisation through natural process can be seen in daily physical processes such as refraction, reflection and scattering. The most common natural light polarisation is the sunlight reflection off the water surface. When sunlight falls on the ocean surface, it is reflected in all directions. The glitter of the reflection can only be seen when the position of the sun is above the horizon. At this small angle, the sun rays fall on the water surface and bounce off at the similar angle to reach the human eye [Ashish (2016)]. The ocean water glittering is one of the natural polarisation phenomenon.

Another method to obtain polarised light is by using an additional device such as a polariser. Polariser is an optical device that allows unpolarised electromagnetic wave to transfer through only in one direction to become polarised light [Polarizers (n.d.)]. A polariser can be physically found in different shapes: a polariser sheet, a glass polariser or liquid crystal polariser. The selection of polariser is dependent on the needs of a study. According to [Huard (1997)], the most common two polarisation states of light are linear polarisation and circular polarisation. Linear polarisation is defined as polarisation of an electromagnetic wave at a fixed point in a fixed direction, although varying in magnitude [Intelsat (2013)]. Circular polarisation consists of two perpendicular electromagnetic plane waves of equal amplitude and 90^0 differences in phase [Nave (2012)]. Figure 2.4 illustrates the states of polarisation when unpolarised light wave passes through two types of polarisers: linear and circular polarisers.

As depicted in Figure 2.4, polarised light vibrates in one direction after passing through a polariser. The direction of the polarised light is determined by the angle of the polariser. The polarised light wave will keep on vibrating until it lies on a plane of surface which is the plane that defines the interface between the two materials [Andrei (n.d.)]. Plane of incidence is the plane that contains the incident and reflected lights. There are two types of polarisations that vibrate towards a plane of interface which are the parallel and perpendicular polarisations as shown in Figure 2.5. As presented in Figure 2.5, the parallel polarisation is denoted as p-polarisation and it lies parallel to the plane of incidence, whereas the perpendicular is labelled as s-polarisation and it sticks up out of the plane of incidence.

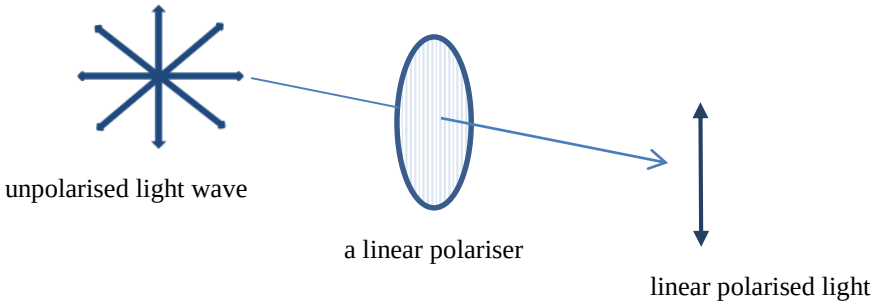

(a) Linear polarization

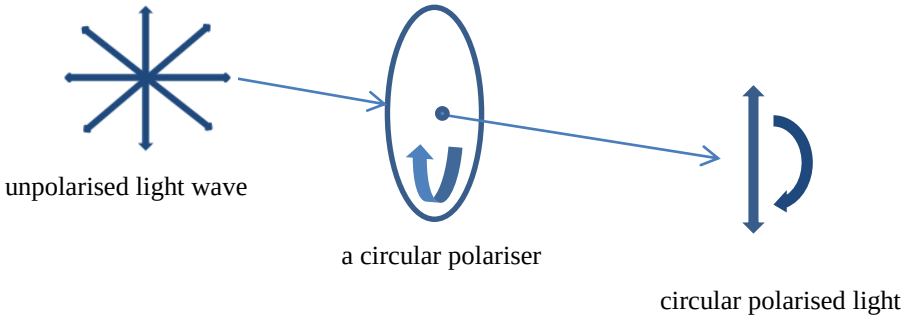

(b) Circular polarization

Figure 2.4: Two states of polarisation. (a) linear polarisation and (b) circular polarisation

Reflections from material surfaces that are not perfectly smooth are assumed to have details of the material [Wolff (1990)]. Most of the material surfaces consist of surface and diffuse reflections in which depends on the characteristics of the materials [Nayar et al. (n.d.)]. Materials with glossy appearance such as metals are more likely to have high specular reflection compared to matte surface, for example clay and paper. The differences in the reflection properties between the materials have been manipulated by researchers as one of the classification parameters. To measure the differences, polarized light is one of the most popular methods used.

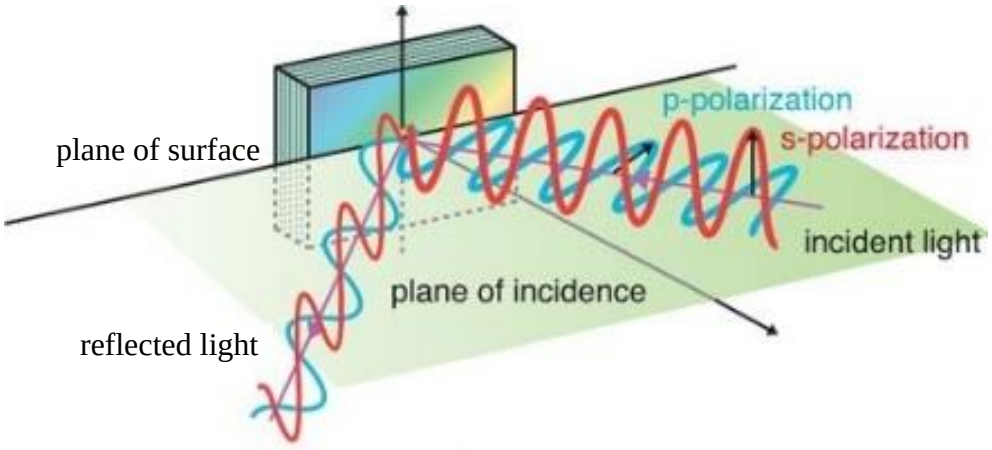

Figure 2.5: The interaction between polarised incident light and a material surface. Source: University of Delaware

2.3.1 Polarisation-based materials classification methods

Over the past two decades, polarised light has been used to classify materials. Wolff (1989) performed a similar series of experiments to show that reflection from object surfaces may be used to differentiate objects. The diffuse and specular reflection components can be separated by adjusting the parallel and perpendicular components of respective two dimensional plots of points. These plots of points form linear clusters which are used to determine the magnitude of the diffuse and specular component of reflection.

In 1990, Wolff introduced a polarisation-based method to discriminate between metal and dielectric surfaces based upon Fresnel reflectance theory. The ratio of the maximum to the minimum transmitted radiance with respect to the rotation of a polariser is used to calculate the Fresnel polarization, a value that differentiates the materials. However the main disadvantage of the proposed method is that it becomes inaccurate when the diffuse reflection component is higher than the specular reflection component. In a follow-up study, Wolff and Boult (1991) reported that the Fresnel polarisation reflectance model has been expressed in three terms of the parameters: I_{max}, I_{min} and the phase of the transmitted radiance. These can be used to obtain object features and enable the separation of diffuse and specular reflection components. Apart from that, the model can also be used to distinguish between material surfaces based on the relative electrical conductivity. Strong evidence of material surfaces classification based on the polarization method was found when the Fresnel reflectance model

shows a geometric reflectance model for light reflection and transmission. Then, Nayar et al. (1993) pointed out that the Fresnel ratio could not be constant and diffuse component may vary within the target region. They examined a method that combines both colour and polarisation, simultaneously, to separate the specular and diffuse components of reflection from images. The degree of polarisation of the images was measured for three colour bands: red, green and blue.

Later on, Hua and Wolff (1996) presented a polarisation phase-based method to differentiate between materials according to their intrinsic electrical conductivity. The phase shifted from an incident linear polarisation to an elliptically polarised state from conducting materials was measured to determine the material. For instance, a linear polarised incident light that reflected from a metal surface will change to elliptically polarised, but will remain as linear polarised light when reflected from a dielectric surface. The proposed method works quite well for metal identification under three conditions: indoor scene, outdoor scene and where there is significant diffuse reflection from dielectric surface in the same scene.

Since then, the popularity of the polarisation based techniques have been increasing particularly for the purpose of differentiating between materials. Sarkar et al. (2011) presented a real-time CMOS image sensor to differentiate between metal and dielectric surfaces. Various measurement metrics such as the Fresnel reflection coefficients and the degree of polarisation were shown to measure the variations of reflection. The measurement of the polarisation state of the reflected light served as an indicator for the type of material surface. The results showed that the degree of polarisation was higher for plastic than for aluminium. Moreover, Sarkar et al. (2011) also claimed that the polarisation of the reflected component varies with the conductivity of the metallic surface. A study by Mahendru and Sarkar (2012) examined the polarised reflection to classify among transparent and opaque objects. Different methodologies were presented such as Stokes degree of polarisation and polarisation Fresnel ratio. The degree of polarisation value for transparent object was quite higher as compared to opaque objects for most of incident angles. Based on the results it is easy to classify transparent object from opaque objects.

From the literature discussed above, the previous studies outlined that the polarisation imaging method has been able to classify materials into particular groups. For instance, classification between opaque and transparent objects and also classification between

conductor and insulator objects. However, to the best of the author's knowledge, previous studies on polarisation method to distinguish between human face and other materials have not yet been conducted.

2.3.2 Polarisation on human skin

The advantages of using polarised light photography on human skin as have been pointed out by Kollias (1996) will now be explained. Firstly, the surface and subsurface features of the skin can be selectively recorded. Secondly, polarised images yield more detail information of the skin features. For example, the surface features may be evaluated without the disruption by the subsurface features. The surface features can be eliminated by perpendicular polarisation therefore the characteristics of the subsurface become more prominent. Driven by these advantages, it will be necessary to discuss on the interaction of polarised light wave with human skin.

Interaction between unpolarised light wave and skin surface was explained in Section 2.2. The unpolarised light wave that vibrates in multi-directions, turns into polarised light wave, which vibrates in one direction through a process called polarisation. When polarised light wave hits skin surface, the interaction between polarised light and skin surface is similar as interaction of natural light on a plate of glass [Kollias (1996)]. As explained in Section 2.3, the reflection angle is the same as the incidence angle when light hits and reflected off a plate of glass. Thus, the angle of polarised incidence light on skin surface and polarised reflection light off the skin surface is also the same. Since polarised light vibrates in one direction, the direction is determined by the polarisation angle of a polariser in front of the unpolarised light source. To illuminate a plane of surface at maximum intensity of polarised light, angle of the polariser is adjusted to produce polarised light wave that is parallel to the plane of surface which is the skin surface. Figure 2.6 illustrates the interaction between parallel polarised light wave and the skin surface.

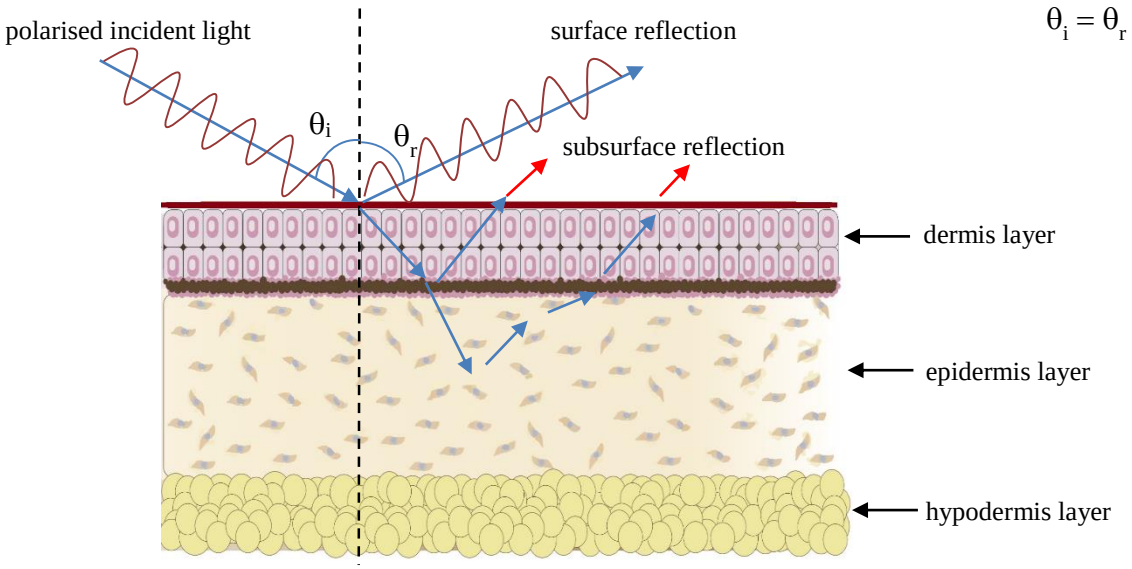

Figure 2.6: The interaction between polarised light and skin surface

From Figure 2.6, it can be seen that the angle of incidence, θ_i is equivalent with the angle of reflection, θ_r. Whereas the reflected light at θ_r is known as surface reflection, the remaining light component that is not reflected enters the skin through the epidermis and dermis layers. This is called subsurface reflection. As discussed in Section 2.3, there are two types of polarisations that vibrate toward a plane of interface, parallel and perpendicular polarisations. When parallel polarised light hits the skin surface, the surface reflection consists of both surface and subsurface properties. However, the surface reflection can be eliminated by using perpendicular polarised light source.

The emergence of optical polarisation imaging has aided researchers particularly in the field of biomedical to carry out more advanced studies on the structure of human skin. Jacques et al. performed similar series of experiments in the 2000s to show that polarised light could reveal the structure of multilayer surfaces such as skin. In 2000, Jacques et al. (2000) published a paper in which they showed the polarised image of chicken liver revealing the structure of a benign pigmented nevus. Two years later, Jacques et al. (2002) made a comparison between normal light images and polarised images of skin with various diseases. This comparative study found that polarisation images can visualize the disruption on skin surface such as skin

cancer. The specular reflection component from the skin surface was redirected at an oblique angle away from the camera by coupling the skin with a glass optical flat and a drop of water. The camera only captured light that had entered the skin and been backscattered towards the surface, which was known as diffuse reflection component.

In a follow-up study, Jacques and Ramella-Roman (2004) used Mueller matrix to describe how a tissue transforms a polarised incident light defined by Stokes vectors into an output collected light. Some of the elements of the Data Matrix were used to generate a new polarised image. Similar to their study in 2002, skin images were captured by placing a plate of glass with a drop of water to omit the surface glare. However, this method of combining Mueller matrix and Stokes vectors did not seems practical as the formula to generate the polarised image was similar to one of the Stokes vectors known as Q vector. In addition, the method introduced by Jacques (2002) was inconvenient for patients with burn or wounded skin characterisation.

Bin et al. (2007) demonstrated a polarisation imaging device that measured the Stokes components of the light transmitting through a specimen to distinguish between healthy breast tissue and breast tissue with cancer. Four intensity images were captured with different phase retardance of two types of illumination: unpolarised light and parallel polarised light. The Stokes vectors were then derived from the images. The texture of the images were individually analysed using an image analysis algorithm called Gray Level Co-occurrence Matrix (GLCM). The results suggested that multi-polarisation Stokes images showed better classifications performances compared to a conventional intensity image.

Hanrahan and Krueger (1993) conducted a study on the reflection from layered surfaces due to subsurface scattering. The results showed that skin surface reflection was affected by subsurface reflection in layered surfaces. A reflectance model was presented which incorporated directional scattering within the layer. The model showed that the concentration of blood and melanin in the dermis layer and epidermis skin layer gave different skin surface reflections. Bae et al. (2010) found that values from the images obtained using parallel polarized light were related and affected by human skin surface characteristics. This method was used to evaluate dermatologic diseases, especially in relation to skin multi-layers structure.

Ghassemi and Miranbaygi (2009) investigated the changes of polarisation state of light scattered from skin surface. A skin-like phantom made of epoxy resin with titanium dioxide (TiO_2) which is similar to a sample model of scattering skin was used. The state of polarisation was assessed with a combination of Stokes parameters and Mueller matrix. Stokes parameters were applied to measure the polarised light and Mueller matrix was applied to the skin. The results showed that some elements of the matrix were sensitive to the size and shape of the scatterers and properties of the skin. Thus, the results suggested that different materials provide different polarised reflectance values. In another study, Matsubara (2012) manipulated the advantages of using polarised light to classify skin into several age groups. The parallel and the perpendicular polarisations were used to capture the surface and the subsurface reflection components, respectively. The reflection characteristics varies accordingly to the age groups, for instance younger skin gives higher surface reflectance compared with older skin. The results from this study showed the multi-reflections of human skin which could be separated with ease through polarisation method.

Rudd et al. (2016) presented polarisation imaging technique to distinguish between genuine face, LCD screen displayed face and paper face mask. Polarised light was used to capture images of the subjects at parallel and perpendicular polarisation angles. Each image was visually compared in which promising differences were spotted between the real and fake faces. However, there was no measurement parameter applied to significantly classify the subjects.

2.3.3 Near infrared polarisation

Besides the visible light polarization imaging, there is a number of studies that reported on human skin analyses by using near infrared (NIR) light on the polarization imaging system. Visible light is defined as the wavelengths that are visible to human eyes [Lucas (2015)]. The wavelength range of visible light are from 400 to 700 nanometres (nm) and a colour range of violet through red [Madigan (2017)]. Whereas the infrared (IR) light corresponds to the wavelength range of 750 to 2,500 nm [Pasquini (2003)], near infrared (NIR) light is within the region between 750 to 1400 nm [Liew (n.d.)]. NIR is invisible to human eye [Dryden (2014)] and the NIR radiation penetrates deeper into human body compared to visible light [Jaminet

(2015)]. In addition, water molecules in human skin will absorb the NIR radiation [Davies (n.d.)].

Thus, several studies have revealed that NIR spectrometry penetrates deeper into human skin to reach deeper tissues. One study by Ali et al. (2004) examined the content of water in cancerous and normal human prostate tissues under NIR spectrometry. The results showed that the water content in normal tissues were more than in cancerous tissues. Zhang et al. (2013) combined visible and NIR spectrometry to differentiate tumor tissues from normal breast tissues. The results showed the effectiveness of the combined spectral analysis compared with the individual spectral analysis. In the same vein, Chen et al. (2015) proposed a method to distinguish between normal and malignant colorectal tissues by combining NIR spectrometry with chemometrics. Lee et al. (2006) used similar method to discriminate between cancer and normal tissues. Collectively, these studies highlighted the effectiveness of using the NIR spectrometry to distinguish between normal and abnormal tissues in human body.

A number of studies have attempted to apply the NIR polarized light for further analyses involving human internal tissues. One study by Demos et al. (1997) applied polarization filter to discriminate between normal and cancerous part of human breast tissue. Laser light with 1064 nm wavelength was used as the light source. Images of parallel and perpendicular polarization were obtained in which the experiment results showed that different types of tissue depolarize light to different degrees of polarization (DOP). Wang et al. (2003) implemented NIR spectral polarization imaging technique to detect prostate cancers through rectum-membrane-prostate tissues. The technique was able to detect small objects and structural changes in the cancerous tissues. In another study, Shao et al. (2010) utilised the polarized NIR autofluorescence (AF) imaging which was integrated with the diffuse reflectance technique for improving colonic cancer detection. This study used colonic tissue specimens that was paired with saline solution. The results show that the intensity of the NIR AF images with cancer tissues was lower than the normal tissues. From the three studies, NIR polarization imaging technique showed significant differences between normal and abnormal human tissues.

2.4 Evaluation on Depth Sensors

Depth sensor is a low-cost technology and an alternative equipment to replace expensive 3D scanner. First version of a depth sensor which is known as Kinect for Xbox 360 was introduced in 2010 by Microsoft mainly for computer games. Then, Asus launched its very own depth sensor in 2011, called as Xtion Pro Live. One year later, Microsoft launched the second generation of Kinect sensor known as Kinect for Windows. In 2014, once again Microsoft introduced the latest version of the Kinect depth sensor which has been named as the Kinect for Windows v2. These depth sensors are inexpensive and can be easily purchased by consumers via online shopping. Apart from being used in computer games, depth sensors have also been used to capture depth images for various purposes. For instance, depth images are used for 3D objects reconstruction. Apart from that, the depth images can also be used in face anti-spoofing studies. As discussed in Section 2.1.2 and Section 2.1.3, there are several face spoofing countermeasures carried out by analysing colour and depth images in a publicly available 3DMAD database. Since the 3DMAD database was developed by recording the images using depth sensor known as Microsoft Kinect for Xbox 360, the characteristics of the depth pixels have become an issue.

Thus, in 2011, Khoshelham (2011) investigated the geometric quality of depth data obtained by the Kinect sensor. From the experiments, the random error of depth measurements increases with the increasing distance between the sensor and the object. In addition, the depth resolution becomes very low at large sensor-object distance. Moreover, Macknojia et al. (2012) presented an analysis to find out the main characteristics of the operating conditions of two depth sensors: Microsoft Kinect Xbox 360 and Microsoft Kinect for Windows. Both sensors were placed on a flat surface and aligned parallel to objects at different distances between 0.4 and 5 meters. The experiments were carried out over two types of scenes: (1) a white wall, a black door and various object with different shapes and colours; and (2) a car in an underground garage. The findings from the investigations suggested that both depth sensors perform fairly well at working distances up to 2m. The performance degraded with the increase in the distance from the object. In addition, non-transparent but shiny object with highly curved shapes were acquired for relatively accurate performances.

From the results of both studies by Macknojia et al. (2012) and Khoshelham (2011), the depth pixels performances obtained from the Kinect for Xbox 360 sensor decreased with

the increase of the object-sensor distances. Since the 3DMAD database was recorded by using the similar depth sensor, the results from the spoofing analysis that have been carried out using images from 3DMAD database could be questioned.

2.5 Conclusion

As reviewed in this chapter, a great amount of research has been carried out to protect the vulnerabilities of face biometric systems from spoofing attacks. It is hard to select one technique over the other as spoof countermeasure on face recognition systems. Face recognition systems have been broadly classified into two groups: 2D and 3D systems. Conventionally, 2D face recognition systems can be spoofed by presenting photo paper or playing a video in front of the sensor. 3D face models or face masks made of various materials such as silicone gel or rubber could be used to attack both 2D and 3D face recognition systems [Zhang et al. (2011)]. In principle, the 2D face recognition systems are more often attacked by impostors [Chakka et al. (2011)]. On the other hand, 3D spoofing requires the creation of 3D masks that mimic the real users' face. The difficulty to get 3D face masks due to high costs have led to a lack of publicly available 3D face spoofing databases. This in turn has caused fewer studies in 3D face spoofing countermeasures.

In view of the literatures that has been mentioned so far, the possibility in using polarization technique as one of the anti-spoofing techniques in face recognition systems is undeniable. Since the human skin consists of multiple layers which produce more than one reflection, each reflection might provide unique values that could be used as a mark between genuine and fake faces. Other than that, due to the ability of polarization technique in object classification, similar procedure could be implemented to discover the polarization properties of human skin compared to other materials. To analyse the differences, the degree of polarization and the Stokes parameters are two main parameters to be implemented throughout this study.

Chapter 3: Methodology

3.1 Overview of Polarisation Imaging System

3.1.1 Introduction

This section introduces the polarisation imaging system used in the investigations throughout this thesis. Basically, polarised light is required in a polarisation imaging system. As explained in Section 2.3, polarised light is light wave that vibrates in one direction through a process known as polarisation. Naturally, lights from sources such as the sun, fluorescent tubes and lamps are unpolarised. These types of lights are also known as visible lights which visible to human eye [Lucas (2015)]. Light is measured by its frequency (in Hertz) or wavelength (in nanometres). The wavelengths of visible light are in between 400 to 700 nanometres (nm). Wavelength is the measure of distance between two successive wave crests or troughs. Frequency is the number of waves that passes a given point at every second. Figure 3.1 illustrates the crests and troughs of light waves in which the distance between the two crests or troughs is called wavelength.

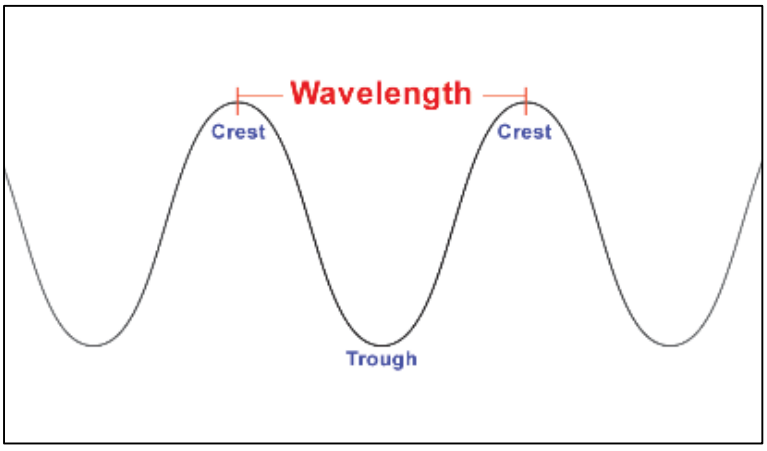

Figure 3.1: The wavelength of light wave

Normal visible light wave which is also defined as unpolarised light, vibrates in multi directions until it lies on a surface [Sirohi (1993)]. Naturally, when unpolarised light interacts with another medium, the unpolarised light wave is turned into two types of polarised lights: partially or completely polarised light. Two properties of light wave occur when the beam of light interacts with a medium [Vandergriff (2008)]. Firstly, the light wave is reflected off the surface. Secondly, the light wave is refracted through one medium to another. In this study, light reflections off skin surface was investigated to be compared with reflections from surfaces of other materials. As has been discussed in Section 2.2, skin produces two types of reflections known as surface and subsurface reflections. These multi-reflections criteria could be one of the discriminative factors between genuine faces and fake faces used in this study. Polarised images are one of the methods that could be used to differentiate between the two reflections. Polarised images are a number of images captured under different polariser angles in a polarisation imaging system. Detailed explanation on polarised images, polarisation angles and polarisation imaging system are discussed in the next sections.

Material classification has been studied by many researchers using polarisation method. The state of polarisation of each material, for instance aluminium and glass, have been analysed for classification. Previous studies have reported that polarization method could be used to differentiate between metal and non-metal objects [Sarkar et al. (2011); Hua and Wolff (1996)], but to date none has been applied to distinguish between human skin and other materials. However, a number of studies have found that polarized reflection can discriminate between normal and abnormal skin tissues [Demos et al. (1997); Bae et al. (2010); Jacques et al. (2002)]. In addition, numerous studies have emerged on skin multilayer reflections which attempted to separate these reflections by using polarization method [Hanrahan and Krueger (1993); Ghassemi and Miranbaygi (2009); Matsubara (2012)].

Along with the growth of studies in using polarised light source questions have been raised about the significance in using polarised light source compared to unpolarised light. Therefore, unpolarised visible light source is initially used in a polarisation imaging system, which will be introduced in the next section, to investigate the consequences on real and fake faces reflectance based on two parameters: (1) the degree of polarisation; and (2) the Stokes parameters. Similarly, a study by Mahendru and Sarkar (2012) adopted unpolarised light source to examine the degree of polarization (DOP), the polarization Fresnel ratio and the Stokes degree of polarization between transparent and opaque objects. The DOP value of the

transparent object was found higher than the opaque object and the differences used to distinguish among the two objects.

3.1.2 Polarisation imaging system

The principle of a polarisation imaging system usually adopts the following modules: (1) incident light gets through a polariser; (2) polarisation angles; and (3) a group of intensity value of output light [Zhao et al. (2016)]. Driven by several linear polarisation imaging systems proposed by previous studies [Sarkar et al. (2011); Ghassemi and Miranbaygi (2009); Bin et al. (2007)], the principle of the polarisation imaging technique proposed in this study is relatively similar to the previous studies. The proposed linear polarisation imaging system consisted of a camera, light source, two sheets of linear polariser (P_2 and P_3) and one glass linear polariser (P_1) coupled with an angle rotator. Basically, a polariser was placed in front of normal light source to produce polarised light. Another polariser coupled with an angle rotator was mounted in front of the camera lens to adjust the polarisation angles. Figure 3.2 illustrates the principle of polarisation imaging system proposed to be used throughout the analysis in this thesis. As presented in Figure 3.2, P_1 is a polariser in front of the camera lens. P_2 and P_3 are polarisers mounted in front of each light source.

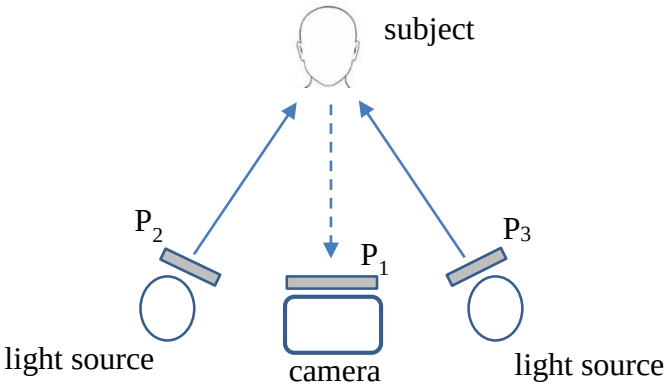

Figure 3.2: The polarisation imaging system

3.1.3 Polarisation axis

Polarisation axis is the relationship between the vibration of electromagnetic wave from the light source and the axis of the polariser in front of the camera lens, P_1. When the vibration of polarised light source is perpendicular to the axis of P1, the light wave is blocked from passing through P_1. This is known as perpendicular polarisation axis. Meanwhile, any vibrations from the light source that are parallel to the P_1's axis are allowed to pass through. At this point, the polarisation is called parallel polarisation. There are several steps to determine the polarisation axis between P_1, P_2 and P_3 polarisers.

Firstly, polarisers P_1 and P_2 were placed next to each other as illustrated in Figure 3.3(a). For clearer vision, an object such as a pen was placed at the back of the two polarisers. Then, P_2 was slowly rotated on top of P_1 until all light was blocked and the pen could no longer be seen through the two overlapping polarisers. At this position, the polarisation angle between P_1 and P_2 is called perpendicular polarisation as can be seen in Figure 3.3(b). Images capture under perpendicular polarisation consist minimum light intensity. Next, P_2 was rotated once again until the pen was clearly visible. At this orientation as shown in Figure 3.3(c), the P_1 and P_2 axes were parallel to each other where maximum light intensity was transmitted through the polarisers. Since the polarisation imaging system shown in Figure 3.2 consists of two lights source, the position of P_3 was set in the same direction as the position of P_2.

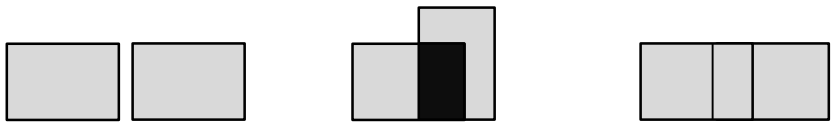

(a) P_1 and P_2 (b) perpendicular (c) parallel

Figure 3.3: The determination of the P_1, P_2 and P_3 polarisation axes

3.1.4 Polarisation angle

Polarisation angle refers to the angle of polariser that is mounted in front of the camera lens, P_1. From the previous studies on materials classification using polarisation imaging

technique [Mahendru and Sarkar (2012); Sarkar et al. (2011); Hua and Wolff (1996)], four polarisation angles: 0^0, 45^0, 90^0 and 135^0 were used to capture images of the research subjects. These angles were selected based on the requirements of the parameters used to measure the polarised images: (1) the degree of polarisation; and (2) the Stokes parameters. As explained in Section 3.1.2, P_1 is a glass polariser which was coupled with an angle rotator. The angle of P_1 was adjusted by using the angle rotator. Figure 3.4 shows the label of the angle rotator of the glass polariser, P_1.

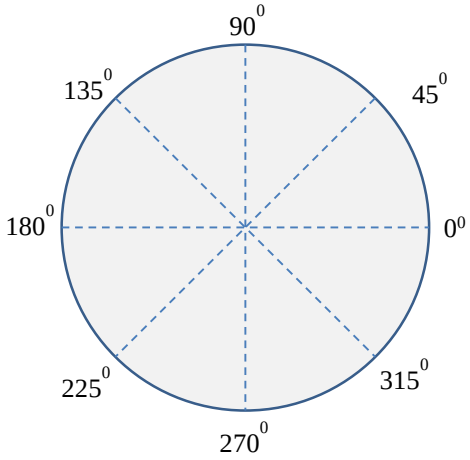

Figure 3.4: The polarisation angles

3.1.5 Polarised image

In this study, polarised images are defined as images of genuine faces, printed photo papers and iPad displayed faces, captured under polarised light at four different polarisation angles: 0^0, 45^0, 90^0 and 135^0, by manually rotating P_1. At each polarisation angle, three frames of images were captured for each subject. Then, these three images were aligned and processed using image registration algorithm based on Speeded_Up Robust Features (SURF) descriptor. After registration process, the three images were averaged to get one final polarised image for each subject at all polarisation angles. Finally, the Stokes parameters and the degree of polarisation (DOP) were applied to generate the SDOLP image, I_{SDOLP} and the polarisation image, I_{DOP} for further investigations. The SURF descriptor, the Stokes parameters and the DOP are explained in detail in the next sections.

3.2 Overview of parameters

To further analyse the polarised images of genuine and fake faces captured in each experiment, two parameters are applied: the Stokes parameters and the degree of polarisation. Detail explanation on each parameter is explained in the next sections.

3.2.1 The Stokes parameters

The state of polarisation of reflected light wave can be described by the Stokes parameters. These parameters were introduced by Sir G. C. Stokes in 1852. The parameters consist of four components: S_0, S_1, S_2 and S_3. The value of each component is calculate for every pixels of an image. These components are presented in a 4x1 column matrix known as the Stokes vector, as shown:

$$Stokes = \begin{bmatrix} S_0 \\ S_1 \\ S_2 \\ S_3 \end{bmatrix} \tag{3.1}$$

The Stokes parameters presented in equation (3.1) can be described as intensity (S_0), degree of polarisation (S_1), plane of polarisation (S_2), and ellipticity (S_3). Since only linear polarisation was used in this study, circular and elliptical polarisation did not occur. Therefore, the S_3 component that relates to the circular polarisation was omitted. The components S_0, S_1 and S_2 were obtained using images captured at four polarisation angles: 0^0, 45^0, 90^0 and 135^0; these image components were created as:

$$\begin{aligned} S_0 &= Img_0 + Img_{90} \\ S_1 &= Img_0 - Img_{90} \\ S_2 &= Img_{135} - Img_{45} \end{aligned} \tag{3.2}$$

where Img_0, Img_{45}, Img_{90} and Img_{135} are the polarised images captured at polarisation angles of 0^0, 45^0, 90^0 and 135^0, respectively. Once the Stokes components were derived in term of

images, the components were then used to generate the final image known as the Stokes degree of linear polarisation image (I_{SDOLP}) as:

$$I_{SDOLP} = \frac{\sqrt{S_1^2 + S_2^2}}{S_0} \tag{3.3}$$

As explained in Section 3.1.3, parallel and perpendicular polarisations are obtained by adjusting the angle of polariser, P_1 to 0^0 and 90^0, respectively. Polarised images captured under each polarisation angle have been denoted as Img_0 and Img_{90}. Img_0 consists of both surface and subsurface (diffuse) reflections; Img_{90} consists only the subsurface reflection [Matsubara et al. (2012)]. According to Jacques et al. (2002), an image that consists of only surface reflectance can be obtained by subtracting Img_{90} from Img_0.

3.2.2 The Degree of Polarisation (DOP)

An incident light that interacts with surface will be reflected and the reflected light is partially polarized [Sarkar et al. (2011)]. The degree of polarization (DOP) is one of the parameters used to measure the portion of reflected light that is polarised compared to the total amount of the reflected light. The scalar value of the DOP is between 0 and 1. The DOP can also be expressed in terms of maximum and minimum light intensities of every pixels of an image, transmitted through linear polariser as:

$$DOP = \frac{I_{max} - I_{min}}{I_{max} + I_{min}} \tag{3.4}$$

where I_{max} is the maximum light intensity while I_{min} is the minimum light intensity transmitted through polariser in front of the camera lens, P_1. As explained in Section 3.1.3, images captured under 0^0 polarisation angle consist of maximum light intensity. Thus, an image taken under 0^0 polarisation angle is labelled I_{max} whereas I_{min} is an image captured under 90^0 polarisation angle. The two images are denoted as Img_0 and Img_{90}, respectively, which are then used to

generate the third image known as polarisation image, I_{pol}. Hence, equation (3.4) can be rewritten as:

$$I_{pol} = \frac{Img_0 - Img_{90}}{Img_0 + Img_{90}} \tag{3.5}$$

The polarisation image, I_{pol} is based on the ratio of a numerator that represent surface reflectance and a denominator that represent the total reflectance. From equation (3.5), it can be seen that the $Img_0 - Img_{90}$ and the $Img_0 + Img_{90}$ are equivalent to S_1 and S_0 in equation (3.2), respectively. Therefore, equation (3.5) can also be written as:

$$I_{pol} = \frac{Img_0 - Img_{90}}{Img_0 + Img_{90}} = \frac{S_1}{S_0} \tag{3.6}$$

3.3 Preliminary experiments

The proposed polarisation imaging system as proposed in Section 3.1.2 requires a linear polariser to be installed in front of each light source. The reason for this is to transfer the unpolarised light source to polarised light wave. Similar polarised imaging system has been adopted in a number of studies such as for object detection applications. Along with the growth of studies in using polarised light source, questions have been raised about the significance in using polarised light source compared to unpolarised light. In this chapter, unpolarised visible light source was initially used in the following experiments to investigate the consequences on the results for the Stokes parameters and the degree of polarisation. The first experiment was carried out by using fluorescent ceiling light and the second experiment was done by using table light. The reasons for choosing the two types of lights are due to the low cost and the lights are easily obtained from local shops. In both experiments, no polariser was installed in front of the lights. Only one polariser, P_1 was mounted in front of the camera lens.

Prior to commencing the study, ethical clearance was sought from the Department of Computer Science, University of Reading. All subjects were firstly required to read the

information sheet to understand the experiment procedures. They were then asked to sign the ethical form before proceeding with the recording processes.

3.3.1 Unpolarised fluorescent ceiling light

The first experiment was conducted by using ceiling fluorescents bulbs as the light source that was already available in the room. The fluorescent bulbs colour temperature is 3500k. To control natural illumination from affecting the experiment result, the recording process was conducted in a dark room. As a start, to see if various surface materials gave different reflectance measurements, one genuine human face and three fake faces made of paper, plastic and rubber were used as the experiment subjects. Figure 3.5 illustrates the experiment setup. As shown in Figure 3.5, the distance between the subject and the camera is 1.5 meters, approximately. The distance was chosen to imply the actual situation at a building access control. A Samsung Full HD camera was used for the recording processes in which a linear polariser, P_1 coupled with an angle rotator was mounted in front of the camera lens. Aperture setting for the camera was f/1.4. Images of each subject were recorded at four polarization angles: 0^0, 45^0,90^0 and 135^0, by manually rotating P_1. The recorded images were then labelled accordingly to the polarization angles as Img_0, Img_{45}, Img_{90} and Img_{135}. The following processes were based on the proposed anti-spoofing face detection framework in Figure 1.2.

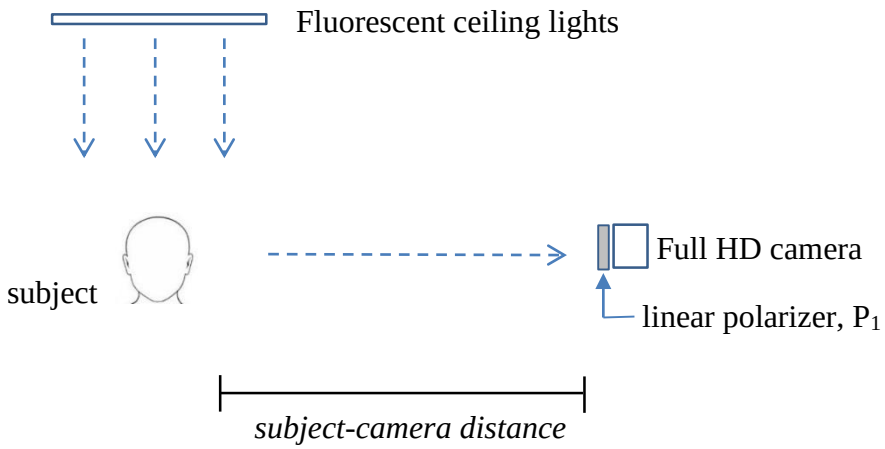

Figure 3.5: Experiment setup for the unpolarised fluorescent ceiling light source

At each polarisation angle, three frames of images were captured for each subject. The images were then cropped at the face region. Since three frames were recorded within a period of time, the three images needed to be aligned. Image registration is the process of overlaying two or more images taken at the same scene within a period of time [Zitova and Flusser (2003)]. In addition, the image registration applications can be divided into four groups: (1) different viewpoints; (2) different times; (3) different sensors; and (4) scene to model registration. The image registration process geometrically aligned two images: a referenced image and sensed image. In this study, at least three frames of images were taken at each polarisation angle for each subject. Thus, image registration process was required to align the three polarised images. To do this, an image registration algorithm based on SURF (Speeded Up Robust Features) descriptor as proposed by Bay et al. (2008) was used in the image alignment process throughout this thesis. In SURF, Hessian-matrix approximation which lends on an integral image was used for the interest point detection. The integral image, $I_{\sum}(x)$ at a location $x = (x,y)^T$ represents the sum of all pixels in the input image I within a rectangular region formed by the origin and *x*:

$$I_{\sum}(x) = \sum_{i=0}^{i \le x} \sum_{j=0}^{j \le y} I(i,j) \tag{3.7}$$

The Hessian matrix in *x* at scale σ is defined as follows:

$$H\,(x,\sigma) = \begin{bmatrix} L_{xx}(x,\sigma) & L_{xy}(x,\sigma) \\ L_{xy}(x,\sigma) & L_{yy}(x,\sigma) \end{bmatrix} \tag{3.8}$$

where $L_{xx}(x,\sigma)$ is the convolution of the Gaussian second order derivative $\frac{a^2}{ax^2} g(\sigma)$ with the image I in point x, and similarly for $L_{xy}(x,\sigma)$ and $L_{yy}(x,\sigma)$. After image registration, the three images were averaged to get one final image representing each polarisation angle. There are several advantages of using image averaging technique to reduce image noise [McHugh (2005)]: (1) image averaging reduces noise by increasing the signal to noise ratio (SNR) of an image; (2) increases the bit depth of the image; and (3) remove noise without softening the image. The final processed images of each subject are presented in Figure 3.6.

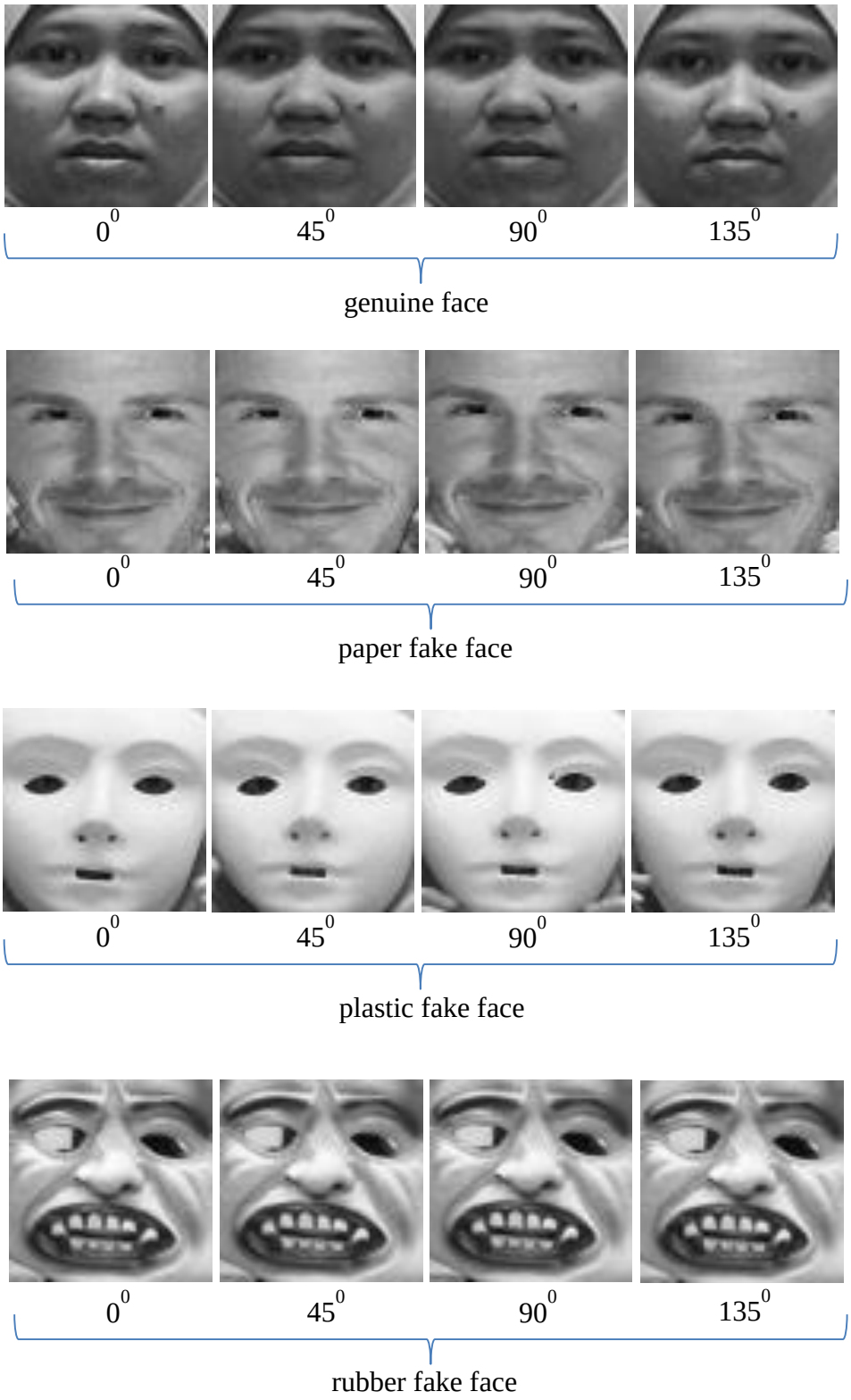

Figure 3.6: The polarised images of the real face and three fake faces: paper, plastic and rubber; captured at four polarisation angles

As coarse comparison, it is apparent that there is no significant difference between the images of the real and fake faces in Figure 3.6 at each polarisation angle. To further analyse the images, two parameters were applied which are the Stokes parameters and the degree of polarisation.

a) The Stokes parameters

By using equation (3.2), three of the Stokes components were generated in the form of images as presented in Figure 3.7. Apparently, no significant difference can be seen on the S_0, S_1 and S_2 components between real and fake faces. For further comparison, histograms are plotted as graphical representation of each images. The histograms of the S_1 and S_2 clearly show the similarity of the pixels intensity distributions between the four subjects. In contrast, S_0 histogram of the real face is significantly different than the other subjects. Although the real and fake faces have S_0 contrastive histograms shapes, the comparison is not practical since the number of subject is very small.

The next investigation is to find any differences in the states of polarisation of reflected light wave between the subjects. By using the Stokes components in Figure 3.7, the final image known as the Stokes degree of linear polarisation image, I_{SDOLP} was produced for each subject based on equation (3.3). Figure 3.8 shows the I_{SDOLP} for the real face and the three fake faces. As can be seen, the I_{SDOLP} shown in Figure 3.8 are quite similar to each other in term of intensity. Histograms of each I_{SDOLP} is also plotted to graphically represent the intensity distributions. From the histograms, the data distribution among the subjects are close to each other. For instance, all of the four histograms are right skewed with unimodal data distributions. For further analysis, the I_{SDOLP} are statistically analysed to justify the initial assumption of the data distributions between the real and fake faces. In statistics, there are four moments that can be used to quantitatively measure a set of data. The four moments are the mean, the standard deviation, the skewness and the kurtosis.

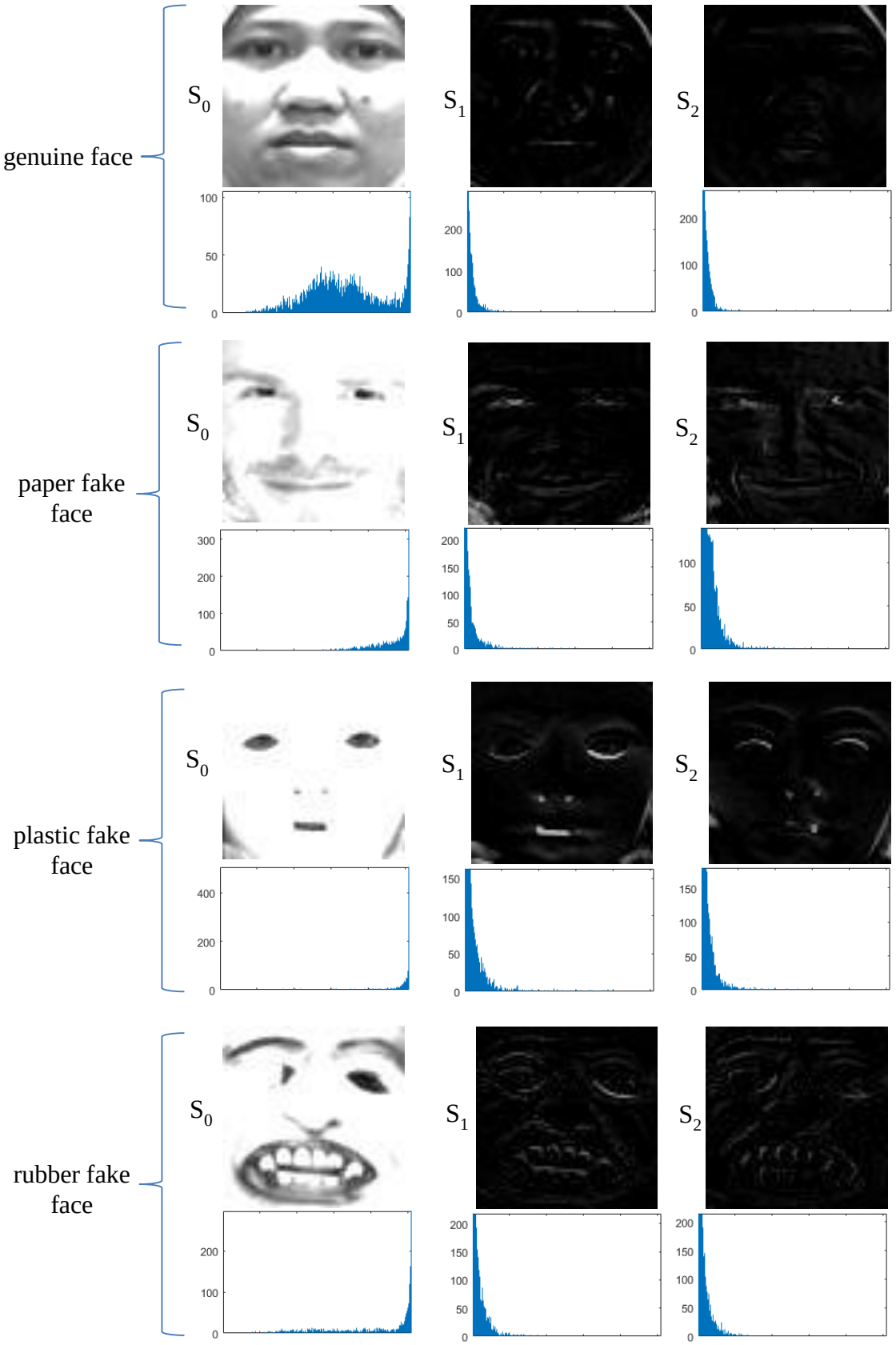

Figure 3.7: The Stokes components under unpolarised fluorescent ceiling light source

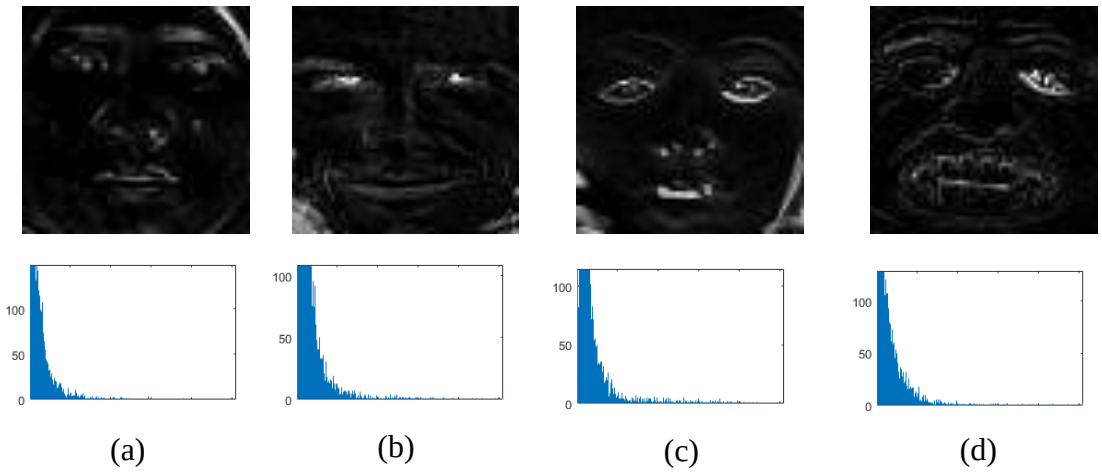

Figure 3.8: The I_{SDOLP} under unpolarised fluorescent ceiling light source for: (a) real face; (b) paper fake face; (c) plastic fake face; and (d) rubber fake face

The mean is the first moment in data distribution. In this study, the mean value is measured on a per-pixel basis. To calculate the mean, the observed values were added up then divided by the quantity of values available. The mean can be conveniently expressed by:

$$Mean, \bar{x} = \frac{1}{N}\sum_{j=1}^{N} x_j \tag{3.9}$$

where x is each of the value of a distribution and N is the sample size. The second moment in a data distribution is known as standard deviation which is a per-pixel basis measurement. Standard deviation is a square root of variance defined as:

$$Standard\ deviation, \sigma = \sqrt{\frac{1}{N-1}\sum_{j=1}^{N}(x - \bar{x})^2} \tag{3.10}$$

The skewness or the third moment is a measure of symmetry of a distribution around its mean. The skewness is a pure number that characterizes the shape of distribution. The skewness is defined as:

$$Skew(x_1 \dots x_N) = \frac{1}{N}\sum_{j=1}^{N}\left[\frac{x_j - \bar{x}}{\sigma}\right]^3 \tag{3.11}$$

where σ = σ (x_1 ... x_N) is the standard deviation of a distribution. Positive value of skewness signify a distribution that is skewed right; negative value indicate data that are skewed to the left. Data that are skewed to the right have a long tail that extends to the right while data that are left skewed have a long tail that extend to the left [Taylor (2017)].

The other common measure of shape is called kurtosis. Kurtosis is the fourth moment which represents the sharpness of the peak of a distribution curve. Kurtosis is similar to skewness in which no unit represents the value of both skewness and kurtosis. A pure number characterizes kurtosis [Brown (2016)].

$$Kurt\ (x_1 \dots x_N) = \left\{\frac{1}{N}\sum_{j=1}^{N}\left[\frac{x_j - \bar{x}}{\sigma}\right]^4\right\} - 3 \tag{3.12}$$

where the -3 term makes the value zero for a normal distribution. The skewness and kurtosis measures are done on a per-image basis.

The value of the mean, the standard deviation, the skewness and the kurtosis of the real and fake faces are presented in Table 3.1. The results from Table 3.1 indicate that there are little differences of the mean, the standard deviation and the skewness between the materials. Meanwhile, the kurtosis of the real faces has higher value in comparison to the fake faces. Despite the difference in kurtosis value between the real and fake faces, there are no significant differences as the histograms' shape are more or less similar between the materials

Table 3.1: The statistical results for the I_{SDOLP}

	Real face	Paper fake face	Plastic fake face	Rubber fake face
Mean	13.58	18.93	20.08	16.05
Standard Deviation	21.78	24.65	29.16	22.94
Skewness	7.11	3.11	3.56	5.84
Kurtosis	70.20	12.32	15.66	49.85

b) The degree of polarisation

As was explained in Section 3.2.2, DOP is the ratio of reflected light that is polarised compared to the total amount of the reflected light. In this study, the DOP value is analysed in terms of image intensity. Thus, by using equation (3.6), the polarisation image of the real and fake faces is created based on the images components in Figure 3.7. The polarisation image, I_{pol} of each material is presented in Figure 3.9. It can be seen from the I_{pol} images in Figure 3.9 that the images are dark in which no image is formed. The Ipol images were then statistically analysed and the results are set out in Table 3.2.

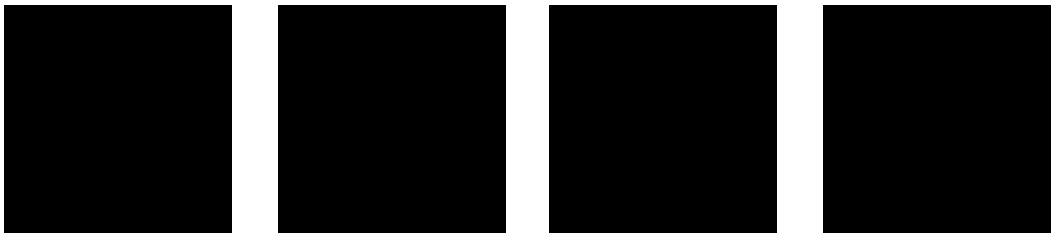

(a) (b) (c) (d)

Figure 3.9: The I_{pol} images under unpolarised fluorescent light for: (a) real face; (b) paper fake face; (c) plastic fake face; and (d) rubber fake face

From the data in Table 3.2, the mean value of the intensity and the standard deviation between the subjects are very small. The results suggest that the amount of polarised reflected light from each subject is very small thus considered as no polarised reflected light exists. Furthermore, the skewness and kurtosis are not available due to the very dark intensity of the

images which indicate no distribution produced. Overall, the I_{pol} images captured using the unpolarised fluorescent ceiling light could not be used to differentiate between the real and the fake faces.

Table 3.2: The statistical results for the I_{pol} images

	Real face	Paper fake face	Plastic fake face	Rubber fake face
Mean	0.0039	0.0093	0.0132	0.0063
Standard Deviation	0.0624	0.0959	0.1141	0.0854

3.3.2 Unpolarised table light

In Section 3.3.1, it is proven that the I_{SDOLP} between the real and fake faces captured under unpolarised fluorescent ceiling light do not provide significant statistical difference. In addition, no polarisation image was created as the image turned dark. In this section, the experimental setup was copied from the investigation carried out by Mahendru and Sarkar (2012). However, several settings were modified to suit the needs of this study. Firstly, different light source was used in this study, which was a table light with a 25W bulb. The lights temperature was 2700k which is an extra warm white light. Secondly, the subject-camera distance was increased to 80cm instead of 25 cm. The original distance was too close to human and may disrupt the vision of the real subject. Figure 3.10 illustrates the experiment setup for the unpolarised table light source. A table light was placed on the left side of the camera at an angle of 45^0. According to Kollias (1996), the reflected intensity is maximum when a light source is place 45^0 in front of the subject. A linear polariser coupled with an angle rotator is mounted in front of the Samsung Full HD camera lens. The camera was placed 80cm from the subject. Aperture setting for the camera was f/1.4. Two genuine subjects were used in this experiment who were different from the genuine face in the previous experiment in Section 3.3.1. Despite that, the same paper fake face, plastic fake face and rubber fake face were still in use.

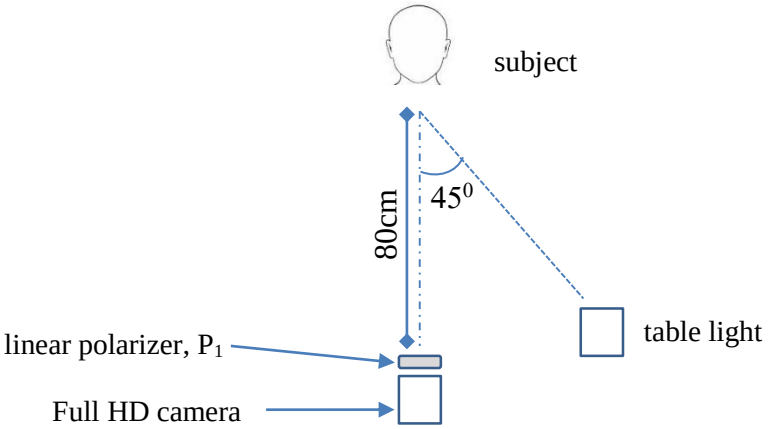

Figure 3.10: The experiment setup for the unpolarised table light source

Similar to the recording process in Section 3.3.1, images of each subject were recorded at four polarization angles: 0^0, 45^0,90^0 and 135^0, by manually rotating P_1. The recorded images were labelled accordingly to the polarization angles as Img_0, Img_{45}, Img_{90} and Img_{135}. At each polarisation angle, three frames of images are captured for each subject. Next, similar processes were repeated: (1) cropped the face region; (b) image aligned; (c) image registration; and (d) image averaging. The processed polarised images of the two genuine faces: R_1 and R_2; and the three fake faces are presented in Figure 3.11. As shown in Figure 3.11, a shadow formed on the right side of each image due to the position of the table light. Shadow is formed when an object blocks the light. The existence of the shadow suggests that a weak light intensity may occur on the right side of the images. To further analyse the polarised images, two parameters were used which were the Stokes parameters and the degree of polarisation.

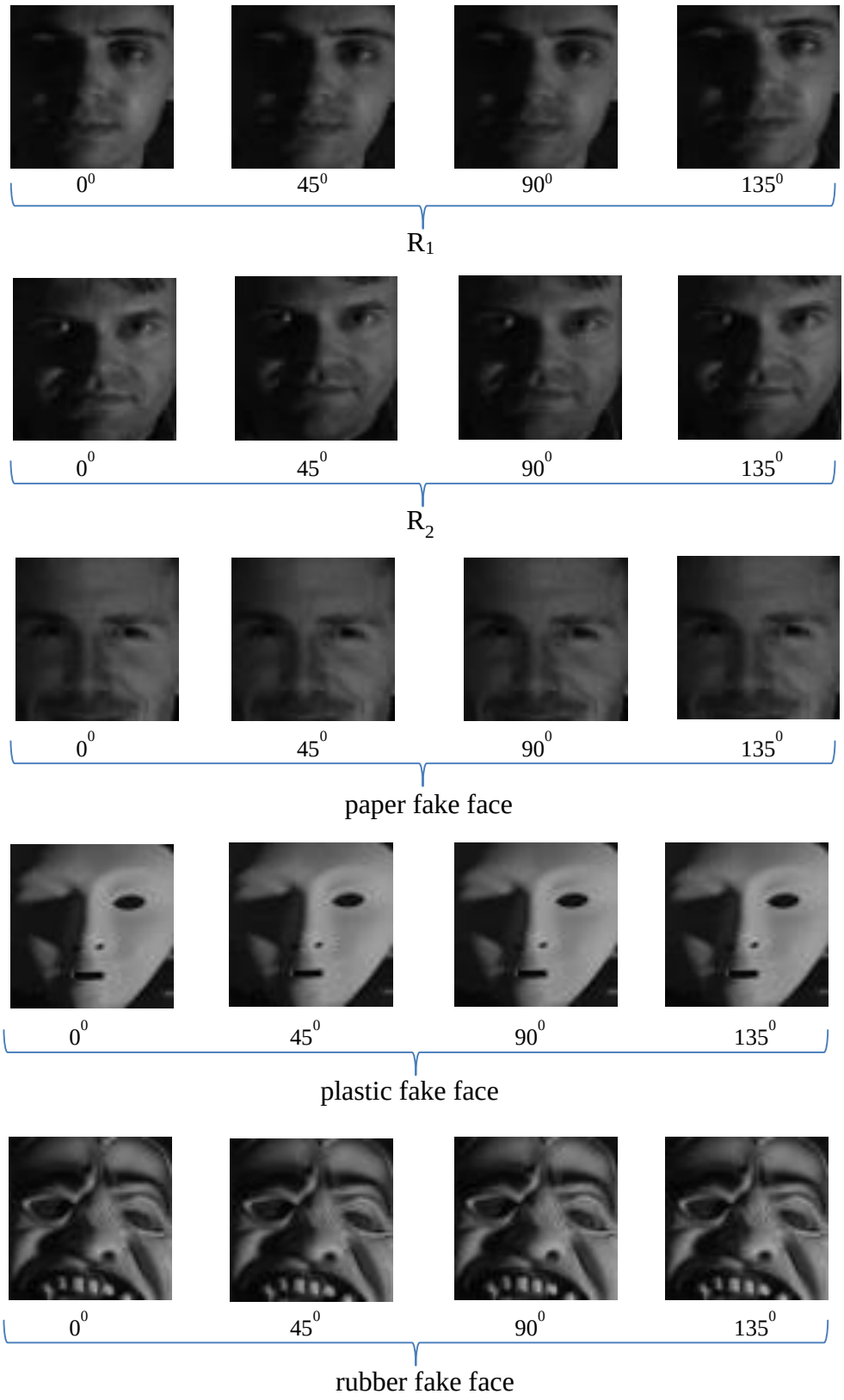

Figure 3.11: The polarised images of two real faces: R_1 and R_2; and three fake faces: paper, plastic and rubber; captured at four polarisation angles

a) The Stokes parameters

From the polarised images in Figure 3.11, the Stokes components were generated by using equation (3.2). Figure 3.12 lists the S_0, S_1 and S_2 components for each of the material. As can be seen from the figure, there is no significant difference in terms of intensity between S_1 and S_2 of the real and fake faces. Histograms are plotted and presented in Figure 3.13 in order to compare the pixels' intensity distribution between the subjects.

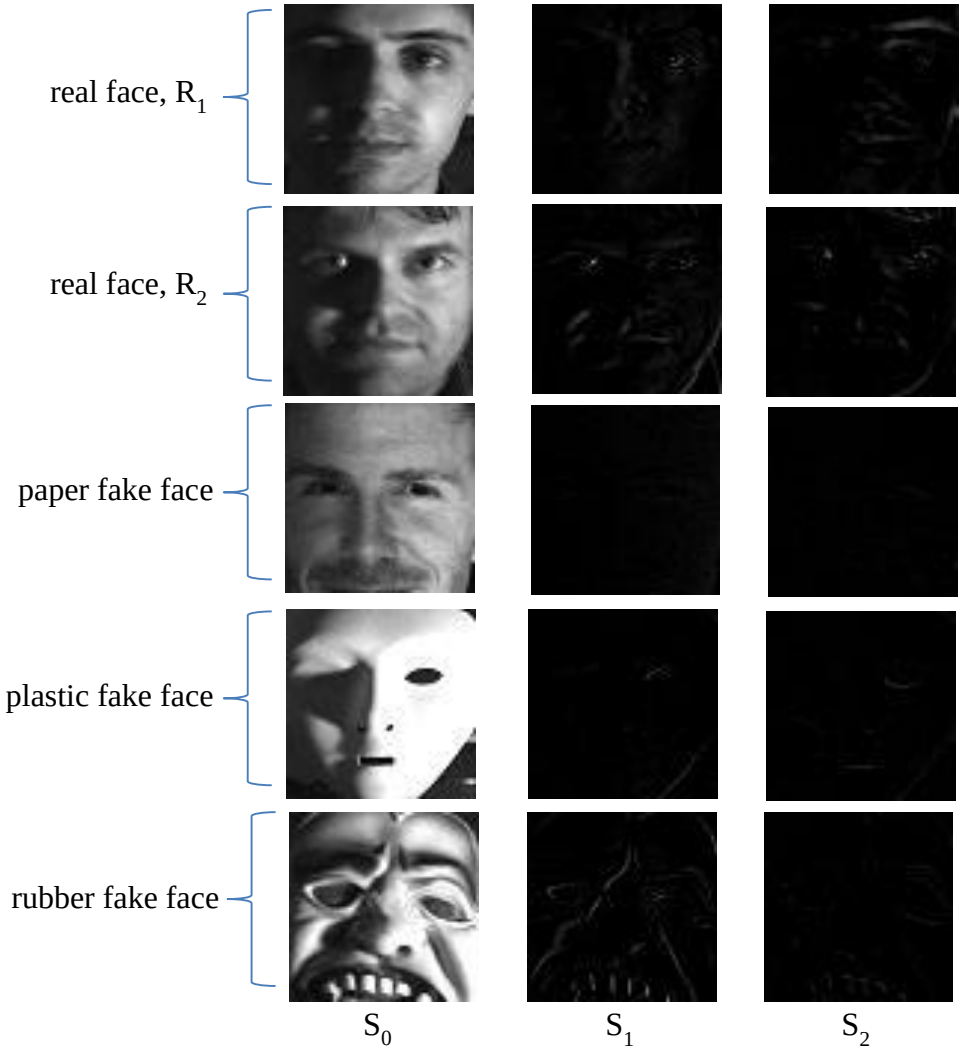

Figure 3.12: The Stokes components under unpolarised table light source

As can be seen from Figure 3.13, the shapes of the histograms for component S_0 of all subjects are quite similar. The pixels' intensity is widely spread with multi-modality distributions. Meanwhile, the other two components, S_1 and S_2 also show similar histogram shape. The distributions for S_1 and S_2 can be described as unimodal distributions which is positively skewed to the right with a short tail.

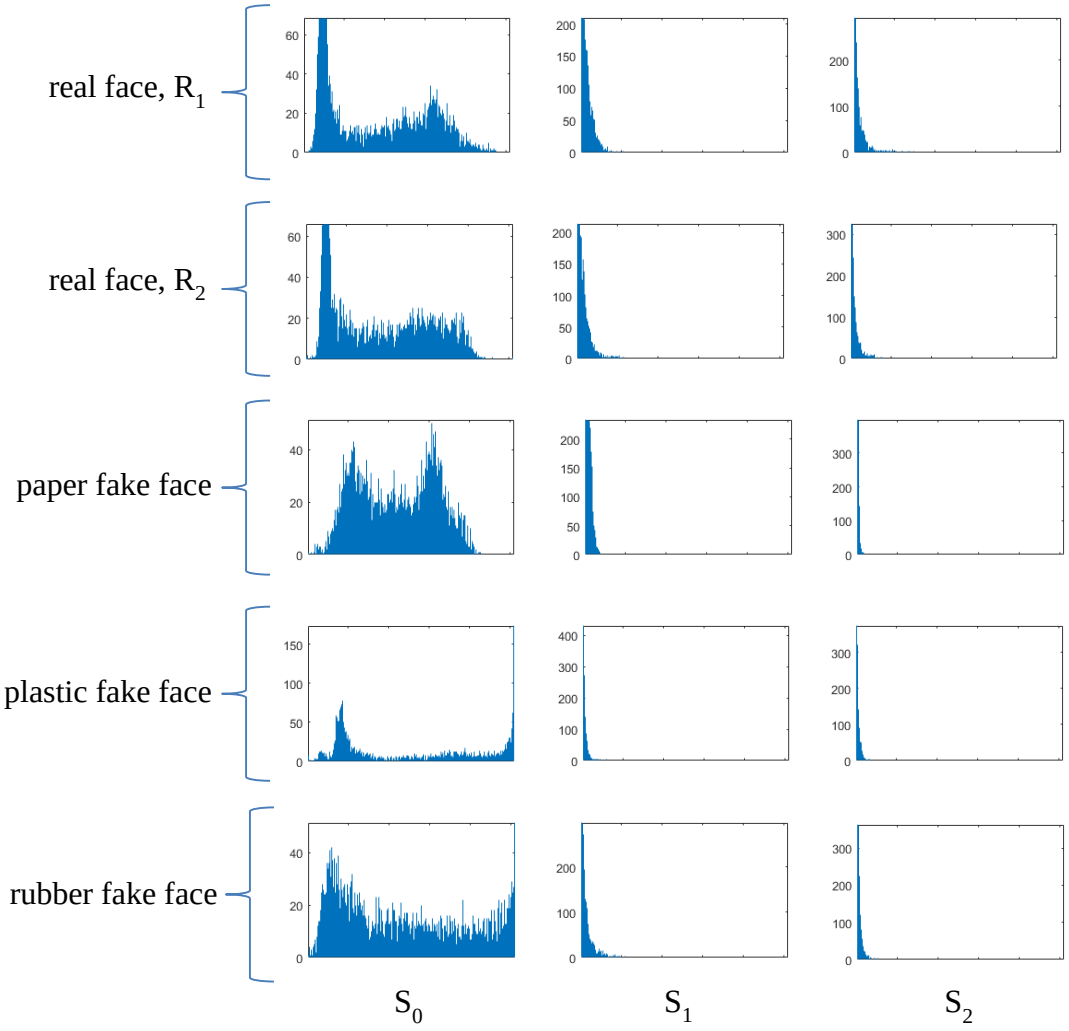

Figure 3.13: Histograms of the S_0, S_1 and S_2 for each real and fake faces under unpolarised table light

The investigation continued by generating the I_{SDOLP} for the real and fake faces. By using equation (3.3), the I_{SDOLP} for each material were generated based on the Stokes components in Figure 3.12. The I_{SDOLP} obtained can be compared in Figure 3.14. As was mentioned earlier, the experiment setup for this study locates a table light on the left side of the subject. Thus, the light beam illuminates mostly the left side of the subject in which shadow was formed on the right side. As can be seen in Figure 3.14, the right side of the I_{SDOLP} for each subject experienced some noise. To compare the distributions between I_{SDOLP} images, histograms are presented at the bottom of each I_{SDOLP} in Figure 3.14.

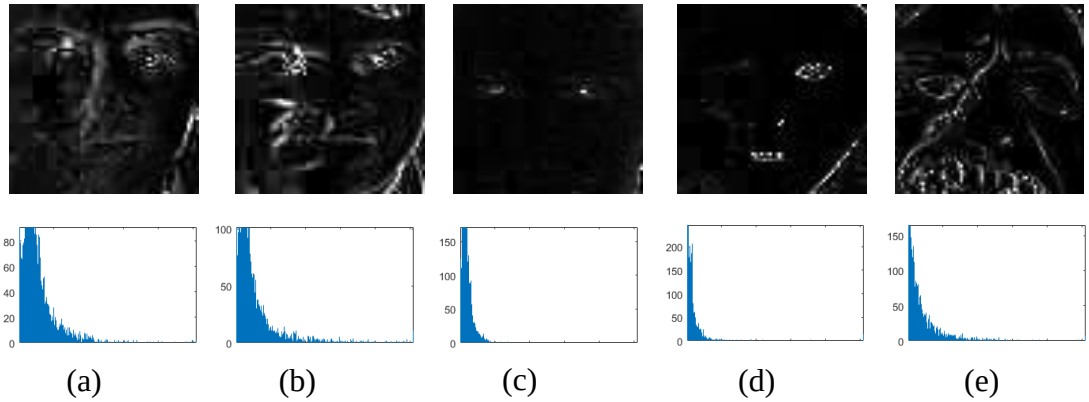

Figure 3.14: The I_{SDOLP} under unpolarised table light source for: (a) real face, R_1; (b) real face, R_2; (c) paper fake face; (d) plastic fake face; and (e) rubber fake face

The histograms show no clear difference of histograms shapes between the real and fake faces. The data distributions for all materials are described as skewed to the right; long tail for the two real subjects and the rubber fake face; short tails for the paper and plastic fake faces. In addition, the modality of all I_{SDOLP} is more to unimodal distributions. For further analysis, the I_{SDOLP} images were analysed statistically. The mean, the standard deviation, the skewness and the kurtosis were measured by using equation (3.9), (3.10), (3.11) and (3.12), respectively. The results of the statistical analysis are summarised in Table 3.3. As Table 3.3 shows, the mean value for R_1 and R_2 are higher than the fake faces. In contrast, the skewness and kurtosis of R_1 and R_2 are lower in value than the other materials. In addition, the value of standard deviation for all subjects are relatively similar.

Table 3.3: The statistical results for the I_{SDOLP}

	Real face R_1	Real face R_2	Paper fake face	Plastic fake face	Rubber fake face
Mean	26.34	26.60	9.08	7.20	18.36
Standard Deviation	26.75	36.18	10.94	22.81	30.75
Skewness	2.70	4.11	5.49	10.29	10.62
Kurtosis	11.36	26.40	34.44	122.69	139.4

b) The degree of polarisation

To measure the degree of polarisation, a polarisation image of each real and fake faces was created based on the images components in Figure 3.12. The polarisation image was produced by using equation (3.6) and the resulted image is known as I_{pol}. Figure 3.15 compares the I_{pol} images between the subjects. From the images in Figure 3.15, it is apparent that all images have low intensity value. Equations (3.9) - (3.12) were used to measure the mean of the intensity, the standard deviation, the skewness and the kurtosis of the I_{pol} images, respectively.

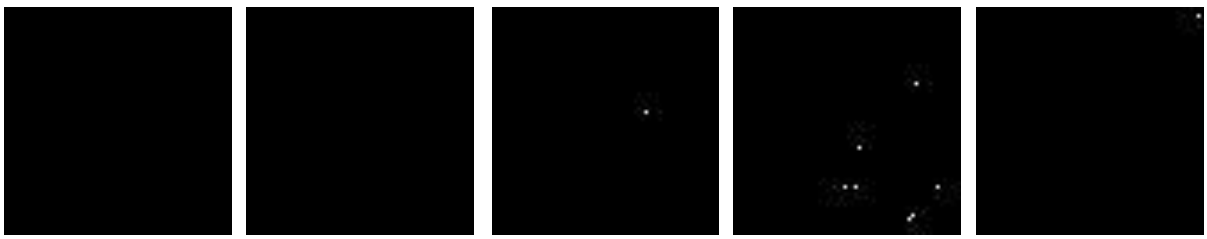

(a) (b) (c) (d) (e)

Figure 3.15: The I_{pol} images under unpolarised table light for: (a) real face, R_1; (b) real face, R_2; (c) paper fake face; (d) plastic fake face; and (e) rubber fake face

The results obtained from the statistical measures are summarised in Table 3.4. It is apparent from the table that the differences are not statistically significant. Data from this table can be compared with data in Table 3.2 which shows small amount of polarised reflected light from each of the subject. Overall, the degree of polarisation could not be used to separate between genuine and fake faces.

Table 3.4: The statistical results for the I_{pol} images

	Real face R_1	Real face R_2	Paper fake face	Plastic fake face	Rubber fake face
Mean	0.0029	0.0195	0.1155	0.7644	0.1121
Standard Deviation	0.0541	0.1436	4.039	10.689	4.047

3.4 Discussion and Conclusion

In this chapter, the study aims to determine the effect on the states of linear polarisation and the degree of polarisation to various material surfaces when unpolarised light sources were used. Two parameters which were the Stokes parameters and the degree of polarisation (DOP) were applied to measure the states of linear polarisation and the degree of polarisation for each subject. The first experiment was carried out by using unpolarised fluorescent ceiling light source with one genuine subject and three fake traits. The second experiment setup was designed based on the study to differentiate between transparent and opaque objects proposed by Mahendru and Sarkar (2012). Several changes have been made in the second experimental setup compared to the one proposed by Mahendru and Sarkar (2012): (1) table light sources; (2) subject-camera distance was increased to 80cm.

Two images components known as S_0 and S_1 were required to form a polarisation image, I_{pol}. These images were then statistically analysed and histograms of each of them were plotted. Under the unpolarised fluorescent ceiling light source, histogram of the S_0 images of the genuine face shows a different shape compared to histograms of the three fake faces.

However, the difference was not very encouraging because the number of samples used in this study was very small. In contrast, there is no significant difference of the distribution between histogram shapes of the five S_0 images under the unpolarised table light source.

The next discussion is about the Stokes parameters and the Stokes degree of linear polarization images (I_{SDOLP}) of all samples for both unpolarised fluorescent ceiling and table light sources. As was discussed earlier, the Stokes parameters were required to produce the SDOLP images, I_{SDOLP}. Figure 3.7 and Figure 3.12 illustrated the Stokes parameters: S_0, S_1 and S_2 under unpolarised fluorescent and table lights, respectively. These figures show similar pattern of S_0, S_1 and S_2 components: clear S_0 images and very dark S_1 and S_2 images. These components were then used to produce the I_{SDOLP} under both lighting types. The I_{SDOLP} images that were created are shown in Figure 3.8 and Figure 3.14. The I_{SDOLP} images from Figure 3.8 and Figure 3.14 do not show any significant difference between the real and fake faces. In addition, the pixels' intensity distributions as showed by the histograms of each I_{SDOLP} also seemed identical to each other. Therefore, the statistical analysis results on the I_{SDOLP} images under both light sources do not present much differences between the real and fake subjects.

Then, the I_{pol} image was generated by using equation (3.6) which was then examined statistically. The results showed that the mean intensity of all I_{pol} images under both unpolarised fluorescent ceiling and table lights was very small within the range value of 0.0029 to 0.1155. No significant difference was found between the genuine faces and the fake faces. In comparison with the study by Mahendru and Sarkar (2012), the transparent and opaque objects based on the DOP value of the transparent object were distinguished and it was found that the transparent object was higher than the opaque object. The differences could be used as the classification measurement. However, when similar unpolarised imaging system was applied to this study, no significant difference was found between the genuine and the fake faces. Moreover, the ratio of polarised reflected light to the total reflectance was very small and similar between the subjects. The different results achieved in this study compared to the study by Mahendru and Sarkar (2012) could be possibly explained as follows:

1. The specular reflection from the transparent object was highly polarized compared to the diffuse reflection from the opaque object. This clear difference provides significant classification results between the objects based on the degree of polarisation in the investigation done by Mahendru and Sarkar (2012).

2. The distance between the subject-camera and the subject-light source in the experiment carried out by Mahendru and Sarkar (2012) was closer compared to the experiments described in this chapter. The 25cm distance between subject-camera and subject-light source is practical to be used on non-live object not on live subject such as a human. Moreover, in a face recognition system, very close subject-camera requires full cooperation from the live human subject.

For record, the Stokes parameters and the Stokes degree of polarisation image (SDOLP) methods have not been applied in any previous study to compare human skin surface with the surface of objects. For instance, numerous studies attempted to distinguish between several materials using polarised light source and methods such as the Stokes parameters, the degree of polarisation and the Polarisation Fresnel Ratio [Sarkar et al. (2011); Hua and Wolff (1996); Wolff (1990); Wolff and Boult (1991)]. Apart from that, several studies have examined polarised image to separate the surface and subsurface reflections that emerge from the skin. All of these assessments used polarised light source in the polarisation imaging systems compared to the experiments presented in this chapter which applied unpolarised light sources. None of the degree of polarization (DOP) results were statistically significant and the I_{SDOLP} images were similar between the real and fake faces. These findings while preliminary, suggest that polarised light source is compulsory in any polarisation imaging system. Another limitation of this study is that the number of the subjects and the mask used did not mimic a real person's face.

The above suggested that polarised light source should be attempted in the polarisation imaging system. The results suggest that unpolarised light source does not contribute to a polarisation imaging system. In addition, an issue that emerged from the findings is to find a solution to avoid the existence of shadow on the images. To get a convincing result, more subjects are required. The use of fake faces that represent the original faces are therefore suggested for the next study.

Chapter 4: Visible Light Polarisation Imaging Systems

4.1 Introduction

Previous studies have reported that facial skins and mask materials can be distinguished by exploiting the differences of their reflectance [Kim et al. (2009), Zhang et al. (2011)]. These two studies investigated the reflectance differences between real faces and mask materials by examining the distribution of the albedo values under different wavelengths. These proposed methods were reported to have high accuracy for fake detection, however, the mask attacks used did not mimic the real subjects. For instance, the face masks used were made of silicon, latex, plastic which could be randomly obtained from a general market. Similar types of face masks were used in spoofing trials in Chapter 3. None of the masks mimic a real person's face thus the context of the analysis was more to differentiate between materials rather than spoofing. Additionally, the experiments in Chapter 3 have significantly failed to prove that the normal light source can be applied to evaluate the Stokes degree of linear polarisation (SDOLP) and the degree of polarisation for all real and fake faces. Thus, no classification method has been proposed in Chapter 3.

It has been assumed by Hadid (2014) that no single countermeasure is able to detect all types of spoofing attacks in real-world applications. Each counter measure was developed for a recognition system specifically to deal with certain types of threat. The system is likely to face difficulty if different types of fraud were imposed on the system. For instance, motion-based approaches try to find any movement, e.g., eyes blinking and lips movement in the video sequence. This motion-based spoofing counter measure system, however, cannot effectively be used in any static scenarios [Galbally et al. (2014)]. Similarly, other anti-spoofing techniques that is subjected to one type of counter measure method also cannot effectively be used in any static scenarios. For example, texture based approaches were proposed to extract image artefacts in fake face images, e.g., photo and replayed video attacks. These methods have been experimentally proved capable to distinguish fake faces from genuine faces within particular databases but the performance dropped when similar methods were applied to a different face spoof database [Wen et al. (2015)].

As investigated in Section 3.3.1 and Section 3.3.2, the results suggested that a polarisation imaging system may need a polarised light source. The SDOLP images generated by using polarised images captured under unpolarised imaging system have shown relatively similar histograms. Thus, no spoofing face was detected. In this chapter, the proposed anti-spoofing face detection algorithms based on the Stokes degree of linear polarisation image, I_{SDOLP} and the polarisation image, I_{pol} presented in Figure 1.2, were applied as trials to distinguish between real and fake faces. As can be seen from Figure 1.2, two types of face attacks that resemble the real subjects were used as the attempts to cheat this self-made 2D polarisation face imaging system. Firstly, iPad screen was used to display faces of legitimate users and secondly, photo of the real user's face printed on an A4 matte paper, was placed in front of the camera as trials to gain access. The genuine subjects were also involved in the recognition processes. These three types of materials were then going through several processes: crop, align, resize and average. The polarised intensity features of each processed image were analysed based on the two proposed parameters: the Stokes parameters and the DOP. The decision on whether the sample is genuine or not was determined based on the results of the parameters.

This chapter is organised as follows. In Section 4.2, spoofing face detection method is discussed based on the polarisation images captured under an updated polarisation imaging system compared from the one previously used in Chapter 3. The polarisation imaging system proposed in Section 3.3.2 used a table light placed on the right side of the subject. As a result, the recorded images were half-covered with shadows due to the position and the number of light source. Thus, in this chapter, two table lights were used and placed on the right and left side of the subject to avoid shadows [Kollias (1996)]. The Stokes degree of linear polarization (SDOLP) and the degree of polarisation (DOP) parameters were applied as trials to differentiate between a real face and an iPad attack. Results and discussion are presented at the end of the section. The next major section is Section 4.3. In this section, similar polarisation imaging system as implemented in Section 4.2 was employed. By using printed photo faces, the SDOLP and the DOP parameters were measured between the real and photo faces. However, due to some similarities in the results, a new detection algorithm named as the SDOLP fast fusion formula (SDOLP3F) is proposed and discussed at the end of Section 4.3. Finally, summary is later presented in section 4.4.

4.2 Spoofing Face Detection between Genuine Face and iPad Displayed Face

Face biometric system is vulnerable to spoofing attacks compared to any other biometrics traits such as finger prints and iris due to the relatively easier way to acquire a legitimate user image or video in front of the sensor by using a digital device or a printed photo [Wen et al. (2015)]. For instance, Samsung Galaxy and iPad are two popular tablets used throughout the world in which both screens are known as liquid crystal display (LCD). As was explained earlier, LCD screen emits its own linearly polarised light which means that the transmitted light wave from the LCD screen vibrates in a single direction either parallel or perpendicular to any plane of surface in front of the screen. By contrast, human real face produces multi-reflections (surface and diffuse) when the skin is illuminated by any source of light. These reflections can be separated by adopting polarised light in an imaging system. Therefore, these different characteristics between the genuine face and LCD screen could be exploited in the next classification trials. By using self-made 2D polarisation imaging system, the images captured were analysed based on their reflectance features by using the degree of polarisation (DOP) and the Stokes parameters.

4.2.1 Experiment Setup

As was briefly introduced in Section 4.1, the polarisation imaging system used in this study consisted of two table lights: one is placed 50cm to the right and the other 50cm to the left of the camera. Light bulbs used was extra warm white light with 2700k. The lights were adjusted to illuminate the subject at an angle of 45^0. Each of the table light was coupled with a linear polariser in the form of a thin piece of sheet, denoted as P_2 and P_3. Both of the polarisers were aligned parallel to each other. Therefore, the table lights wave travelled in the same direction towards the subject. The camera used in this experiment was Samsung Full HD camera placed 80cm in front of the subject as shown in Figure 4.1. Aperture setting for the camera was f/1.4. One linear polariser made of glass, P_1, coupled with an angle rotator, was placed in front of the camera lens. The angle rotator was used to adjust the polarisation angle during the image recording process. The determination of the positions of P_1, P_2 and P_3 was explained in Section 3.1.3. For record, the recording process was carried out in a dark room to

control the illumination. Hence, the intensity of the polarisation images was caused only by the polarised light source.

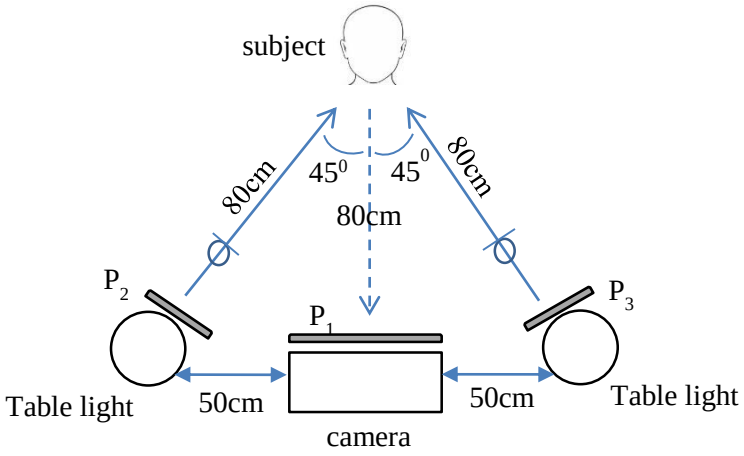

Figure 4.1: The Visible Light Polarisation Imaging System

4.2.2 Dataset

To the best of the author's knowledge, polarised spoofing face database is not yet publicly available. In order to validate the effectiveness of the proposed method, a set of polarized images was captured by using the measurement setup as shown in Figure 4.1. In this study, dataset of genuine faces and iPad displayed attacks of eight people were developed. The real faces consist of five females and three males of two skin colours: Asian and Caucasian. This self-developed dataset was named as Face-iPad dataset. Firstly, the recording was carried out without any polariser either in front of the camera lens or the table lights. The image of each subject was captured and stored in an iPad to be later displayed as spoofing attempt. After that, the three linear polarisers were mounted each in front of the camera lens and the two table lights as in Figure 4.1.

By manually rotating P_1, images of each real face were recorded at four polarisation angles: 0^0, 45^0,90^0 and 135^0. The recorded images were labelled as Img_0, Img_{45}, Img_{90} and Img_{135}, respectively. Similar to the previous experiments in Chapter 3, three frames of images were captured at each polarisation angle. For the spoofing attempt, face images that was

captured at the beginning of this experiment, were displayed on an iPad screen in front of the camera at the subject-camera distance of 80cm as stated in Figure 4.1. These iPad displayed faces were also recorded three frames each. SURF algorithm in Section 3.3.1 was then applied to register and align the real and fake images. The aligned images were averaged in order to reduce noise. One final processed polarised image was produced for each subject and polarisation angle. Figure 4.2 presents the structured Face-iPad dataset. From the hierarchy graph shown in Figure 4.2, the total captured polarised images for the real faces and the iPad displayed faces at all polarisation angles were 192 images. In addition, the total number of final processed polarised image for each real and fake traits was 64. In total, there were 256 images in the Face-iPad dataset.

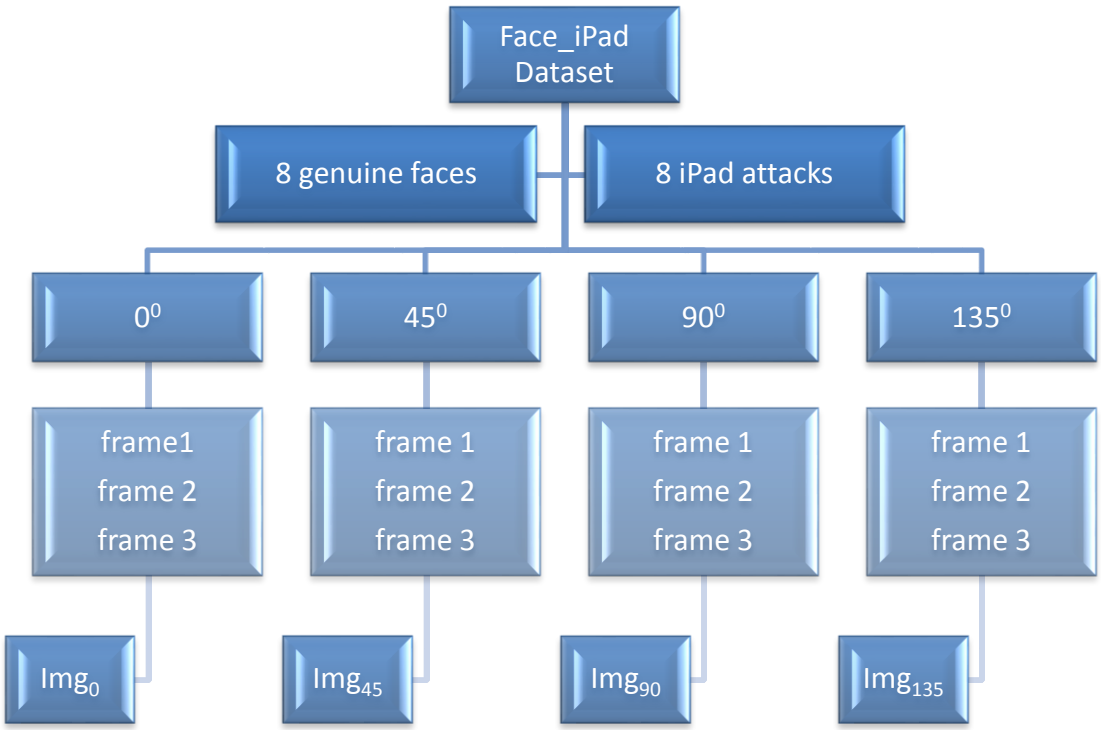

Figure 4.2: The structured Face-iPad dataset

For the purpose of analysis, polarised images of one real subject and one iPad face are presented throughout this section. To begin with, RGB images captured at each polarisation angle for one genuine subject together with iPad displayed faces of the same subject are presented in Figure 4.3(a). Noted that these images have been cropped from the original scene but have not been processed. The top row in Figure 4.3(a) shows the RGB images of the genuine face and the second row lists the RGB images of the iPad attacks. Images from left to right are labelled as F_0, F_{45}, F_{90} and F_{135} for the real subject and iP_0, iP_{45}, iP_{90} and iP_{135} for the iPad display, respectively in accordance with polarisation angles. Since these images were captured at different polarisation angles, they might suffer from image misalignment between the three frames. To overcome this problem, the three images for each angle were registered using the SURF image registration algorithm. The SURF algorithm was programmed in MATLAB with the Image Processing Toolbox. After the alignment process, an average image was generated by adding the three registered images and averaged them. Image averaging could also help to reduce random noise. The final processed polarised images are presented in Figure 4.3(b). As can be seen in Figure 4.3(b), the processed polarised images for both real face and iPad display are presented as grayscale images. Due to the image registration process, the RGB images in Figure 4.3(a) needed to be converted to grayscale format.

As Figure 4.3(a) shows, the intensity of F_0 is greater than the F_{45}, F_{90} and F_{135} images. F_0 image was taken under parallel polarisation axis whereas F_{90} was recorded under perpendicular polarisation axis. The determination of these polarisation axes was explained in Section 3.1.3. Whereas images captured under parallel polarisation consist of both surface and subsurface reflections, perpendicular polarised images have only subsurface reflection [Matsubara et al. (2012)]. This explains why the F_0 image looks shinier compared to the F_{90} image. Besides that, F_{45} and F_{135} images also show slight intensity differences between each other.

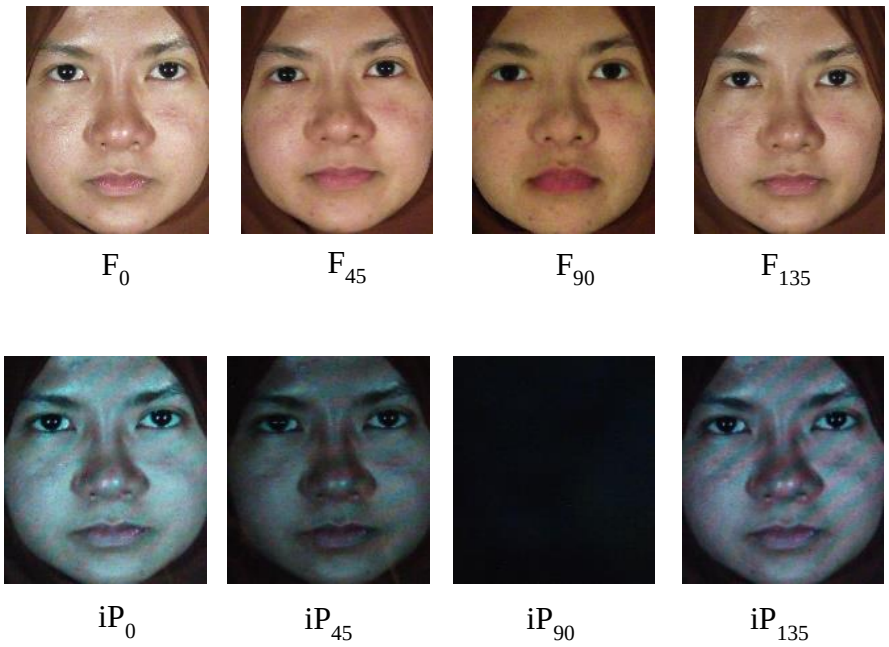

(a) RGB polarised images of real face and iPad displayed face

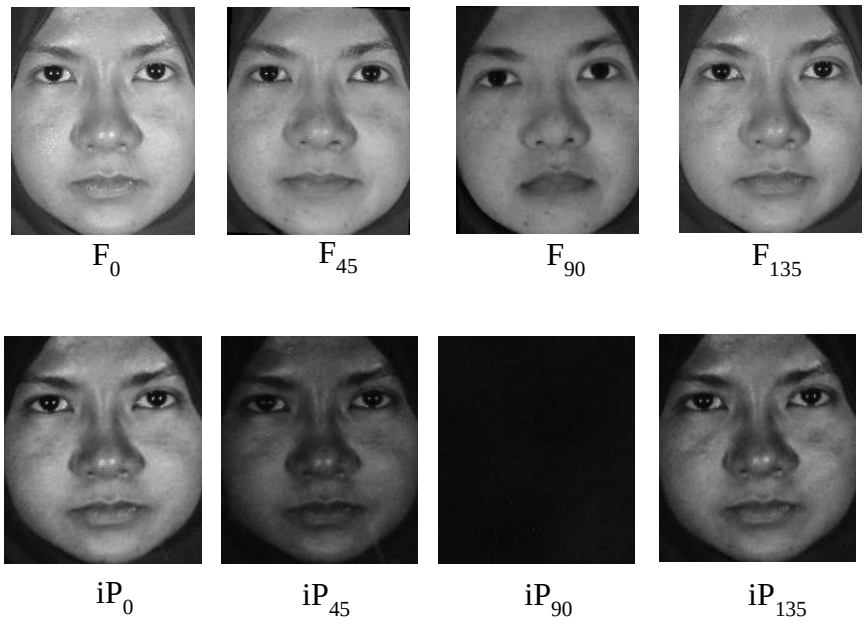

(b) grayscale polarised images of real face and iPad displayed face

Figure 4.3: Sample of polarised images in Face-iPad dataset

Let us turn now to the coarse comparison between polarised images for the iPad display faces. As can be seen in Figure 4.3(a), there is clear difference between iP_0 and iP_{90} images. Both were taken at 0^0 and 90^0 polarisation angles that were perpendicular to each other. Interestingly, the iP_{90} image turns to be a dark image because the light wave was blocked from passing through the linear polariser, P_1. Comparing the iP_{90} with F_0, the F_{90} image is completely clear and visible. Driven by these initial polarised images, iPad display attack could be easily detected by using cross polarisation in which no light wave is allowed to pass through the P_1. The iPad image will become dark at this point and prove that it is an iPad attack.

Another possible explanation for the dark iP_{90} image might be related to phenomenon known as the interference of waves. Interference happens when two or more waves come together as they travel through the same medium. Interference could occur at any location along the medium where the waves such as sound, water and electromagnetic waves travel [Duffy (2000)]. In this study, two table light sources were used in which each of them was coupled with a linear polariser to produce linear polarised light wave. The polarised light wave was emitted towards the iPad screen which also emitted polarised light from its inside. Therefore, it is possible to hypothesise that interference are more likely to occur between the light waves. There are two types of interference: constructive interference and destructive interference. Constructive interference occurs whenever waves with the same oscillations direction meet each other resulting larger amplitude at the meeting point than the individual wave amplitude. In contrast, destructive interference happens when the interfering waves are vibrating in the opposite direction and completely cancel each other out. Figure 4.4 illustrates the two types of wave interference. As shown in Figure 4.4, two waves are constructively interfered when a crest meets a crest or a trough meets a trough, destructive interference occurs when a crest meets a trough.

There are a number of conditions to be satisfied for light waves to interfere either constructively or destructively [Sirohi (1993)]. Firstly, the interfering waves should be coherent, in which they possess a constant phase difference within the waves. Laser light is an example of coherent light. Secondly, the waves should be of a single wavelength or also known as monochromatic waves. The third condition is that the waves must have the same state of polarization. The traveling waves have to satisfy these three conditions in order to interfere each other. Otherwise, interference cannot occur. In this study, the lighting sources used were table lights which were denoted as incoherent light. These table lights are considered as visible

light with wavelength range of 400 – 700 nanometers (nm) which is not considered as single wavelength. Although the first and second interference conditions have failed to be met, the third condition still needs to be discussed. According to Xia (2014), Fresnel-Arago laws are three laws which summarise properties of interference between polarized lights. These laws emphasize that polarized light waves have to be obtained from coherent light source to allow interference. Taken together, the properties of the two light waves in this study did not meet the three interference conditions. Thus, the waves did not interfere and did not contribute to the low intensity value of the iPad display images.

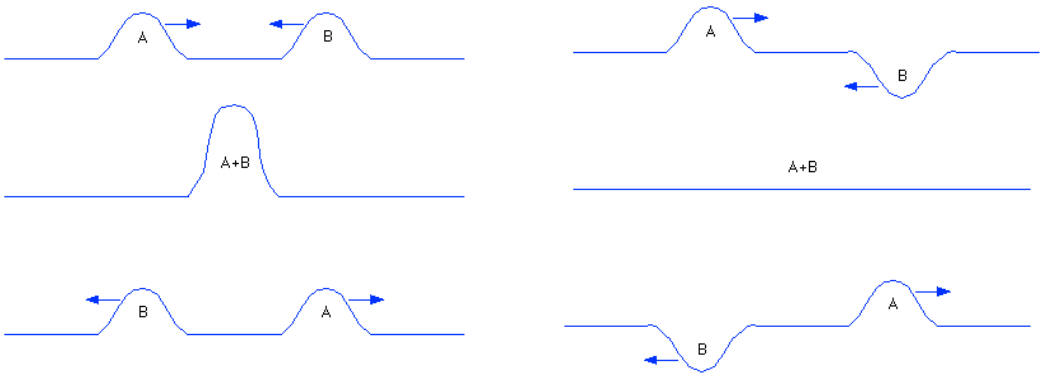

Figure 4.4: Constructive and destructive interference

There are a number of conditions to be satisfied for light waves to interfere either constructively or destructively [Sirohi (1993)]. Firstly, the interfering waves should be coherent, in which they possess a constant phase difference within the waves. Laser light is an example of coherent light. Secondly, the waves should be of a single wavelength or also known as monochromatic waves. The third condition is that the waves must have the same state of polarization. The traveling waves have to satisfy these three conditions in order to interfere each other. Otherwise, interference cannot occur. In this study, the lighting sources used were table lights which were denoted as incoherent light. These table lights are considered as visible light with wavelength range of 400 – 700 nanometers (nm) which is not considered as single wavelength. Although the first and second interference conditions have failed to be met, the third condition still needs to be discussed. According to Xia (2014), Fresnel-Arago laws are three laws which summarise properties of interference between polarized lights. These laws

emphasize that polarized light waves have to be obtained from coherent light source to allow interference. Taken together, the properties of the two light waves in this study did not meet the three interference conditions. Thus, the waves did not interfere and did not contribute to the low intensity value of the iPad display images.

From the discussion on the light interference above, the remaining reason that caused the low intensity values for the iP_{90} image is the P_1 polarisation axis. P_1 was a linear polariser mounted in front of the camera lens. As can be seen in Figure 4.3, iP_{90} image is a dark image captured at 90^0 polarisation angle. This shows that the polarised light emitted from the iPad screen was perpendicular to the polarisation axis. Thus, the traveling perpendicular light wave from the iPad was stopped by polariser P_1 from transmitting through. The camera captured iP_{90} without any light transmitted. This is a significant positive correlation between lights emitted from iPad screen and the polarisation angle of P_1. The differences between the F_{90} and iP_{90} images can be easily used to distinguish between the real face and the iPad attack. However, it is interesting to further investigate using the DOP and the SDOLP parameters applied in the previous chapter as trials to differentiate between genuine and fake faces.

4.2.3 The degree of polarisation

In contrast to the analysis that was carried out in Chapter 3, polarised images in the Face-iPad dataset were firstly analysed using the degree of polarisation (DOP) parameter instead of the SDOLP parameter. As was discussed in Section 3.1.3, I_{max} is an image taken under 0^0 polarisation angle, and I_{min} is an image captured under 90^0 polarisation. These two images were denoted as I_0 and I_{90}, respectively. By using equation (3.6), polarisation image, I_{pol} of the real faces and the iPad display faces were generated. Figure 4.5 presents the S_0 and S_1 image components used to generate the polarisation image, I_{pol}. To avoid confusion, the polarisation image of the real face and the iPad displayed face were labelled as F_{pol} and iP_{pol}, respectively.

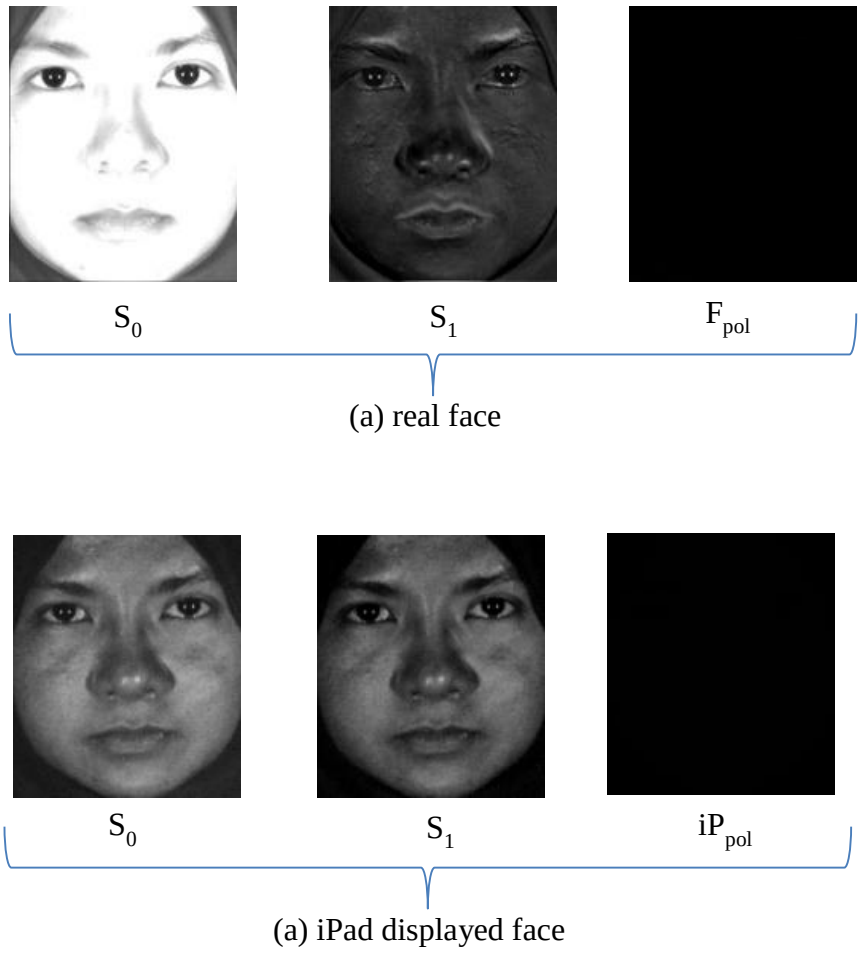

Figure 4.5: The S_0 and S_1 image components and the I_{pol}

Sarkar et al. (2011) had successfully differentiate plastic and aluminium based on the DOP values of each material. In another study, Mahendru and Sarkar (2012) once again claimed that the DOP value could be used to differentiate between opaque and transparent objects. In this experiment, however, as can be seen in Figure 4.5, there is no significant difference between the F_{pol} and iP_{pol} images. To further confirm the assumption that the F_{pol} and iP_{pol} are relatively similar, statistical analysis was used. The results of the mean, standard deviation, skewness and kurtosis are illustrated in Figure 4.6. From the plots in Figure 4.6, it can be seen that the mean intensity values for each polarisation image are very small in between 0 and 0.9. However, the differences of the four measurements values between F_{pol} and iP_{pol} are quite significant. Thus, the threshold value which is represented by the green dotted line, is selected for each measure. The polarisation image, I_{pol} is identified as real face if the mean and standard deviation values are less than the corresponding values. Furthermore, the skewness

and the kurtosis values are not applicable due to the very low intensity values of each I_{pol}. Then, the detection rates for the mean and standard deviation were calculated based on a confusion matrix as shown in Table 4.1.

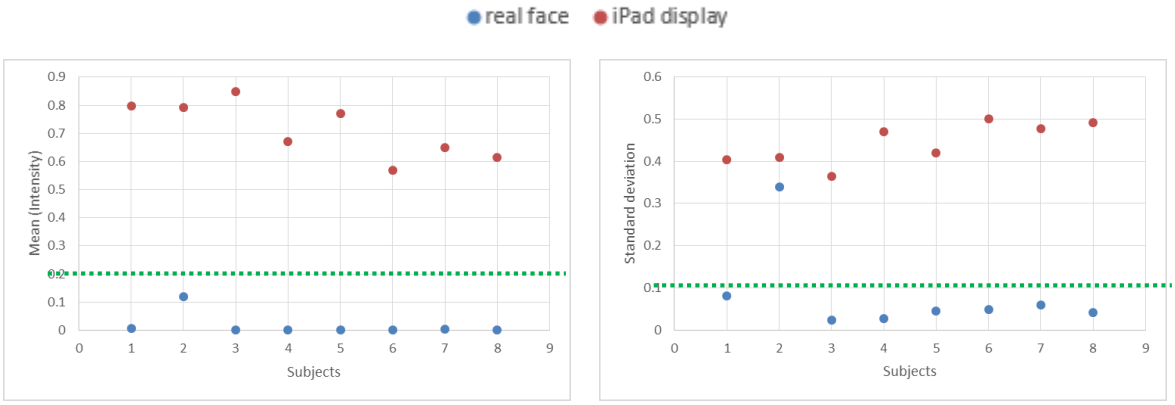

Figure 4.6: The statistics analysis for F_{pol} and iP_{pol}

From the matrix in Table 4.1, four possible predictions can be made. Firstly, the true positive (TP) is the case in which the statistics scores meet the prediction that the material is a genuine face. Secondly, the true negative (TN) is the state in which statistical scores of a fake face meet the fake trait prediction. Thirdly, the prediction says that the material should be a real face but the scores do not comply with the prediction. The third case is known as the false positive (FP). Finally, the false negative (FN) is when a material is predicted as fake trait, however, the scores show that the material is a genuine face. To classify the materials into two groups (real face or fake face), the confusion matrix is applied as a binary classifier.

Table 4.1: The confusion matrix for the spoofing face detection

	Predictions		
Actual Image	Real face	Fake face	
Real face	True positive (TP)	False negative (FN)	∑ real face
Fake face	False positive (FP)	True negative (TN)	∑ fake face
	∑ test outcome positive	∑ test outcome negative	

The results which were based on the predetermined threshold as illustrated in Figure 4.6, are presented in Figure 4.7. In Figure 4.7, the prediction results were presented individually according to the statistical scores: (a) mean; and (b) standard deviation. The total number of I_{pol} images computed in the confusion matrix denoted as *n* are 16 images. The sixteen I_{pol} images consist of eight F_{pol} and eight iP_{pol}.

n = 16	Predicted: Real face	Predicted: iPad display	
Actual: Real face	8	0	8
Actual: iPad display	0	8	8
	8	8	

(a) mean

n = 16	Predicted: Real face	Predicted: iPad display	
Actual: Real face	7	1	8
Actual: iPad display	0	8	8
	7	9	

(b) standard deviation

Figure 4.7: The predictions scores based on the statistical measures

From the data in Figure 4.7, the true positive rate (TPR) and the false positive rate (FPR) were calculated. TPR is a frequency rate of the true predictions for the actual material. On the other hand, FPR is a frequency rate of the false predictions for the actual material. The TPR and the FPR were computed as follows:

$$\begin{aligned}&\text{True positive rate (TPR)} = \sum \text{True positive (TP)} / \sum \text{real face}\\&\text{False positive rate (FPR)} = \sum \text{False positive (FP)} / \sum \text{fake face}\end{aligned} \tag{4.1}$$

Besides the TPR and FPR, the accuracy (AC) which is the proportion of the total number of correct predictions, can also be used to measure the performance of a measure. The accuracy is determined by using the equation:

$$Accuracy\ (AC) = \frac{\mathrm{TP} + \mathrm{TN}}{\mathrm{TP} + \mathrm{FN} + \mathrm{FP} + \mathrm{TN}} \tag{4.2}$$

where TP is true positive, TN is true negative, FN is false negative and FP is false positive as shown in Table 4.1.

The detection rates are then presented in Table 4.2. The results, as shown in Table 4.2, indicate that all iP_{pol} images was correctly identified as iPad displayed attacks based on the 0% false positive rates (FPR). Furthermore, the mean scores 100% for both TPR and AC. The standard deviation shows 87.5% TPR and 93.75% AC. Driven by these results, the degree of polarisation (DOP) parameter have the potential in detecting iPad displayed face attacks based on the statistical measures of the polarisation images. Besides that, due to the low intensity values, histograms for both F_{pol} and iP_{pol} images could not be generated.

Table 4.2: Detection rates for the statistical measures of the I_{pol} between real faces and iPad displayed faces

	TPR	FPR	Accuracy (AC)
	in percentage (%)		
Mean	100	0	100
Standard deviation	87.5	0	93.75

The results above will now be compared to the findings of previous works. Sarkar et al. (2011) distinguished plastic object from the aluminium object. Then, Mahendru and Sarkar (2012) once again successfully differentiated between transparent and opaque objects. Both results were based on the DOP values of the materials. There are several possible explanations for these results. The polarisation of the reflected light depends on the properties of the object surface. In accordance to the surface properties of the object, the difference between transparent and opaque objects is physically obvious. Transparent object such as glass not only allows light to transmit but also reflects light. The reflections from a transparent object have been reported to be mostly specular while an opaque object's reflections are diffuse [Mahendru and Sarkar (2012)]. The difference between transparent object and the opaque object's reflections have also produced different DOP values to each of the objects. In the experiment to distinguish between plastic and aluminium objects, the DOP values was successfully differentiated between the two materials [Sarkar et al. (2011)]. There is a significant difference between plastic and aluminium objects that has contributed to the values of the DOP. Aluminium surface is a metallic surface and also a conductor while plastic is

classified as an insulator. The DOP value of a highly conductive object is lower than the DOP value of a non-conductor object. These differences were used as a classification method among the two objects.

Surprisingly, the findings of the DOP values between human genuine face and iPad displayed faces in this section are supported by studies conducted by Sarkar et al. (2011) and Mahendru and Sarkar (2012). To the best of the author's knowledge, no study has been done on the degree of polarisation on human skin surface. Unlike the materials used in the experiments by Sarkar et al. (2011) and Mahendru and Sarkar (2012), physical properties of the real faces and iPad displayed faces used in this section were relatively similar. For instance, these three materials have been classified as insulators [St. Rosemary Educational Institution (2017)]. Moist human skin is identified as a fair conductor, however, the real human skins used in this study were dry thus they were not conductors. The iPad screen was made of glass which is an insulator and emits its own polarised light. Despite these similarities, statistically, by using the DOP, the iPad displayed faces were able to be distinguished from the real faces. In next section, further research was carried out by using the Stoke parameters as trial to distinguish between real face and iPad attack.

4.2.4 The Stokes parameters

Let us now investigate on the state of polarisation for genuine face and the iPad displayed face. As was discussed in Section 3.2.1, the state of polarisation of reflected light wave can be described in terms of the Stokes parameters. The Stokes parameters consist of four components: S_0, S_1, S_2 and S_3; and each of them represents distinctive value of the light intensity, the degree of polarisation, the plane of polarisation and the ellipticity polarisation, respectively. However, since linear polarisation was used throughout this study, component S_3 was omitted. A number of studies have found that the degree of polarisation can be used to distinguish between materials: plastic and aluminium [Sarkar et al. (2011)]; transparent and opaque objects [Mahendru and Sarkar (2012)]; and metal and dielectrics [Wolff (1990)]. To the best of the author's knowledge, none of the previous studies applied the Stokes parameters to measure the degree of polarisation between a genuine human face and a fake face particularly in a face biometric system. Rudd et al. (2016) proposed a hypothesis of using

polarised light to reject a presentation attack. A preliminary proposal with no parameter was implemented to measure the difference between a legitimate user and a fake face. However, similar approaches have been exploited in studies mostly in medical field. For instance, polarised light was adopted to eliminate the surface reflection of the skin surface so that the abnormal skin tissue underneath could be clarified [Bin et al. (2007)]. Many more studies on human skin reflections from the medical point of view have been carried out by using polarisation method. The details were explained in the literature review.

Polarised images from the Face-iPad dataset as presented in Figure 4.3 were used in the investigations throughout this section. Similar to the experiments in Chapter 3, only linear polariser was used in this study. Therefore, three Stokes components: S_0, S_1, and S_2; were created by using equation (3.2). These Stokes components were then used to generate the SDOLP image which was labelled as I_{SDOLP} by using equation (3.3). Figure 4.8 compares the Stokes components in the form of images of a real face and an iPad displayed face. As depicted in Figure 4.8, the Stokes components of an iPad face seems similar to each other. The Stokes components for the genuine face are significantly different compared to the iPad's Stokes components.

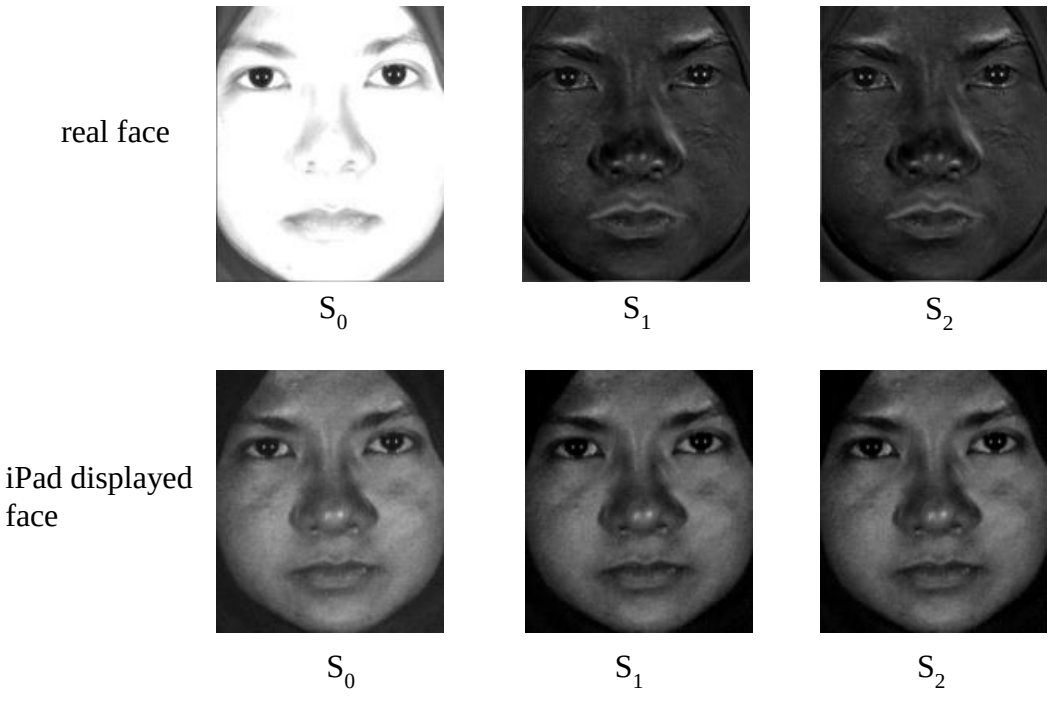

Figure 4.8: The Stokes components

Given that the number of subject in the Face-iPad dataset was small in which there were only eight real subjects and eight iPad displayed faces, Figure 4.9 compares four of the I_{SDOLP} images between real and fake faces. Apparently, very significant difference can be identified in Figure 4.9 between I_{SDOLP} of the real and iPad displayed faces. To measure the dissimilarity, statistics measures were used: the mean, standard deviation, skewness and kurtosis. Equations (3.9) to (3.12) were used to calculate the values for each of these measures, respectively. The results are plotted in Figure 4.10.

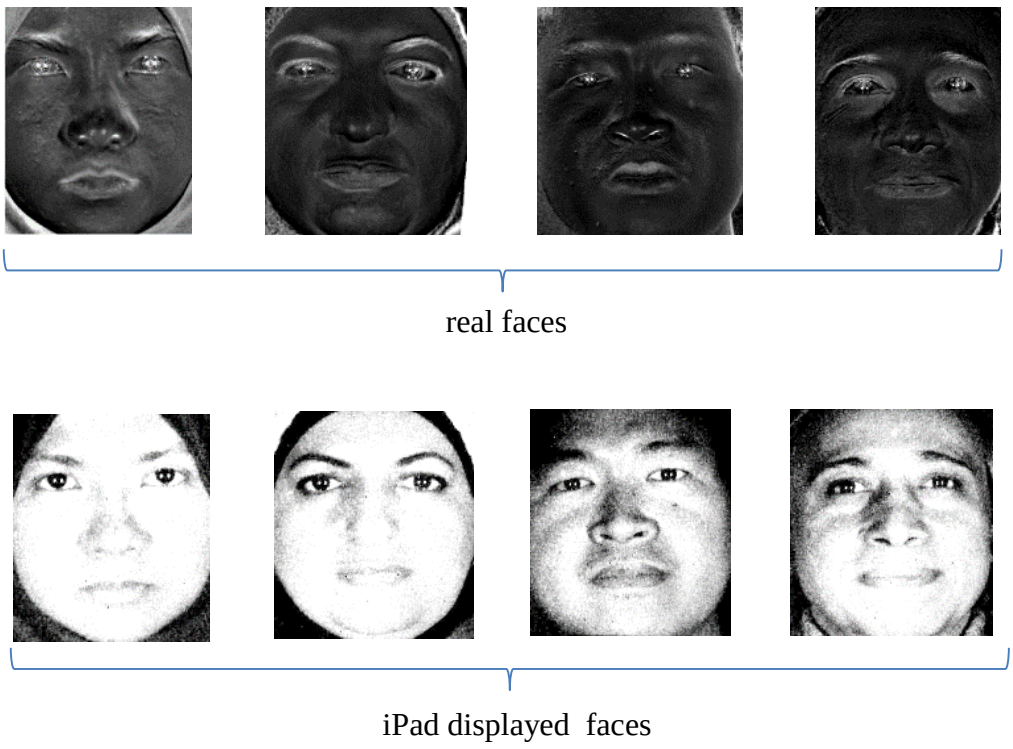

Figure 4.9: The I_{SDOLP} for the real faces and iPad displayed faces

From the plots in Figure 4.10, it is apparent that the differences for the mean, standard deviation, skewness and kurtosis between the real faces and iPad attacks are very significant. These plots are consistent with the assumption above that I_{SDOLP} between the real and fake faces seem very unlikely. Thresholds are assigned for each measure as represented by the dotted green line in Figure 4.10. The I_{SDOLP} is identified as real face if the measures values less than the corresponding threshold. Otherwise, the I_{SDOLP} is denoted as iPad displayed face. From

the data in Figure 4.10, it is apparent that all real faces and iPad displayed faces have been successfully identified accordingly. In this case, confusion matrix may not be necessary as each measure shows 100% accuracy rate as illustrated in the plots below.

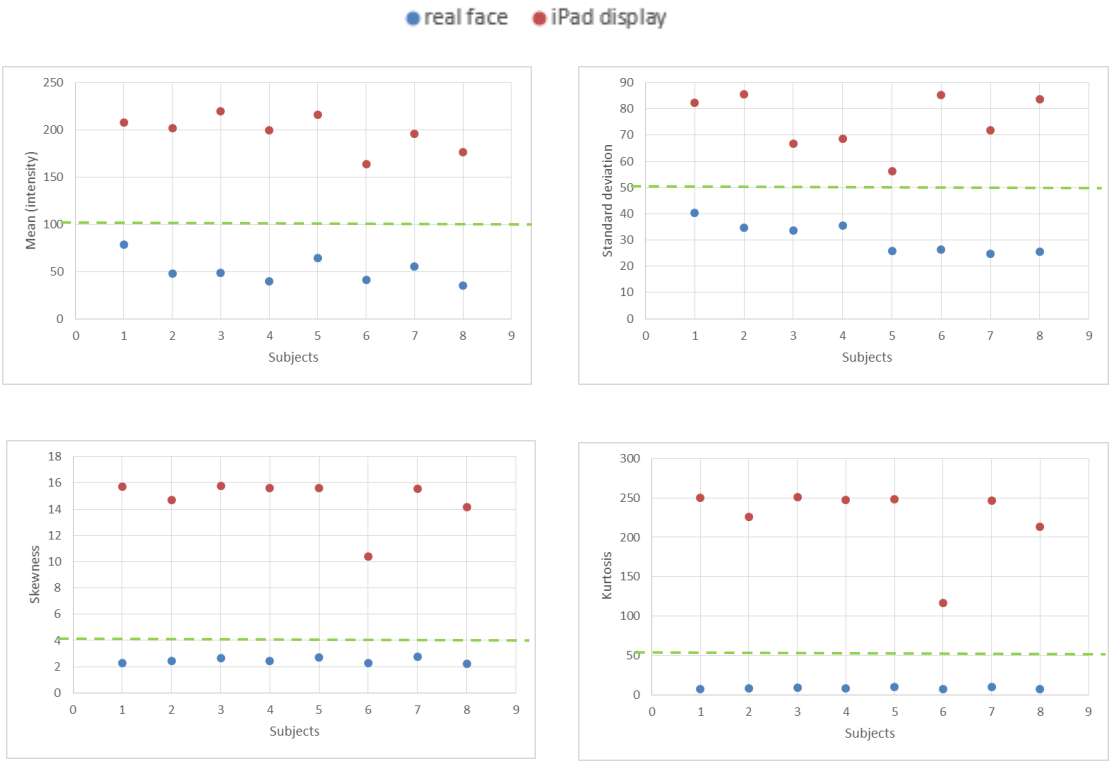

Figure 4.10: The statistical results of the I_{SDOLP} between real and iPad displayed faces

The statistical results obtained in this section have shown that I_{SDOLP} can be used to distinguish between genuine face and iPad attack. Thus, it is not necessary to carry on with further measures. In the following section, the same analysis on I_{DOP} and I_{SDOLP} images were repeated to detect printed photo attacks.

4.3 Spoofing Face Detection between Genuine Face and Printed Photo Paper

So far, this chapter has focussed on the techniques to differentiate between genuine faces and iPad attacks. The results show that the iPad attacks were distinguishable from the genuine faces using the two proposed parameters: the DOP and the SDOLP. Despite the iPad attacks, photograph representation is one of the most common spoofing attacks in face recognition system [Chakka et al. (2011)]. Photograph of a person can be easily obtained, for instance by downloading through the internet [Bagga and Singh (2016)]. Therefore, this section focuses on detecting photo spoofing face based on the same two parameters used in Section 4.2 which are the DOP and the SDOLP.

As reported in the literature review, vast majority of spoofing faces is photo face. Photo attacks are carried out by presenting photograph of a legitimate user to the recognition system as attempts to gain access. There are some reasons behind the selection of paper mask as the spoofing attacks. First, images of a legitimate user is easily available. For instance, photograph of a person can be easily downloaded from any well-known online social media websites. Second, the photos can be taken by the impostor using a digital camera or a video camera. The photos can be easily printed either to carry or to store. Other than that, the cost to produce a paper mask is cheap and affordable. Thus, it is not surprising that paper mask is a popular choice to be used in the spoofing attacks by the imposters.

Before proceeding to examine the polarized reflection of the two materials, it is necessary to discuss the physical properties of paper. Paper is usually made of cellulose fibres which are a complex carbohydrate consisting of more than 3,000 glucose units [Britannica (2007)]. Although papermaking processes have become highly mechanized compared to when paper was first produced in China, the basic steps remain unchanged. The fibres are firstly separated and wetted to yield the paper stock which is then filtered to form a sheet of fibre. The fibre sheet is pressed to squeeze out most of the water. The sheet is evaporated to remove the remaining water and produce a dry sheet. Depending on the intended use, the dry sheet is then coated or impregnated with other substances to generate the required paper.

There are four most important optical properties of paper: brightness, colour, opacity, and gloss [Britt (2012)]. For writing and printing purposes, opacity is the most desired paper property. Opaque paper requires white mineral pigments applied as coating. Apart from that, coated papers have five types of finishing which describe the characteristics of the paper surface. These are: the cast coated, gloss, dull, silk, and matte. In this study, the paper mask was printed on a matte paper; hence the following discussion is related to matte paper. According to Matt (2012), matte paper has no sheen on the surface which contributes to an extremely low reflection property. Most of the light that hits matte paper is absorbed, while only a little amount is reflected. The absorbed light is diffused by the paper before re-emerging from the paper to the air. The amount of the reflected light from the paper surface is also affected by the inks printed on the paper. In an investigation of penetration of light into paper printed with a black and white checkerboard pattern, Yule and Nielsen (1951), found that light which strikes on the black dots is absorbed while the remaining is diffused by the paper. Figure 4.11 illustrates the interaction between a paper print with checkerboard pattern with light. As shown in Figure 4.11, only 25% of the incident light is reflected from the paper. The estimated reflection amount is only applied for the checkerboard patterned paper.

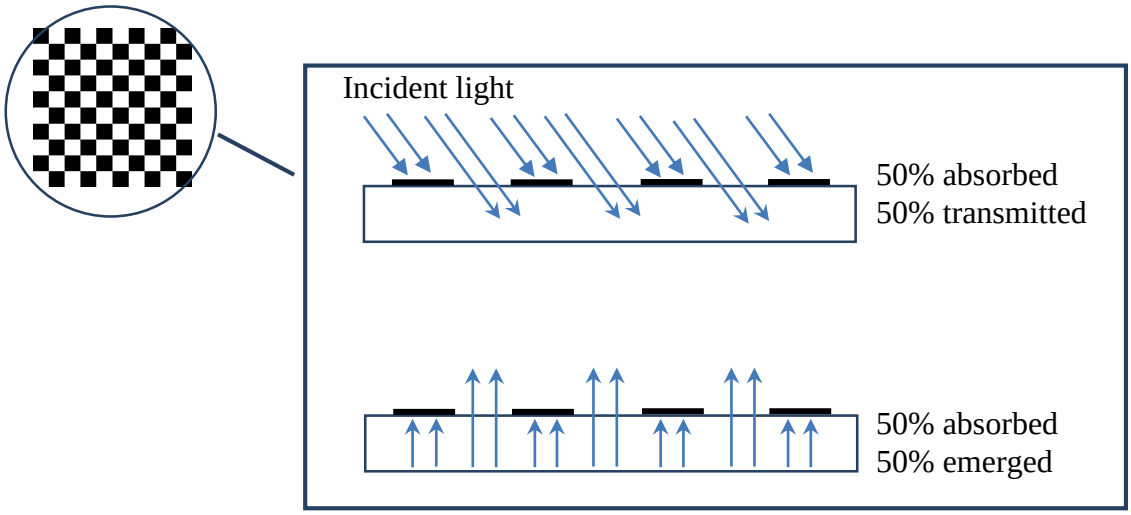

Figure 4.11: The interaction of light and a checkerboard patterned paper

There are other factors that influence the reflection from a matte paper printed with solid ink. These factors are the surface reflection, light scattering and reflection within the substrate, and the internal reflections at the paper-air interface [Hersch et al. (2005)]. As portrayed in Figure 4.12, Hébert and Hersch (2009) illustrated the reflection and transmission of light that hits the coloured printed paper interface. From the image shown in Figure 4.12, some of the incident light is reflected to the air, R_{sur}; while the remainder is transmitted through the inked-paper layer. The transmitted light is scattered within the inked-paper layer and diffusedly reflected to the air, R_{dif}. This phenomenon is similar to the interaction between incident light wave and skin layers as explained in Section 2.2. In general, it seems that human skin and coloured printed paper are having similar reflection properties. Both of the materials produce more than one reflections namely as surface and subsurface (diffuse) reflections. Due to the similarity, it is assumed that the analysis to differentiate between real face and printed photo face will experience a more intense challenge.

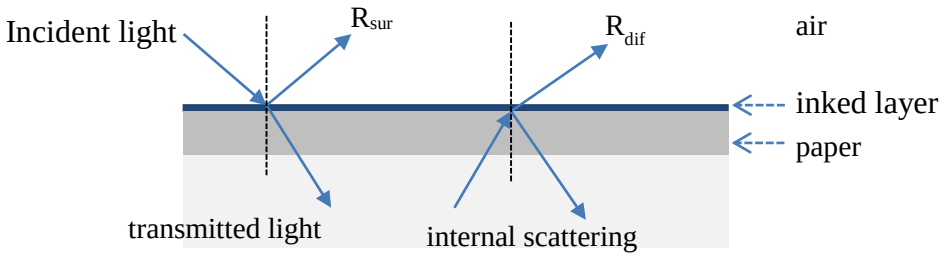

Figure 4.12: The interaction between incident light and coloured paper

4.3.1 Dataset

Since no polarised image dataset for real face and photo spoofing attacks is publicly available, once again the images used in this study were self-collected. The new dataset was named as Face-Photo-Spoof (FaPs) dataset. To enhance the accuracy of the results, the number of subjects in this Face-Photo-Spoof (FaPs) dataset were increased. Compared to only eight genuine subjects and eight iPad displayed faces in the Face-iPad dataset, the FaPs dataset consisted of 37 genuine faces which were randomly selected among the faculty members. These genuine faces were generally classified into three skin colours: 26 Asian; 4 Black; and

7 Caucasian. Meanwhile, printed photos of each genuine subject were added to the FaPs dataset. The same experimental setup and image recording processes as explained in Section 4.2.1 and Section 4.2.2, respectively, were repeated in collecting polarised images for the FaPs dataset. In contrast, printed photo papers were used as spoofing attempts in this study. Images of each genuine subject were printed on a matte A4 white paper which were then placed in front of the camera lens as fake faces. Figure 4.13 presents the structure of FaPs dataset. As can be seen from Figure 4.13, the final processed polarised images for genuine faces were labelled as F_0, F_{45}, F_{90} and F_{135} in accordance with the polarisation angles. Similarly, the processed polarised printed photo faces were named as PF_0, PF_{45}, PF_{90} and PF_{135}.

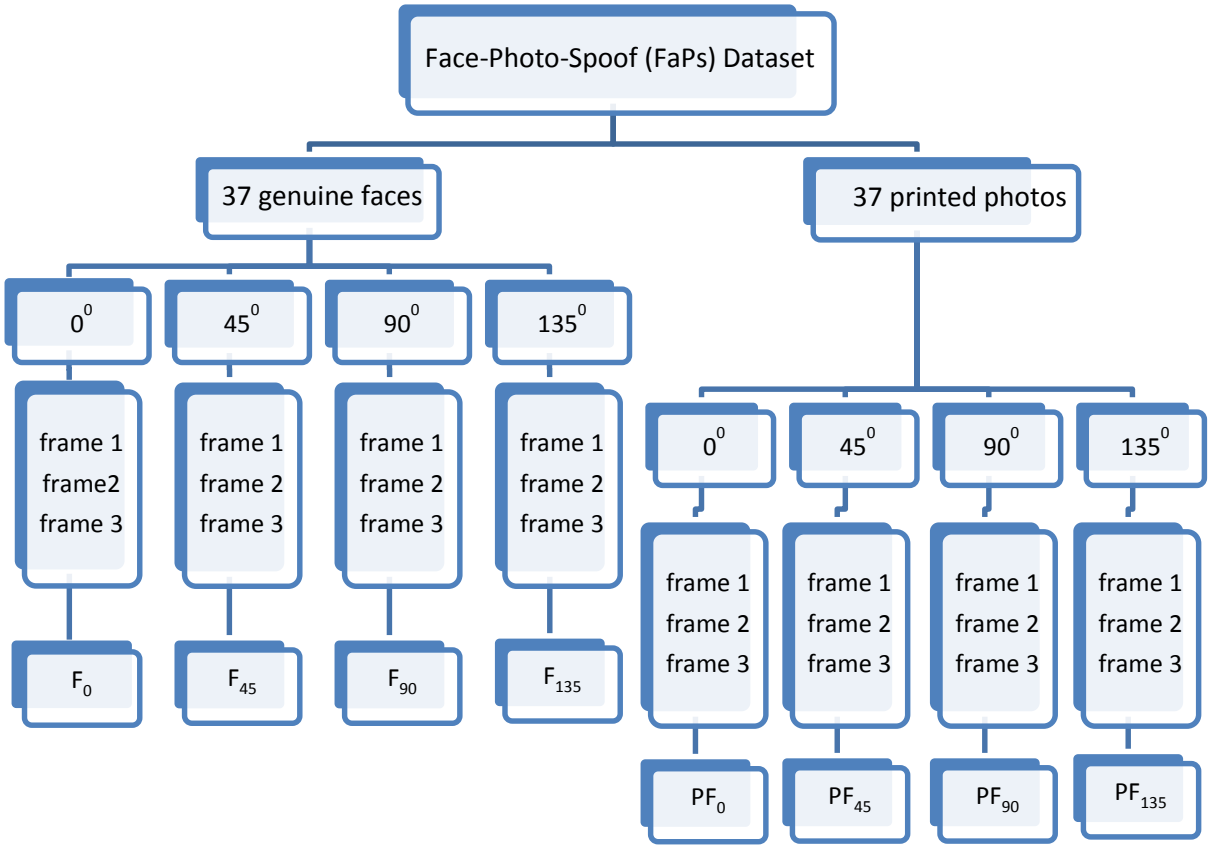

Figure 4.13: The structured Face-Photo-Spoof (FaPs) dataset

The number of images available in the FaPs dataset can be elaborated as follows. Firstly, 37 genuine faces and 37 printer photo paper were captured under four polarisation angles: 0^0, 45^0, 90^0 and 135^0; three frames of images at each polarisation angle for each subject. These polarised images then went through image registration and image averaging processes. After these processes, one final processed polarised image was generated under each polarisation angle for each real and fake traits. In total, 1184 polarised images are available in the FaPs dataset. For analysis comparison purposes, one RGB polarised image of each skin colour for both real and fake faces is presented in Figure 4.14.

Images in Figure 4.14 are quite revealing in several ways. Firstly, the printed photo faces seemed more blurry and darker than the genuine faces. Secondly, glare can be seen on the printed photo face particularly at the 0^0 polarisation angle. However, the glare was eliminated at the perpendicular polarisation axis which is at 90^0 polarisation angle. Images from Figure 4.14 had gone through image registration and averaging processes. On the needs of these two processes, the input RGB polarised images were converted to grayscale images and the results are shown in Figure 4.15. Contrary to grayscale images between genuine face and iPad displayed faces in Figure 4.3, the appearance of grayscale images between genuine and printed photo faces in Figure 4.15 are quite similar. Apart from some glare on the printed photo faces, no other obvious distinction was found. Further investigations were carried out based on the same parameters: the DOP and the Stoke parameters. Next section discusses on the DOP parameter as trial to differentiate between the real and fake faces.

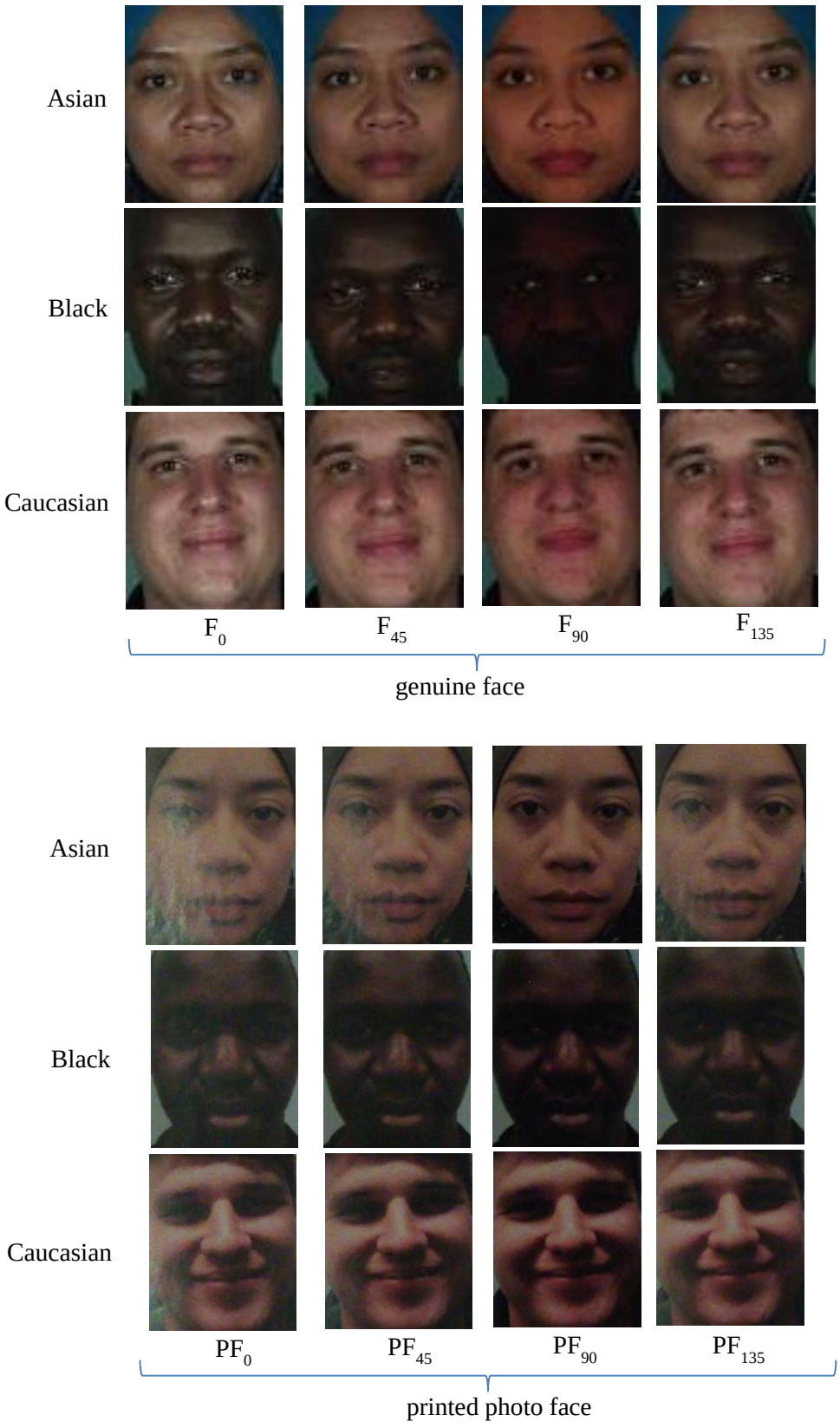

Figure 4.14: RGB polarised images for different skin colours of genuine face and printed photo face

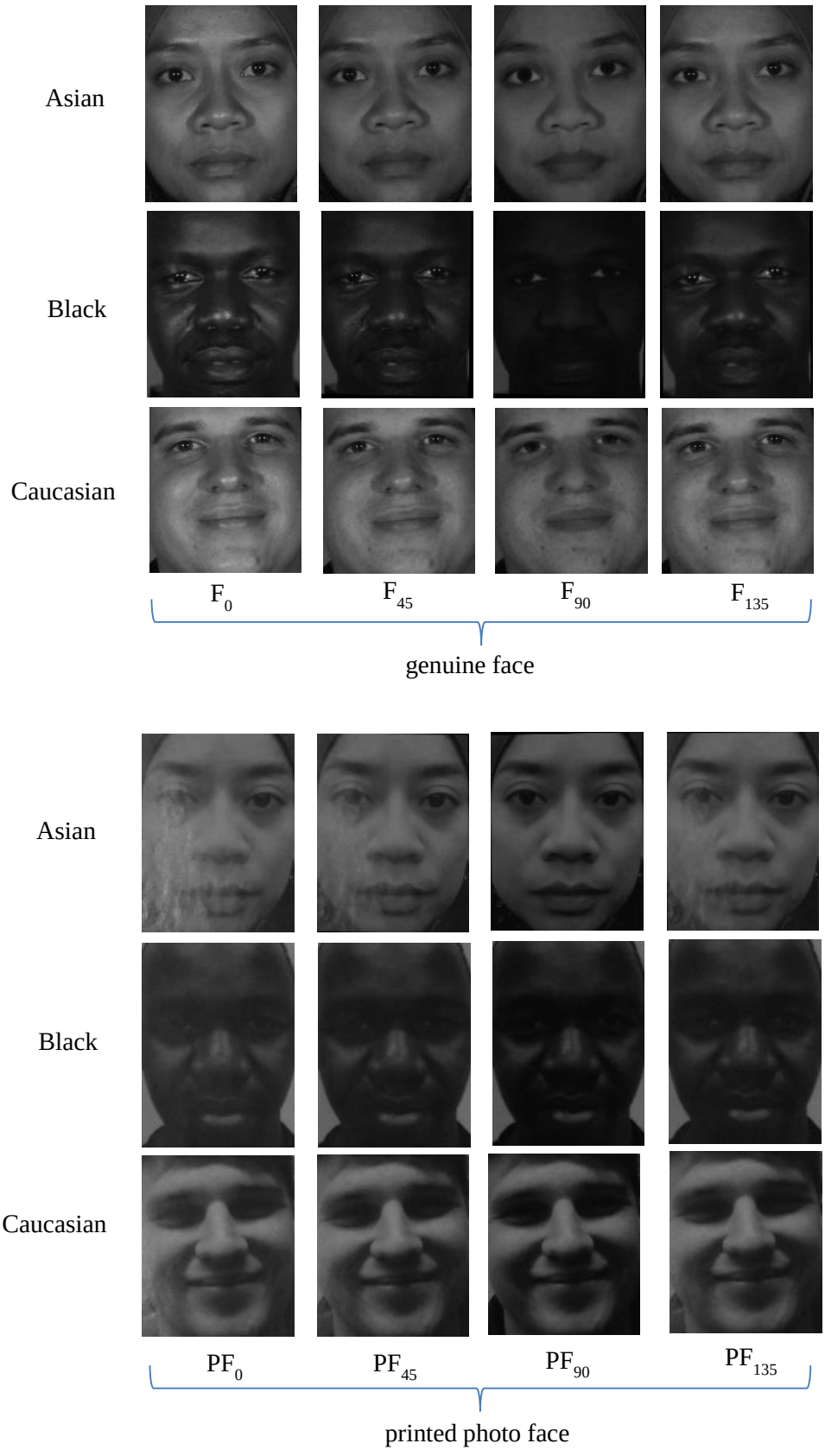

Figure 4.15: Examples of processed images for different skin colours of genuine face and printed photo face

4.3.2 The degree of polarisation

The degree of polarisation (DOP) was used to measure partially polarised light reflected from the material surface. In this study, the DOP values were analysed based on the polarisation image, I_{pol} of each real and printed photo faces in FaPs dataset. By using equation (3.6), I_{pol} was generated for each real and fake faces in the dataset. Figure 4.16 compares the S_0 and S_1 image components and the I_{pol} images between the real and printed photo face among the three different skin colours. To avoid confusion, polarisation images for the real face and the printed photo are called F_{pol} and PF_{pol}, respectively. From the F_{pol} and PF_{pol} in Figure 4.16, no significant difference in terms of image intensity was found. Similar to the analysis that have been carried out in previous experiments in this thesis, the F_{pol} and PF_{pol} were initially being examined statistically. Results for the statistics analysis on F_{pol} and PF_{pol} are presented in Figure 4.17.

From the data in Figure 4.17, it is observed that there is a clear different score patterns between real faces and printed photo faces. On average, the mean intensity values for the real faces are very small within the range values of 0 and 0.01; the mean intensity of Fpol images are lower compared to the mean intensity values for PF_{pol}. The similar scores pattern can also be seen in Figure 4.17 for the standard deviation values between the real and fake faces. Meanwhile, the skewness and kurtosis values for the genuine faces are higher than the printed photo faces. Based on these differences, a threshold is set for each measure as represented by the dotted green line in Figure 4.17. By using confusion matrix in Table 4.1, each subject is classified as real face or printed photo face based on the predetermined threshold shown in Figure 4.17. For instance, a subject is determined as real face if the mean or standard deviation value is less than the corresponding threshold. In addition, the skewness or kurtosis scores for real face should be more than the threshold. Otherwise, the subject is known as printed paper photo. The predictions' results for all F_{pol} and PF_{pol} images in the FaPs dataset are summarised in Figure 4.18.

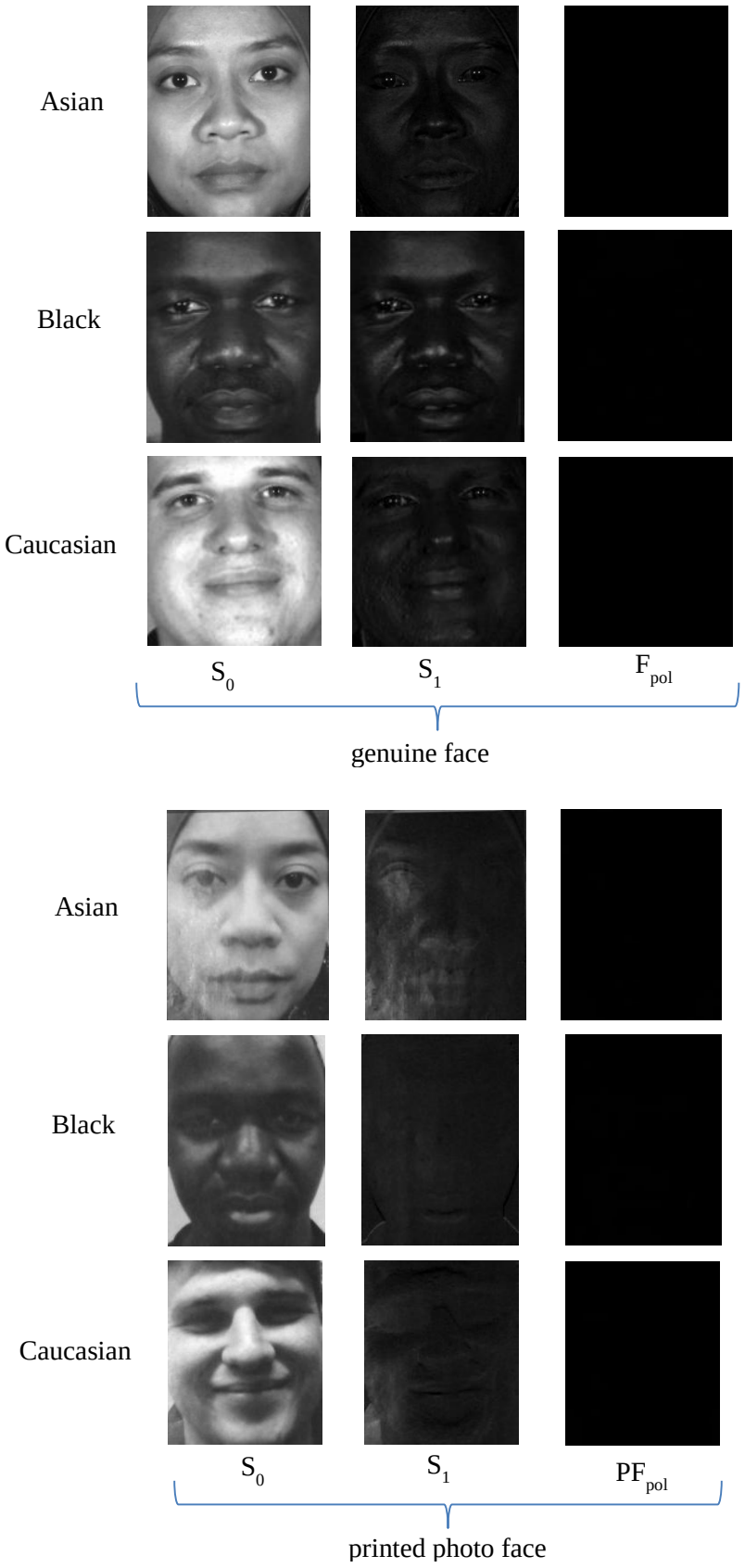

Figure 4.16: The S_0 and S_1 image components and I_{pol} images

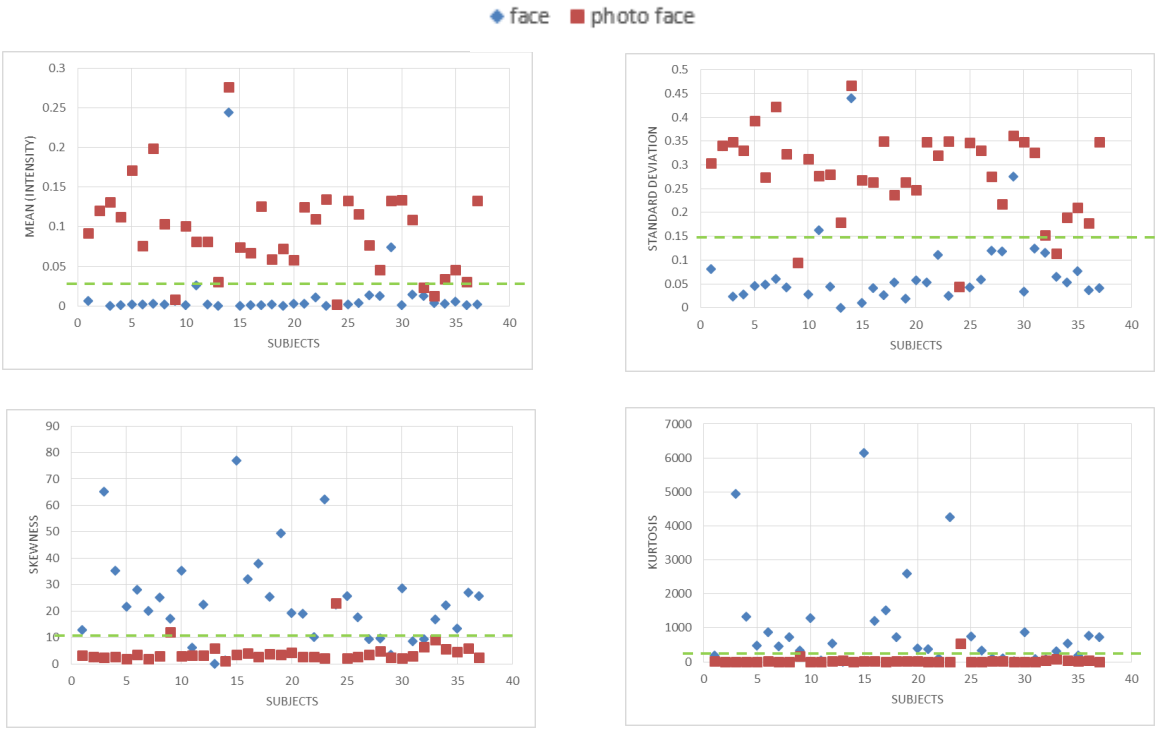

Figure 4.17: The statistics analysis for F_{pol} and PF_{pol}

From the scores in Figure 4.18, the TPR and FPR were calculated using equation (4.1). Then, the accuracy (AC) rates for the mean, standard deviation, skewness and kurtosis were determined using equation (4.2). Table 4.3 provides the results obtained for the TPR, FPR and AC. From the results in Table 4.3, the accuracy detection rates for the mean, standard deviation and skewness are over 90%. The kurtosis accuracy rate is slightly lower. Although the F_{pol} and PF_{pol} seem similar to each other as shown in Figure 4.16, there is a small amount of intensity which represents the portion of reflected light from these two material surfaces that were polarised. Since the intensity values for both F_{pol} and PF_{pol} are very low, no histogram can be generated for further analysis.

n = 74	Predicted: Real face	Predicted: Printed photo	
Actual: Real face	34	3	37
Actual: Printed photo	4	33	37
	38	36	

(a) mean

n = 74	Predicted: Real face	Predicted: Printed photo	
Actual: Real face	34	3	37
Actual: Printed photo	3	34	37
	37	37	

(b) standard deviation

n = 74	Predicted: Real face	Predicted: Printed photo	
Actual: Real face	32	5	37
Actual: Printed photo	2	35	37
	34	40	

(c) skewness

n = 74	Predicted: Real face	Predicted: Printed photo	
Actual: Real face	30	7	37
Actual: Printed photo	1	36	37
	31	43	

(d) kurtosis

Figure 4.18: The predictions scores for F_{pol} and PF_{pol} based on the statistics measures

The detection accuracy rates in Table 4.3, which are based on the statistical analysis, show convincing classification rates in which almost all of the four measures achieved more than 90%. Since no data distribution for each I_{DOP} of genuine face and printed photo, further analysis could not be carried out.

Table 4.3: Detection rates of the statistical measures for F_{pol} and PF_{pol}

	TPR	FPR	Accuracy (AC)
	in percentage (%)		
Mean	91.89	10.81	90.54
Standard deviation	91.89	8.10	91.78
Skewness	86.49	5.41	90.54
Kurtosis	81.08	2.70	89.19

As discussed earlier in Section 4.2.3, physical property of a material is one of the reasons that contributes to the results of the degree of polarisation. Human skin is classified as non-conductor. Meanwhile, printed photo paper is also an insulator. Another similarity between the genuine face and paper photo is that both of the materials produce two types of reflections: specular and diffuse. Despite these similarities, statistically, by using the DOP, the fake faces have been able to be distinguished from the real faces. In the next section, the Stokes parameters were applied as further investigations in detecting printed photo attacks.

4.3.3 The Stokes parameters

This section describes and discusses the Stokes parameters used to distinguish between real faces and printed photo faces. Polarised images in Face-Paper-Spoof (FaPs) dataset were used for analysis throughout this section. Firstly, by using equation (3.2), three components of the Stokes parameters known as S_0, S_1 and S_2, were generated. These components, in the forms of images are presented in Figure 4.19. As can be seen in Figure 4.19, there are several clear differences of the Stokes components between the real and fake faces. For instance, S_1 and S_2 components for real faces contain significant features compared to the same components of the printed photo faces. Apart from that, glare can be detected on most of the printed photo faces' components. After obtaining the S_0, S_1 and S_2 components, an image named as I_{SDOLP} was obtained by using equation (3.3). Figure 4.20 presents the I_{SDOLP} images of the real and fake faces.

The I_{SDOLP} images in Figure 4.20 are quite revealing in several ways. Firstly, the intensity of black genuine face is brighter than the Asian and Caucasian genuine skin colours. Secondly, unlike the genuine faces, there are some bright parts on the I_{SDOLP} of the printed photo faces particularly on the eyes and mouth regions. Although it is apparent from Figure 4.20 that the I_{SDOLP} of genuine faces are different that the printed photo faces, it is necessary to measure the differences by the proposed parameters in order to differentiate between the real and fake traits. In Section 4.2.3, the DOP parameter was statistically able to distinguish between printed photo faces than the real faces even though the F_{pol} and PF_{pol} are dark and very similar to each other. In this section, before proceeding with the statistics analysis, histograms of each I_{SDOLP} image was plotted to represent the data distribution of the images. The histograms are shown underneath each of the I_{SDOLP} in Figure 4.20.

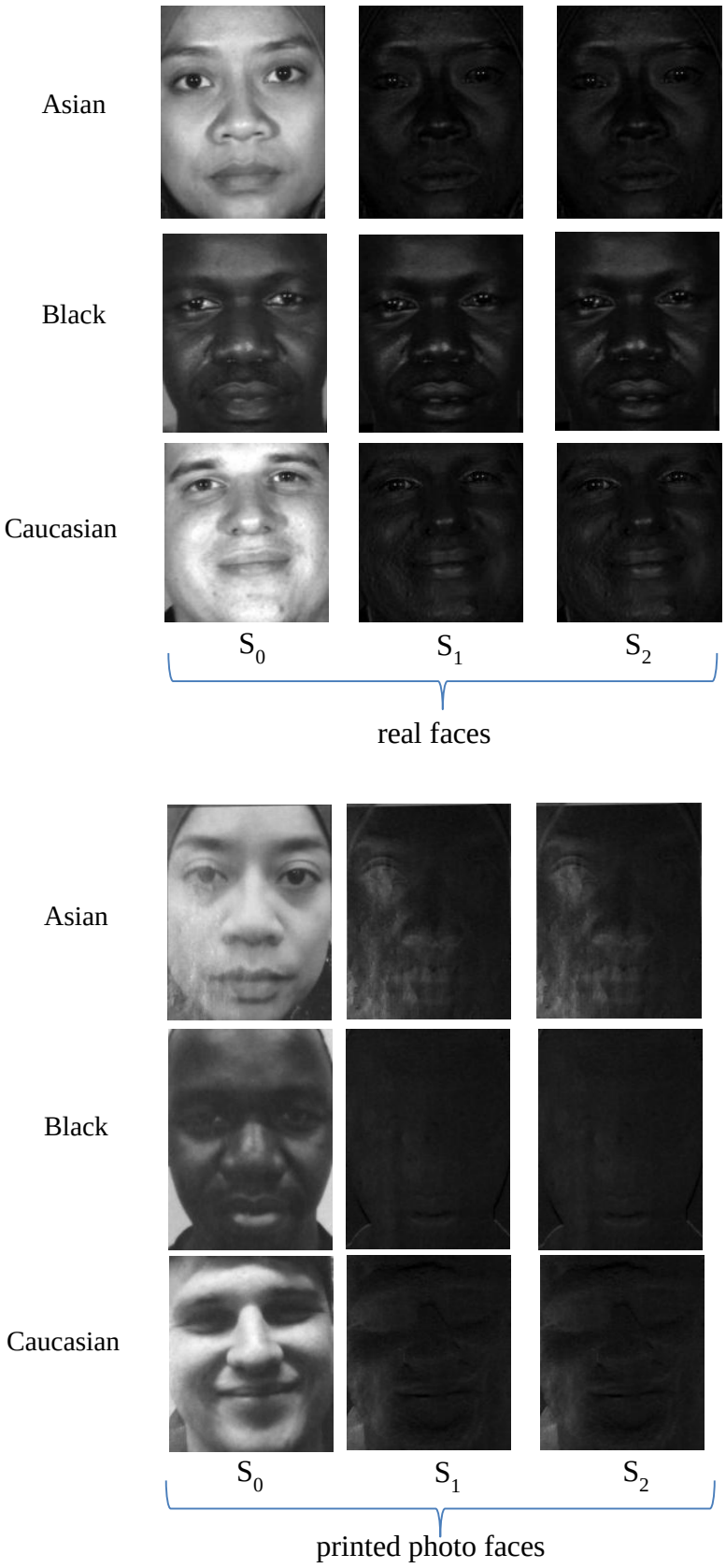

Figure 4.19: The Stokes components, S_0, S_1 and S_2 for real faces and printed photo faces of different skin colours

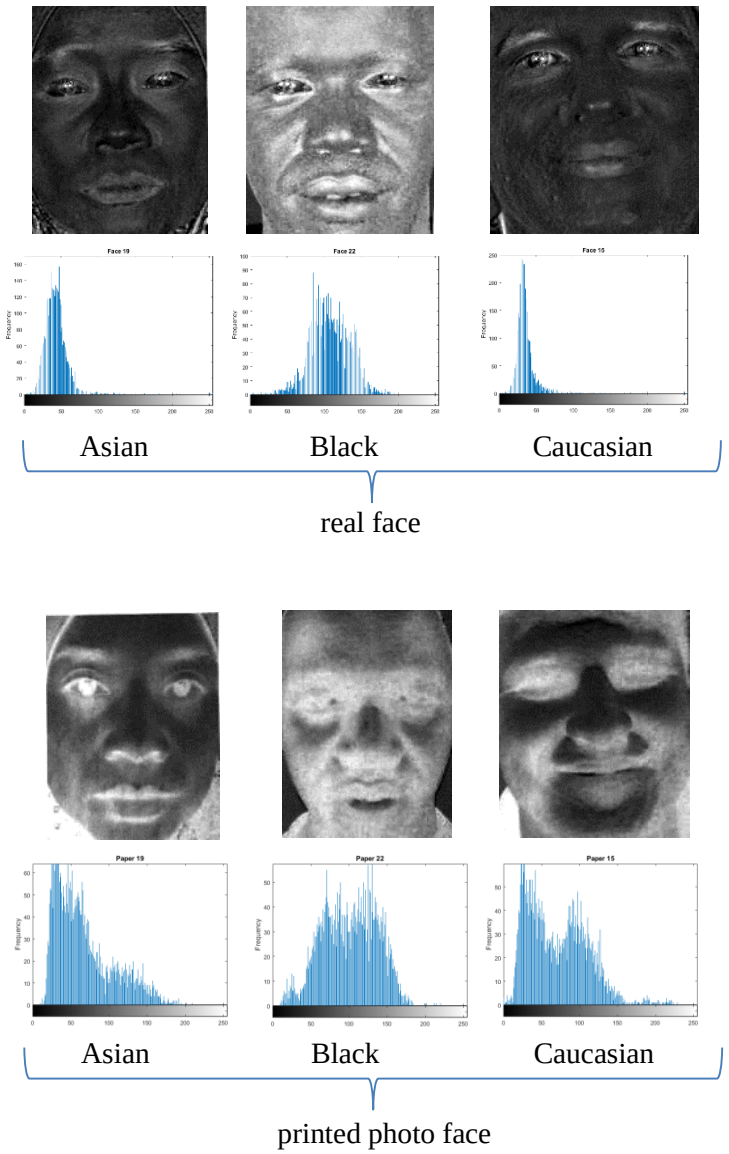

Figure 4.20: The I_{SDOLP} for the real faces and printed photo faces

a) Statistical analysis

From the histograms in Figure 4.20, it is seen that data distribution for the three printed photo faces are wider than the real faces. Surprisingly, histogram of the black genuine face shows relatively similar distribution to the black printed face. The shape of histograms for the black genuine face and the three printed photo faces are more likely multimodal shape. On the other hand, histograms of Asian and Caucasian real faces are likely to have unimodal data distribution. The assessment was based on rough views. Nonetheless, to verify the similarities

and differences between I_{SDOLP} of real faces and photo faces, comparison by statistical analysis was conducted. The four statistical measures: mean, standard deviation, skewness and kurtosis were calculated using equations (3.9) - (3.11), respectively. Scores for each statistic measure is presented in the form of scatter chart as shown in Figure 4.21.

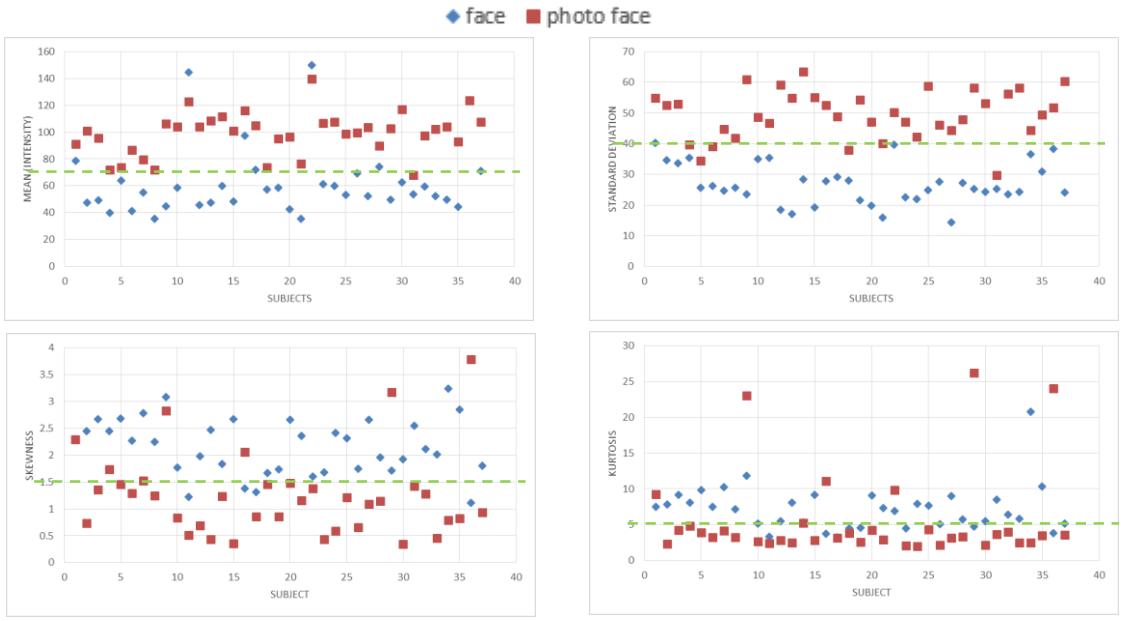

Figure 4.21: Statistics analysis on the I_{SDOLP} of real faces and printed photo faces

It can be seen from the chart in Figure 4.21 that the statistics scores between real faces and photo faces reported a convincing separation pattern. A threshold was selected for each measure as represented by the dotted green line in Figure 4.21. The I_{SDOLP} image is identified as real face if the mean or standard deviation score is lesser than the corresponding threshold. Otherwise, the I_{SDOLP} images is detected as spoofing face. While score of the skewness or kurtosis that is more than the threshold belongs to real face, any of these two scores that is less than the threshold is considered as fake face. These predictions were carried out based on confusion matrix in Table 4.1 for all I_{SDOLP} images in FaPs dataset. The predictions' results are shown in Figure 4.22.

n = 74	Predicted: Real face	Predicted: Printed photo	
Actual: Real face	29	8	37
Actual: Printed photo	1	36	37
	30	44	

(a) mean

n = 74	Predicted: Real face	Predicted: Printed photo	
Actual: Real face	36	1	37
Actual: Printed photo	5	32	37
	41	33	

(b) standard deviation

n = 74	Predicted: Real face	Predicted: Printed photo	
Actual: Real face	33	4	37
Actual: Printed photo	6	31	37
	39	35	

(c) skewness

n = 74	Predicted: Real face	Predicted: Printed photo	
Actual: Real face	21	16	37
Actual: Printed photo	6	31	37
	27	47	

(d) kurtosis

Figure 4.22: The predictions scores for I_{SDOLP} based on the statistics measures

Based on the predictions' results in Figure 4.22, detection rates were then measured by using equation (4.1). Following this, the accuracy (AC) rates for the mean, standard deviation, skewness and kurtosis were determined using equation (4.2). The results for the TPR, FPR and AC are presented in Table 4.4. From the data in Table 4.4, the standard deviation shows highest detection accuracy rate compared to the other three statistics moments. Despite the highest accuracy rate of the standard deviation, the score alone is not sufficient to be used in detecting spoofing faces. As Table 4.4 shows, it is not easy to find a general rule to distinguish genuine and paper faces.

Table 4.4: Detection rates of the statistical measures for I_{SDOLP}

	TPR	FPR	Accuracy (AC)
	in percentage (%)		
Mean	78.38	2.70	87.84
Standard deviation	97.30	13.51	91.89
Skewness	89.19	16.22	86.49
Kurtosis	56.76	16.22	70.27

In Figure 4.20, there is a clear difference of histogram shape between genuine and fake faces except for the black genuine face. The histogram comparison shown in Figure 4.20 was between three genuine faces and three printed photo faces. Since there are 37 real faces and 37 printed photo faces in the FaPs dataset, histograms of all I_{SDOLP} are visualised in Figure 4.23 and in Figure 4.24. In Figure 4.23, mostly all of the distribution for genuine faces show small deviation. In addition, the modality of the histograms seemed more likely to unimodal distribution except from three of them. For instance, the deviation of data for F_{11}, F_{22} and F_{36} as illustrated in Figure 4.23 are wider compared to the others. Interestingly, these three distributions represent black genuine faces. Turning now to the histograms for the printed photo faces in Figure 4.24. The histograms show that the data deviation is wide. On average, the modality of the distribution is assumed to be bimodal distribution.

Statistically, data distribution for I_{SDOLP} of both genuine and photo faces were analysed and the results are shown in Table 4.4. Due to the convincing differences of data distribution between real faces and printed photo faces as in Figure 4.23 and Figure 4.24, further analysis on the distribution's modality is carried out in the next section.

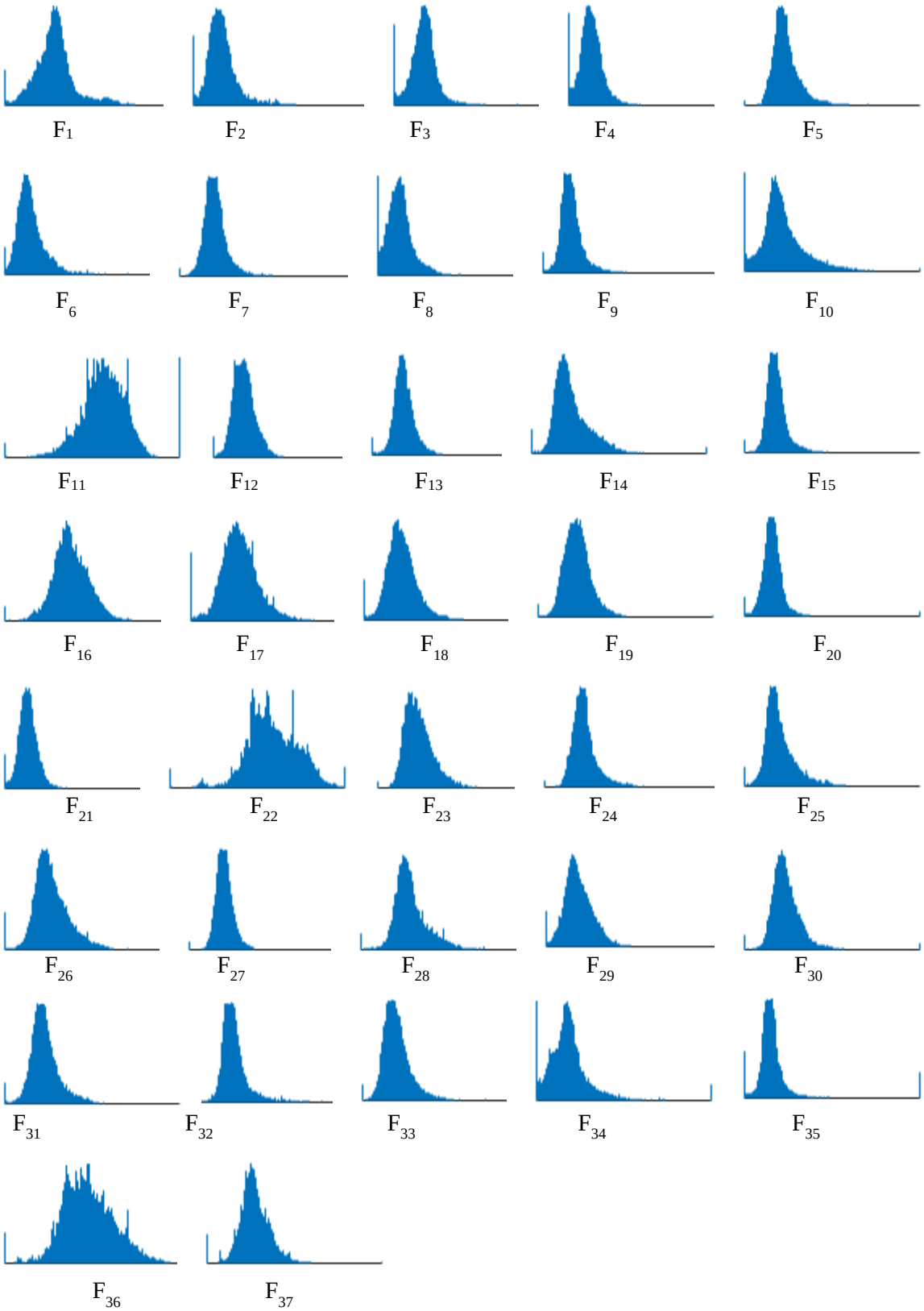

Figure 4.23: Histograms of I_{SDOLP} for genuine face in FaPs dataset

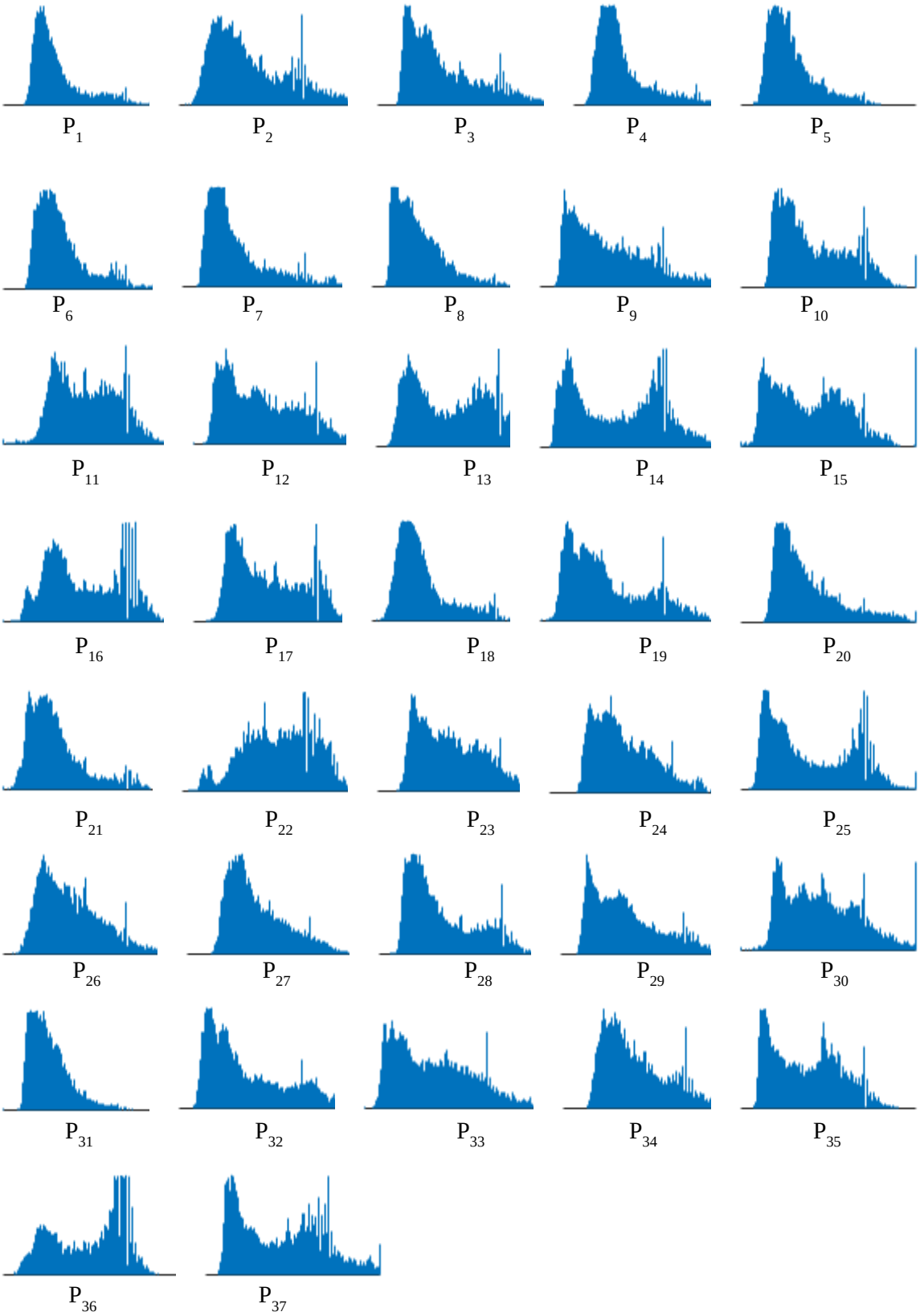

Figure 4.24: Histograms of I_{SDOLP} for printed photo face in FaPs dataset

b) Modality of distribution

Besides the statistical analysis, the difference of the histogram shape between real and printed photo faces should indicate another classification cue. Driven by the histograms in Figure 4.23 and Figure 4.24, data distribution for real faces and printed photo faces are assumed as unimodal and bimodal, respectively. These assumptions need to be proven by using appropriate parameter. Previous researchers have used several measures to differentiate between unimodality and bimodality. For instance, the Bimodality coefficient (BC) [Pfister et al. (2013)], the Hartigan's dip statistic (HDS) [Hartigan and Hartigan (1985)] and the Akaike's information criterion (AIC) [Akaike (2011)].

Freeman and Dale (2013) carried out experiments to compare between the BC and the HDS. The results showed that both measures had advantage for assessing bimodality, however, neither measure was sensitive and specific at the same time. Different results were obtained when using different set of data. In the first experiment, Freeman and Dale (2013) used simulated data which were controlled and varied. The results concluded that the HDS was the robust measure for detecting bimodality compared to the BC and the AIC. Then, Freeman and Dale (2013) measured the performance of the BC and the HDS by using experimental data contained in the study by Freeman et al. (2008). The results demonstrated that the BC and the HDS were able to differentiate between unimodal and bimodal distributions. In both experiments by Freeman and Dale (2013), the AIC measure was found to be more liberal by recognizing bimodality in all distributions. Although Freeman and Dale (2013) favoured the HDS than the BC, they also considered the use of the BC according to the types of data.

Driven by these findings, the BC and HDS was chosen to determine the distribution modality of real and printed photo faces' I_{SDOLP} images. The performance of the BC and the HDS measures were robust for detecting bimodality in experimental data in which the modality of the distribution was theoretically known [Freeman et al. (2008)]. The computation of the BC requires three inputs: the sample size; the skewness; and the kurtosis. The formulation of the BC was computed using MATLAB based on the sample-bias corrected equation proposed by Pfister et al. (2013) as:

$$BC = \frac{m_3^2 + 1}{m_4 + 3\left(\frac{(n-1)^2}{(n-2)(n-3)}\right)} \tag{4.3}$$

where m_3 = skewness (x,0); m_4= kurtosis (x,0) – 3; and *n* = sample size. The BC values range from 0 and 1, with empirical values of BC > 0.555 suggesting bimodal distribution [SAS Institute, (1989)]. Otherwise, the distribution is classified as unimodal. In this study, genuine face was assumed to have unimodal distribution while printed photo face has bimodal distribution. These assumptions were based on the histograms shown in Figure 4.23 and Figure 4.24. Based on the BC algorithm, distribution of the I_{SDOLP} in the FaPs dataset was identified as genu`ine face if the BC score is less than 0.555. Meanwhile, I_{SDOLP} distribution with the BC score more than 0.555 is classified as printed photo face.

The HDS is a dip test that measures multimodality in a sample by the maximum difference, over all sample points, between two functions: (1) the empirical distribution function; and (2) the unimodal distribution function that minimizes the maximum difference [Hartigan and Hartigan (1985)]. The HDS algorithm was proposed by Hartigan and Hartigan (1985). This algorithm has then been corrected and the up-to-date version was published as an R diptest-package by Maechler (2015). The distribution with the HDS p-value < 0.5 is considered to be multimodal distribution. As mentioned above, genuine and printed photo faces are assumed to have unimodal and multimodal distributions, respectively. Therefore, p-value with more than 0.555 is indicated as real face whereas printed photo face with p-value less than 0.555. By using equation (4.3) and the publicly available R diptest-package, modality of each I_{SDOLP} was measured and compare between the BC and the HDS. Then, the detection rates were calculated: the true positive rate (TPR) and the false positive rate (FPR) by using equation (4.1); and the accuracy rate (AC) by using equation (4.2). Table 4.5 compares the detection rates between the BC and the HDS algorithms for I_{SDOLP} distributions.

From the data in Table 4.5, it is apparent that the BC is more accurate compared to the HDS. Although the TPR for the HDS is slightly higher than the TPR for the BC, the HDS has erroneously identified 80% of the total printed photo faces as genuine faces. Meanwhile, the BC has mistakenly identified: nine I_{SDOLP} of printed photo faces as real face; and four I_{SDOLP} of genuine faces as fake faces. The most striking aspect to emerge from these results is that all genuine faces that have been wrongly identified as multimodal distribution belonging to Asian and Caucasian skin colours. While the statistical analysis results in Table 4.4 show that distribution of genuine black faces are similar with the printed photo faces, the same black skin subjects were successfully identified as genuine faces by using the BC algorithm. These

findings suggest that the BC could be applied as an additional parameter to distinguish the black skin genuine subjects from the printed photo faces.

Table 4.5: Detection rates of the BC and the HDS for I_{SDOLP}

	TPR	FPR	Accuracy (AC)
	in percentage (%)		
The BC	89.19	22.32	82.43
The HDS	90.41	80.13	50.30

c) The density of distribution's mode

This section has focussed on statistical measures and distribution modality as trials to differentiate between genuine and printed photo faces. Some of the statistical results and the BC showed convincing detection results. To further examine the distributions between the two materials, the probability density function (PDF) might contribute to spoofing face detection. The PDF is also known as a density curve fitting, *f(x)* on a histogram which can be used to find the density value of a random distribution, *x*. The *f(x)* is positive value between 0 and 1. Figure 4.25 presents a sample of PDF curve for a normal distribution that has a single peak, or mode. Mode is a number that appears most often in a set of data. The graph in Figure 4.25 shows the peak of the distribution *x* is at number 0 with density value *f(x)* is 0.4.

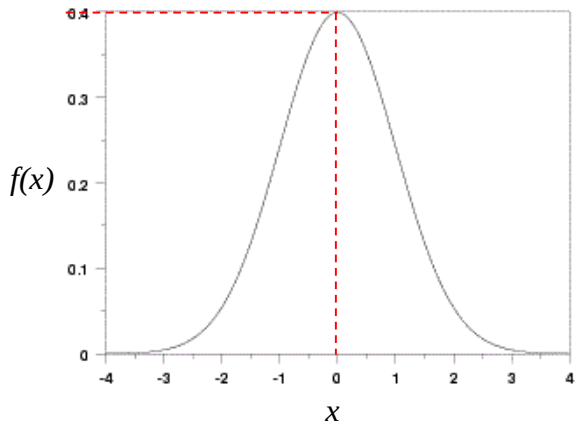

Figure 4.25: The PDF plot for a normal distribution

Motivated by the significant histograms shapes between genuine and printed photo faces presented in Figure 4.23 and Figure 4.24, the density value of each I_{SDOLP} distribution may also provide different scores between the real and fake faces. Therefore, the PDF of each I_{SDOLP} distribution in FaPs dataset was plotted and presented in Figure 4.26 and Figure 4.27. In both Figure 4.26 and Figure 4.27, some of the distributions have a single peak (mode) and the others have more than one peaks (modes). For multimodal distributions, the density value *f(x)* of each distribution was obtained from the highest peak shown in the plot. The comparison of the density values *f(x)* between genuine and printed photo faces is provided in Figure 4.28. From the plot in Figure 4.28, it is apparent that there is a clear classification pattern between the real and fake faces. The density values for real faces are higher compared to the printed photo faces. A threshold value, 0.02 is represented by the dotted red line. A distribution is classified as genuine face if the density value of the mode is more than the threshold. Otherwise, the distribution is identified as printed photo face. Similar to the statistical analysis and modality of distributions, the TPR and the FPR were measured by using equation (4.1) and the accuracy rate is calculated using equation (4.2). The results show that the TPR and the FPR for the density of the distribution mode are 94.6% and 13.5%, respectively; the accuracy rate is 90.5%.

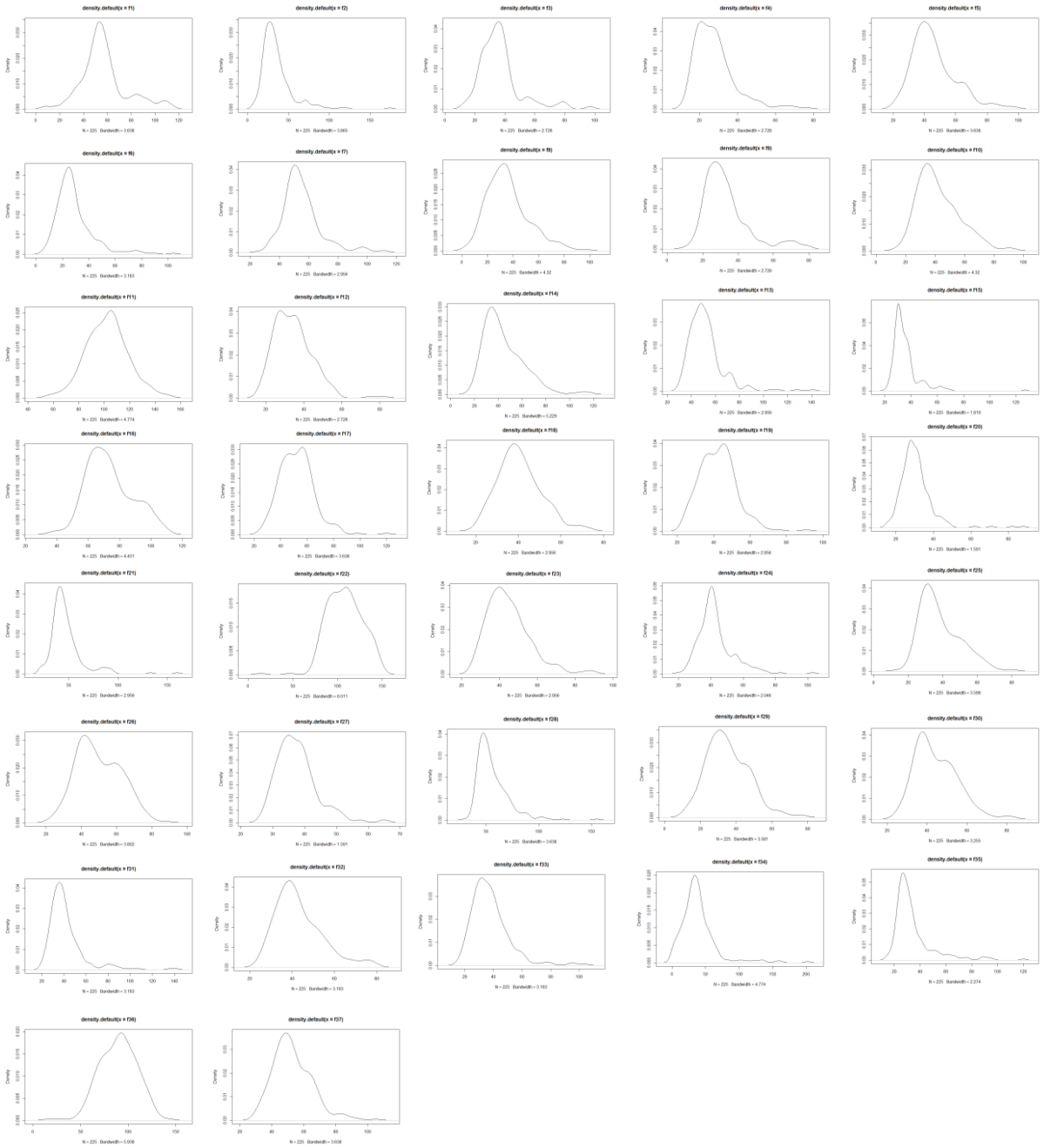

Figure 4.26: The probability density function (PDF) for the I_{SDOLP} of genuine faces

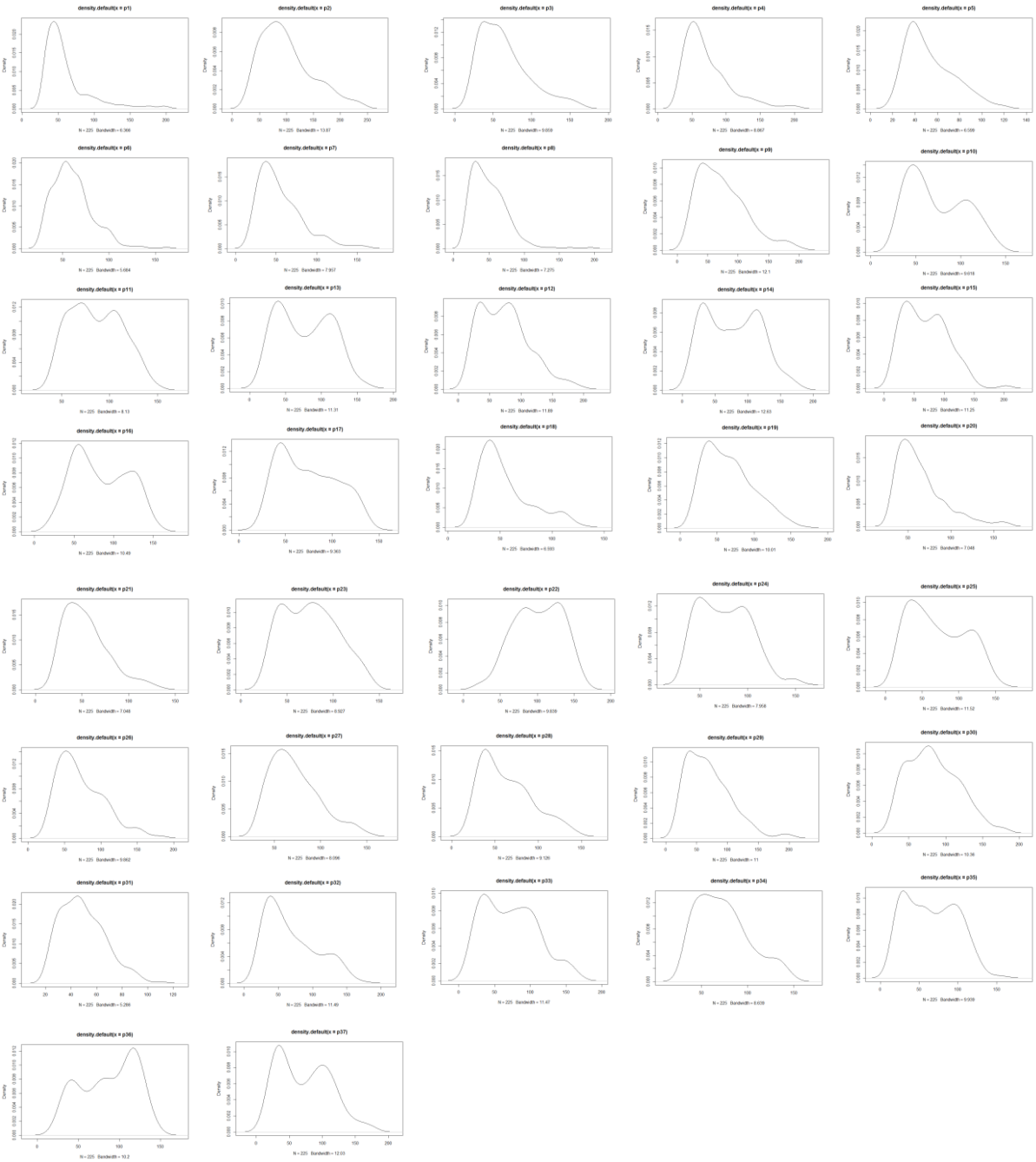

Figure 4.27: The probability density function (PDF) for I_{SDOLP} of printed photo faces

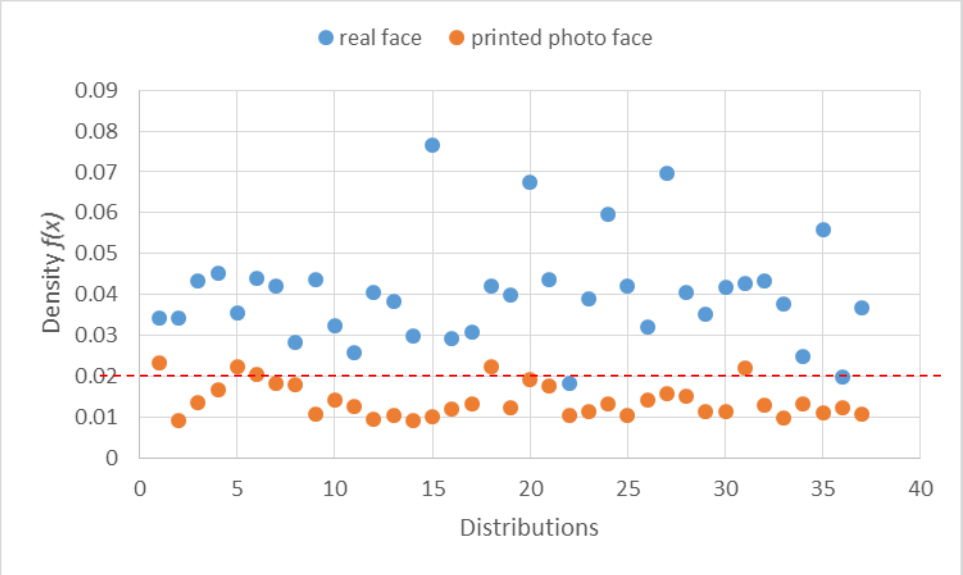

Figure 4.28: The density values, *f(x)* for I_{SDOLP} distributions

After obtaining the detection rates for statistical measures, the bimodality coefficient and the density of the distribution mode, the results explained that the I_{SDOLP}'s distributions between real face and printed photo paper were significantly different. However, the accuracy of spoofing face detection based on a single measure might be doubtful. Therefore, fusion based face detection algorithm is proposed in this thesis in which the details is discussed in the next section.

d) The SDOLP fast fusion formula (SDOLP3F)

In Section 4.3.3, the Stokes parameters were used to examine the state of polarisation between real faces and printed photo faces. An image named as I_{SDOLP} was obtained by using equation (3.3) for each real and fake faces in the FaPs dataset. The I_{SDOLP} was then analysed by four statistical measures, the bimodality coefficient and the density of distribution mode in order to find disparity values between genuine and printed photo faces. Table 4.6 summarises the detection rates obtained. From the results presented in Table 4.6, the most accurate measures with more than 90% accuracy rates are the standard deviation and the density of mode. In addition, the TPR for both measures are also the highest compared to the others.

Table 4.6: The detection rates between the statistics moments, the BC and the density of distribution mode of the I_{SDOLP}

	TPR	FPR	Accuracy (AC)
	in percentage (%)		
Mean	78.38	2.70	87.84
Standard deviation	97.30	13.51	91.89
Skewness	89.19	16.22	86.49
Kurtosis	56.76	16.22	70.27
The BC	89.19	22.32	82.43
Density of mode	94.6	13.5	90.5

To further investigate if higher detection accuracy rate can be obtained by fusing some of the most accurate measures, a list of algorithm components, α was proposed:

$$\begin{aligned} \alpha_{mn} &= mn - th_{mn} \\ \alpha_{sd} &= sd - th_{sd} \\ \alpha_{sk} &= th_{sk} - sk \\ \alpha_{kt} &= th_{kt} - kt \\ \alpha_{bc} &= th_{bc} - bc \\ \alpha_{mod} &= th_{mod} - mod \end{aligned} \tag{4.4}$$

where α is the algorithm component; *mn* is the mean; *sd* is the standard deviation; *sk* is the skewness; *kt* is the kurtosis; *bc* is the bimodality coefficient; *mod* is the density of distribution mode; and *th* is the corresponding threshold for each measure.

From the detection accuracy rates in Table 4.6, it is apparent that there are only two measures with the highest accuracy rates more than 90%: the standard deviation and the density of distribution mode. These measures were then selected to be fused in the newly proposed fusion formula names as the SDOLP fast fusion formula (SDOLP3F):

$$SDOLP3F = \alpha_1 + \alpha_2 \tag{4.5}$$

where α_1 and α_2 are the first and the second components in equation (4.4) with highest accuracy rates according to the results in Table 4.6. The proposed SDOLP3F algorithm suggests: (1) positive value indicates that the I_{SDOLP} distribution is a printed photo face; and (2) negative value marks the I_{SDOLP} as genuine face. The detection rates of the SDOLP3F algorithm (4.5) is summarised in Table 4.7.

Table 4.7: The SDOLP3F detection rates for the I_{SDOLP}

	TPR	FPR	Accuracy (AC)
	in percentage (%)		
The SDOLP3F	97.30	8.89	93.90

As shown in Table 4.7, the detection accuracy rate for the I_{SDOLP} by using SDOLP3F algorithm increased to 93.9% compared to the detection accuracy rate of individual measure in Table 4.6. In addition, the FPR is considered as low with only 8.89% while the TPR is highest with 97.3%. From the results, it is apparent that the SDOLP3F algorithm could be the most robust face spoofing detection algorithm.

In this section, investigation was carried out by adopting the Stokes parameters in order to distinguish between genuine face and printed photo faces. The I_{SDOLP} images for each material were generated using equation (3.3) and was analysed by three measures: statistics moments, the BC and the density of distribution mode. As mentioned earlier, similar reflection properties which produced by the real face and photo paper have led to the production of relatively similar I_{SDOLP}. The statistical analysis did not show very convincing results where

only the standard deviation achieves more than 90% accuracy rate. Therefore, the investigations continued by applying two more methods: the bimodality coefficient (BC) and the density of distribution mode. For all measures, a confusion matrix was used as a binary classifier. The summary of the TPR and the FPR for the six individual measures is presented in Table 4.6.

From the results in Table 4.6, the measures or algorithms with accuracy rates more than 90% were selected to be fused in the newly proposed algorithm which was named as the Stokes degree of linear polarisation fast fusion formula (SDOLP3F). The identification accuracy rate of the SDOLP3F was analysed and compared with other individual measures: mean, standard deviation, skewness, kurtosis, the BC and density of distribution mode. As presented in Table 4.7, the accuracy rate of the SDOLP3F is 93.9% which is the highest among the six measures mentioned above. The most striking observation to emerge from the statistical results and the density of distribution mode was that both methods have erroneously identified black real faces as printed photo faces. However, by using the bimodality coefficient (BC) algorithm, these black genuine faces have been successfully classified as real faces. It is difficult to explain these results, but the distribution similarities between black real faces and printed photo faces might be the reason.

4.4 Spoofing face detection based on surface and subsurface reflections

According to Matsubara (2012), polarised images captured under parallel polarisation consist of both surface and subsurface reflections. Polarised images recorded under 90^0 polarisation angle consist of only subsurface reflection. To obtain an image with only surface reflection properties, polarised image under 90^0 polarisation angle is subtracted from polarised image recorded under parallel polarisation. In this study, polarised image that was captured under 90^0 polarisation angle is denoted as Img_{90} while polarised image that was captured under parallel polarisation is labelled as Img_0. In addition, image with only surface reflection is known as S_1 which is one of the Stokes components.

Apart from the I_{pol} and I_{SDOLP} images, polarised image can also be used to differentiate between multiple reflections occurrence from material surfaces. As discussed in the literature review, human skin consists of multilayer structures which produce more than one reflections. To answer one of the research questions in Chapter 1, polarised images Img_{90} which only had subsurface reflection and the Stokes component S_1 that represented images with only surface reflection, were analysed. The reflection differences between the real faces, the printed photo faces and the iPad displayed faces may contribute as one of the spoofing face detection parameters. Although some of the Img_{90} and S_1 images of the real and fake faces were presented in Section 4.2.2 and Section 4.3.1, the images are listed again in Figure 4.29 for comparison purposes.

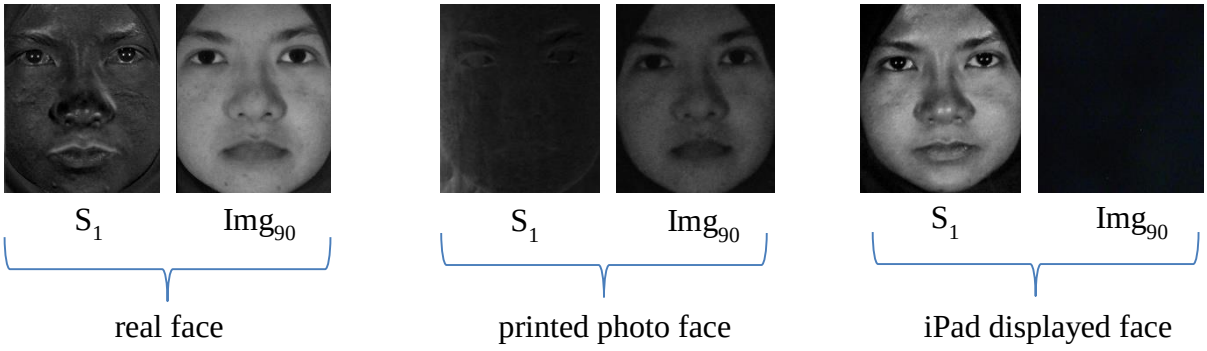

Figure 4.29: The surface, S_1 and subsurface, Img_{90} images

As depicted in Figure 4.29, it is apparent that the S_1 images between real and fake faces are significantly different. However, the subsurface images represented by Img_{90} are relatively similar between the real face, printed photo and iPad displayed faces. These images were then statistically analysed. The statistical results on S_1 image of each subject are presented in Figure 4.30.

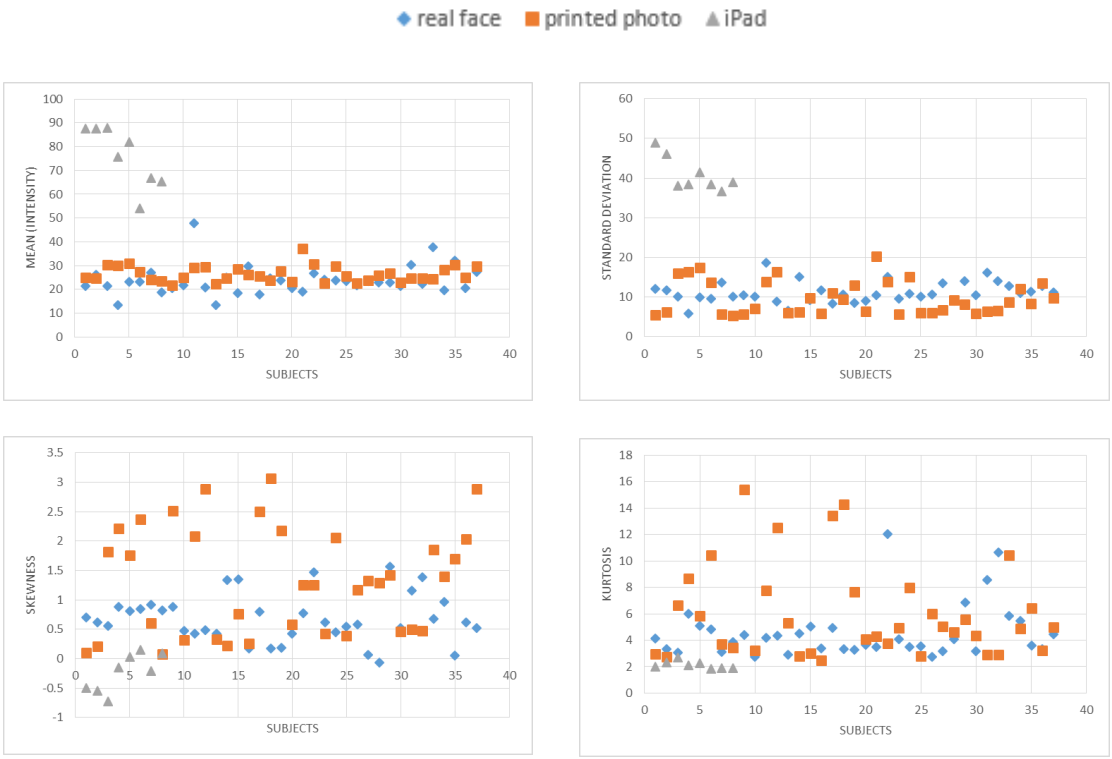

Figure 4.30: Statistics analysis on surface image, S_1 of real and fake faces

As shown in Figure 4.30 , there is a significant difference in the mean and standard deviation between real faces and iPad displayed faces. In contrast, the skewness and kurtosis of these two subjects are similar to each other. Surprisingly, none of these measures were significantly different between real faces and printed photo faces. Furthermore, statistical analysis was applied on the subsurface images and the analysis is known as Img_{90}. The results for the statistical analysis on subsurface images are shown in Figure 4.31. Data from Figure 4.31 can be compared with the data in Figure 4.30 which shows relatively similar statistics results. The mean and standard deviation score between real faces and iPad faces are significantly different. Despite a slight mean intensity difference of Img_{90} between real and photo faces, no other differences were found in the standard deviation, skewness and kurtosis measures.

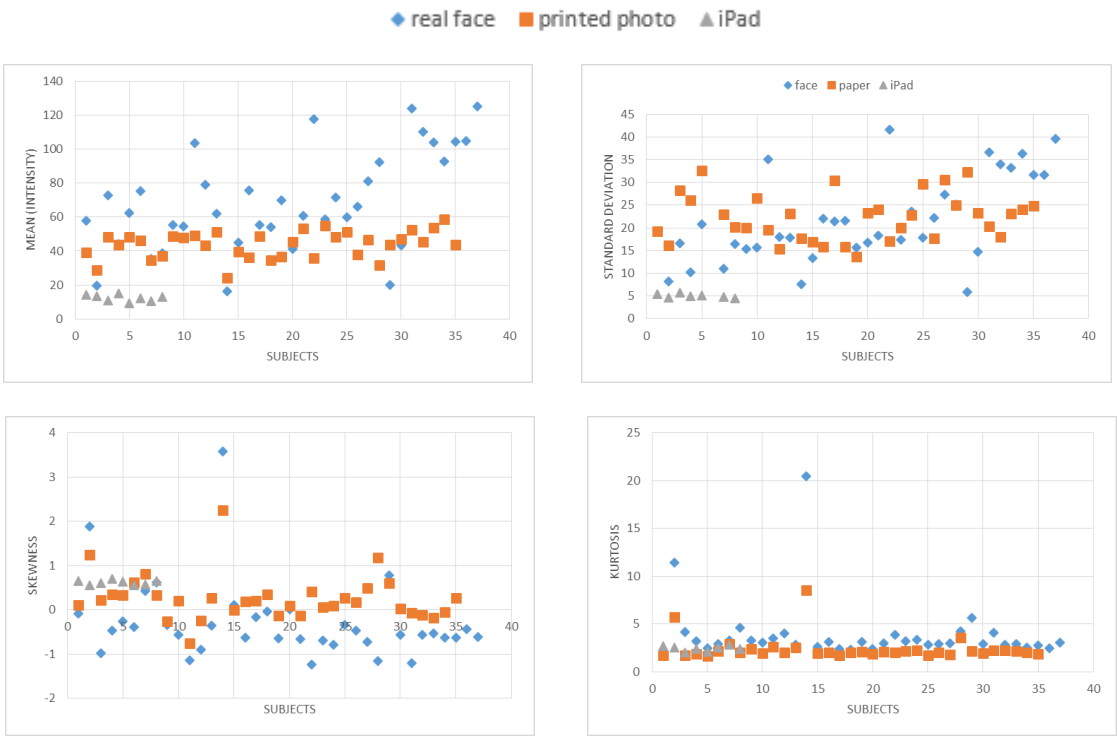

Figure 4.31: Statistics analysis on subsurface image, Img_{90} of real and fake faces

To further examine the distribution of S_1 and Img_{90} for the real faces and the two fake faces, histograms of each subject was plotted and presented in Figure 4.32. As displayed in Figure 4.32, S_1 images for the real face and printed photo face are assumed to have unimodal distributions whereas iPad displayed face images has bimodal distribution. In contrast, Img_{90} for the iPad face shows unimodal distribution while the real and photo faces indicate bimodal distributions. By using equation (4.3), the bimodality coefficient algorithm was then applied to measure the modality of distributions for all S_1 and Img_{90} images in the FaPs and Face-iPad datasets. As mentioned in Section 4.3.3(b), the BC values range from 0 and 1, with empirical values of BC more than 0.555 suggesting bimodal distribution [SAS Institute, (1989)]. Otherwise, the distribution is classified as unimodal. Based on the assumptions initially made above, it seems difficult to differentiate between real and fake faces by the distributions' modality. However, similar to the analysis in Section 4.3.3(b), real face is assumed to have unimodal distribution while fake face with multimodal distribution. Therefore, the modality of each S_1 distribution was measured by the BC and the results are compared in Figure 4.33.

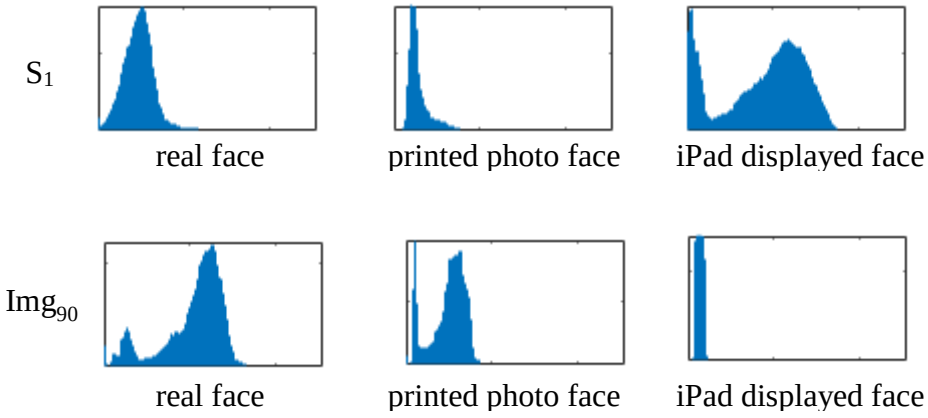

Figure 4.32: Histograms of the S_1 and Img_{90} images

From the data in Figure 4.33, it can be seen that the total number of fake faces were 45 consisting of 37 printed photos and 8 iPad displayed faces. Overall, majority of the fake faces were shown to have unimodal distributions and have been identified as the real faces. The TPR and FPR were calculated by using equation (4.1) and the accuracy rate was measured using equation (4.2). Table 4.8 provides the detection rates of the BC algorithm for both S_1 and Img_{90} distributions. As shown in Table 4.8, the accuracy rates of the BC for both S_1 and Img_{90} distributions are 62.20% which are lower than the accuracy rate of the BC for the I_{SDOLP} distributions in Table 4.5. Meanwhile, data in Table 4.8 also indicate that more than half of the fake faces' distributions were labelled as unimodal.

n = 82	Predicted: Real face	Predicted: Fake face	
Actual: Real face	34	3	37
Actual: Fake face	28	17	45
	62	20	

Surface image, S_1

n = 82	Predicted: Real face	Predicted: Fake face	
Actual: Real face	33	4	37
Actual: Fake face	27	18	45
	60	22	

Subsurface image, Img_{90}

Figure 4.33 The predictions scores for S_1 and Img_{90} based on the BC

Table 4.8: Detection rates of the BC for S_1 and Img_{90}

	TPR	FPR	Accuracy (AC)
	in percentage (%)		
S_1	91.89	62.22	62.20
Img_{90}	89.19	60.00	62.20

Based on the analysis results of the surface and subsurface distributions modality using the BC algorithm, it seems not possible for the modality of distributions for S_1 and Img_{90} to be used as one of the parameters in spoofing face detection. Nonetheless, analysis on the S_1 and Img_{90} images were continued on the density of distribution's mode. The probability density function (PDF) of each S_1 and Img_{90} was plotted. Figure 4.34 shows the PDF plots representing each image in Figure 4.29. Similar to the analysis in Section 4.3.3(c), density value *f(x)* of the highest peak in each distribution was compared between the real and fake faces. The density values between the real faces, printed photo faces and iPad displayed faces are presented in Figure 4.35.

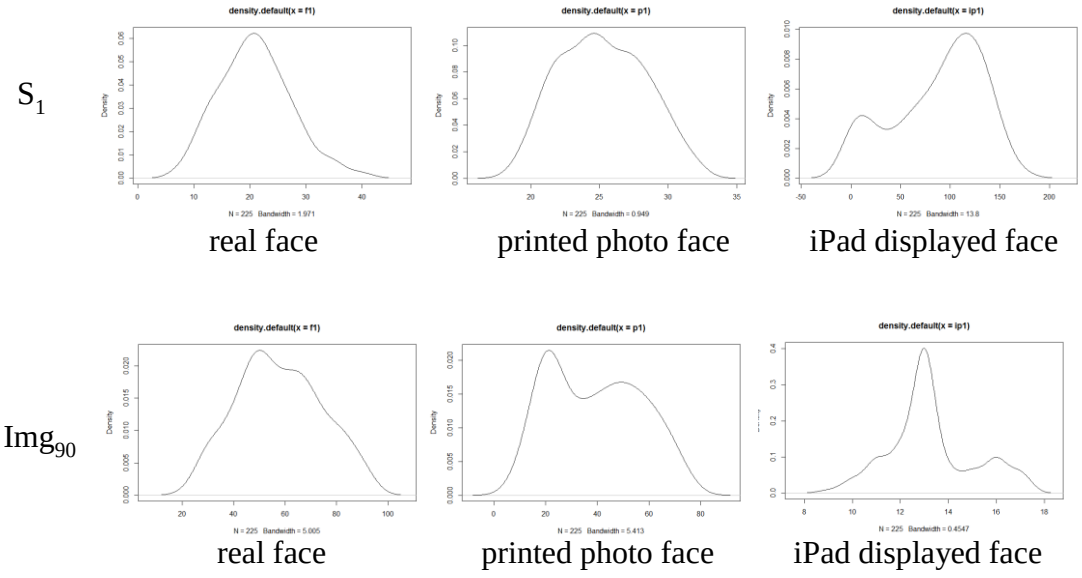

Figure 4.34: The probability density function (PDF) for the S_1 and Img_{90}

The plots in Figure 4.35 shows that the density values of the distribution mode in both S_1 and Img_{90} images between real faces and iPad displayed faces were significantly different. In contrast, no significant difference was found between real faces and printed photo faces in Img_{90} distributions. Despite the similarities of distribution mode's density in Img_{90}, there were slight differences found in S_1 images. A threshold value, 0.08 was selected in which S_1 distribution with density values more than the threshold was identified as printed photos. The detection accuracy rate obtained was 82.43%.

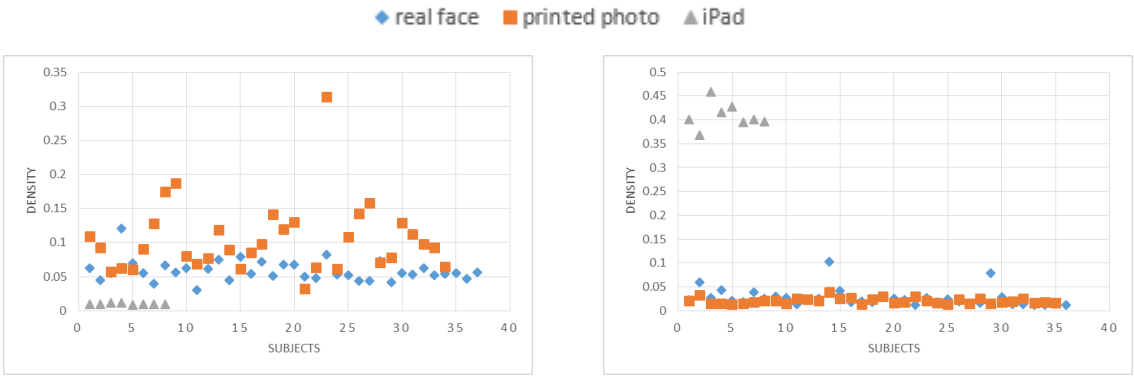

S_1 Img_{90}

Figure 4.35: The density value of distributions mode for S_1 and Img_{90}

The findings of the analysis on the surface, S_1 and subsurface images, Img_{90} showed that real faces and printed photo faces consist of similar reflections properties. Due to these similarities, it is difficult to differentiate between real faces and printed photo faces based on both S_1 and Img_{90} images. On the other hand, iPad attacks can be easily detected based only on the mean intensity of S_1 and Img_{90}. Moreover, density of the iPad distributions mode was also significantly different from the real faces.

According to Bashkatov (2005), the optical properties of the skin layers are determined by the randomly inhomogeneous distribution of blood and various chromophores and pigments in the skin. The epidermis contains pigment particles called melanin. The quantity of melanin in the epidermis determines the colour of the skin. Meanwhile, the dermis layer contains two main ingredients: haemoglobin and collagen. One question that needs to be asked, however, is whether the skin optical properties varies according to skin colours. According to So-Ling and Ling (2001), less blood is supplied to dark skin colours compared to fair skins types, thus

resulting in less scattering. With less blood supply, the quantity of haemoglobin carried by the blood cells in the dermis is also small. Dark skin also has smaller collagen fibres than fairer skin. Apart from that, dark skin types consist more melanin than fairer skin colour [Zaidi (2016)]. A study by Bersha (2010) proved that black skin colours have the highest melanin index. These previous studies provide additional evidence to support that the skin optical properties vary according to skin colours. The correlation between optical properties and reflection has been explained by Li and Ng (2009) as: strong scattering, large diffuse reflection; strong absorption, less diffuse reflection.

Haemoglobin, collagen and melanin act as strong forward scattering agents. As explained above, dark skin types have less haemoglobin and collagen but higher amount of melanin compared with fair skin types. The experiment in Section 4.4 showed that when polarised light wave which vibrates parallel to the skin surface strike on the skin, the incident light wave was reflected in similar wave direction by the oily cells on top of the epidermis. This reflection is known as specular reflection. The quantity of the oil produced on the skin surface affected the amount of surface reflection. Black genuine face is more hydrated and oily than white facial skin [Li and Ng (2009)]. An implication of this is the specular reflection of the black skin was higher compared with the surface reflection of the fair facial skin.

The light component that was not reflected entered the skin firstly to the epidermis layer then to the dermis layer. For dark skin, the quantity of melanin in the epidermis layer was high, thus resulting in strong scattering but less absorption. Most of the light component was scattered by the melanin in which part of the component re-emerged into the air and the rest traveled to the dermis layer. Since dark skin consists less haemoglobin and collagen, most of the transmitted light was absorbed. Taken together, the dark skin types produced a large diffuse reflection. In contrast, fair skin groups which consist less melanin caused most of the transmitted polarized light in the epidermis layer to be absorbed. This has resulted in small diffuse reflection by the fair skin types. These findings have answered the question that the skin optical properties vary according to the skin colour. Moreover, the differences in the skin optical properties have also made the I_{SDOLP} image of the genuine black skin brighter than other skin colours' I_{SDOLP} image.

4.5 Conclusion

The main goal of this chapter was to construct a robust face anti-spoofing algorithm based on the analysis of the polarised images. The first analysis was carried out to differentiate between real face and iPad attacks. The first parameter used was the DOP which statistically showed the potential in detecting iPad displayed faces based on the polarisation image, I_{pol}. Since the I_{pol} images have low intensity, no histogram can be generated for further studies. The same DOP parameter was also applied to detect printed photo faces. Statistically, the printed photo faces was able to be differentiated from the real faces based on the DOP.

Further investigations were carried out by using the Stokes parameters as trials to differentiate between genuine and fake faces. It was found that intensity of the I_{SDOLP} images of iPad displayed attacks was higher than the I_{SDOLP} of the real faces. Statistically, the intensity differences between genuine faces and iPad attacks are significant thus can be used to differentiate the two materials. In the other experiment, the Stokes parameters were applied to distinguish between real faces and printed photos. Only two of the statistics measures achieved detection accuracy rates more than 90%. Therefore, the analysis was continued by using the bimodality coefficient (BC) algorithm and the density of the distribution mode. At this stage, there were six measures used to study the I_{SDOLP} images of real faces and printed photos. Only two of the measures achieve detection accuracy rates greater than 90%. A fusion formula, SDOLP3F was proposed where scores of any measure with accuracy rate higher than 90% were fused. The accuracy rate for the SDOLP3F algorithm is the highest compared to the individual measures.

The next study was conducted to examine the impact of using near infrared light in a polarisation imaging system to detect spoofing faces. The experimental setup was designed to operate at 850nm. The DOP and the Stokes parameters were applied to investigate the differences between real and spoofing faces. Surprisingly, the results could not be used to differentiate the materials. The findings suggest that NIR light is not suitable for surface reflection's analysis of human skin and paper because the NIR penetrates deeper through these two materials.

The final working chapter in this thesis was to investigate the accuracy of depth pixels captured by three versions of depth sensors. Although the experiments were not about face

spoofing detection, but the results could contribute in further reconstruction of 3D spoofing face database by using depth sensor. The findings from the investigations suggest that none of the Microsoft Kinect for Xbox 360, Microsoft Kinect for Windows v2 and Asus Xtion Pro Live are suitable for 3D face reconstruction for the purpose of spoofing face detection according to the potential errors made by the fluctuated pixels.

The following conclusions can be drawn from the present study. This research extends the knowledge that besides the physical properties, the I_{SDOLP} image was also influenced by the optical properties of the subject even though the subject was made of similar material. The results of this research support the idea that each material has different types of reflections. Hence, by examining the reflections using suitable methods, the materials could be separated from each other. The next major finding was that the difficulties to differentiate genuine black faces from the paper photos based on the I_{SDOLP} features. To further identify black skin faces from photo faces, the BC algorithm can be used.

Although the study in this chapter is based on a small sample of participants, the analyses on the physical and optical properties of the subjects suggest that the polarised light was able to highlight the properties to be implemented in the SDOLP3F algorithm as the robust face anti-spoofing method. More research, however, is required to determine the efficacy of the SDOLP3F algorithm. It is recommended that further research to be conducted in the following areas: (a) bigger sample size with varies skin colours particularly more black skin types in the dataset; (b) the classification between real face and a 3D facial mask made of different materials such as rubber, hard resin and silicon.

Chapter 5: Near Infrared Polarisation Imaging System

5.1 Face Spoofing Countermeasures

As was explained in the literature review, human eye is only capable to see radiation within the visible spectrum. The wavelength for the visible light is in the range of 400 – 700 nanometre (nm) [Ryer (1997)]. In Chapter 4, the experiments were carried out using two table lights as the visible light source of the self-developed polarisation imaging system. Two parameters, which were the degree of polarisation (DOP) and the Stokes parameters have been used to generate the polarisation image, I_{pol} and the I_{sdolp} image for further analysis. The results obtained were successfully distinguished between the genuine face and the other two fake traits: the printed photo faces the iPad displayed faces.

In previous studies by other researchers, near infrared (NIR) was successfully used in material classification and showed superior to visible lights in some aspects. In addition, NIR was also used by previous researchers to detect human skin by exploiting skin reflectance characteristics [Kanzawa et al. (2011), Nunez and Mendenhall (2008)]. Other than that, NIR light has been widely used for the in-vivo tissue analysis particularly in biomedical environment [Ali et al. (2004), Henderson and Morries (2015)]. In-vivo study is referred to the analysis and characterization of biomolecules and biological systems using living organisms [Nasr (n.d)]. All of the studies stated above have produced positive results. Despite the success of NIR in those researches, questions have been raised about the performance of polarised NIR in similar studies. One study by Shao et al. (2010) utilised the polarised NIR imaging for improving colonic cancer detection. The results showed that polarised NIR light was able to distinguish between normal and cancer tissue by analysing the polarisation ratio image. Driven by positive results from the previous NIR polarisation imaging analyses, it can therefore be assumed that the polarised NIR reflectance could be used to detect spoofing faces in face recognition systems.

As was discussed in Section 2.3.3, near infrared (NIR) light is a source of light beyond the visible light spectrum. The visible light spectrum is within 400 – 750nm while the wavelength of NIR light is within the region between 750 to 1400 nm [Liew (n.d.)]). NIR

instruments use infrared light to illuminate an object. NIR spectroscopy is defined as imaging technique used for research purposes [Bakker et al. (2012)]. In this chapter, polarised NIR light was used as light source in a face imaging system as trial to differentiate between genuine human face, printed photo faces and iPad displayed faces. The degree of polarisation (DOP) and the Stokes parameters were adopted to examine the differences between the real and fake faces recorded under NIR radiation. The experiment setup is explained in detail in the next section.

5.2 Experimental setup

The NIR imaging measurements were performed using an e-gate camera system available in the Virtual Reality Computer Lab, Department of Computer Science, University of Reading. The NIR imaging system consists of NIR LED lights with 850 nm wavelength which were mounted on the left and right side of the camera. Two pieces of linear polariser denoted as P_2 and P_3 were attached to each of the NIR LED lights. The P_2 and P_3 were aligned in parallel to each other according to the process as explained in Section 3.2. One more linear polariser which was coupled with an angle rotator was attached to the camera lens. Similar to the experiments in Chapter 4, polariser in front of the camera lens is a glass polariser and known as P_1. Figure 5.1 illustrates the e-gate camera system which was designed to operate at 850nm of NIR light, used to record polarised images of genuine faces, printed photo faces and iPad displayed faces.

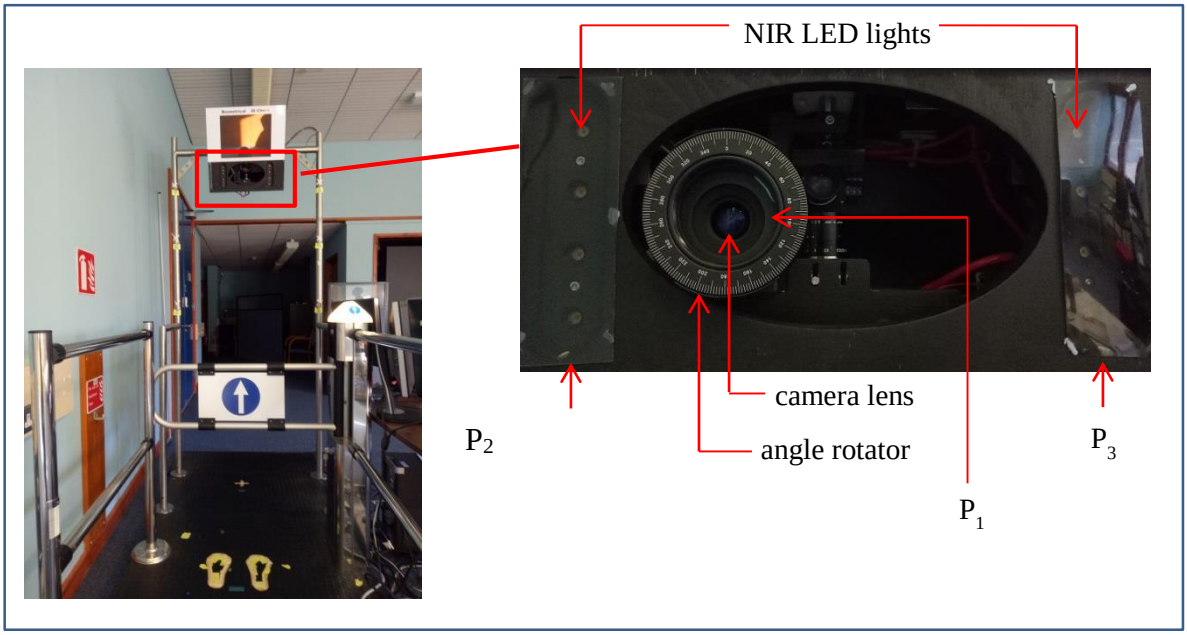

Figure 5.1: The NIR polarisation imaging system

5.3 Dataset

As in Chapter 4, the Face-iPad and FaPs dataset were self-developed since no polarised image dataset was available. In this chapter, the self-created dataset is named as NIR Face-Paper-iPad (NIR-FPi) dataset. The polarised images in the NIR-FPi dataset were self-recorded by using the NIR polarisation imaging system as shown in Figure 5.1. For the data collection process, 25 people among students and staff were randomly selected as the experimental subjects of this study. The subjects consist of 14 men and 11 women from three skin colours: Asian, Black and Caucasian. For recording process, the subjects were asked to stand in front of the camera at the same camera distance as the experiments in Chapter 4, which was 80cm. The same recording processes as in Section 4.2.2 were repeated for each genuine face, printed photo faces and iPad displayed faces. SURF algorithm was then applied for registration and alignment techniques to all polarised images. Finally, one final processed polarised image was produced for each genuine and fake faces at each polarisation angle. The structure of this NIR dataset is illustrated in Figure 5.2. The total number of NIR polarized images for the real face, the paper photo and the iPad display in the NIR-FPi dataset are 912 images.

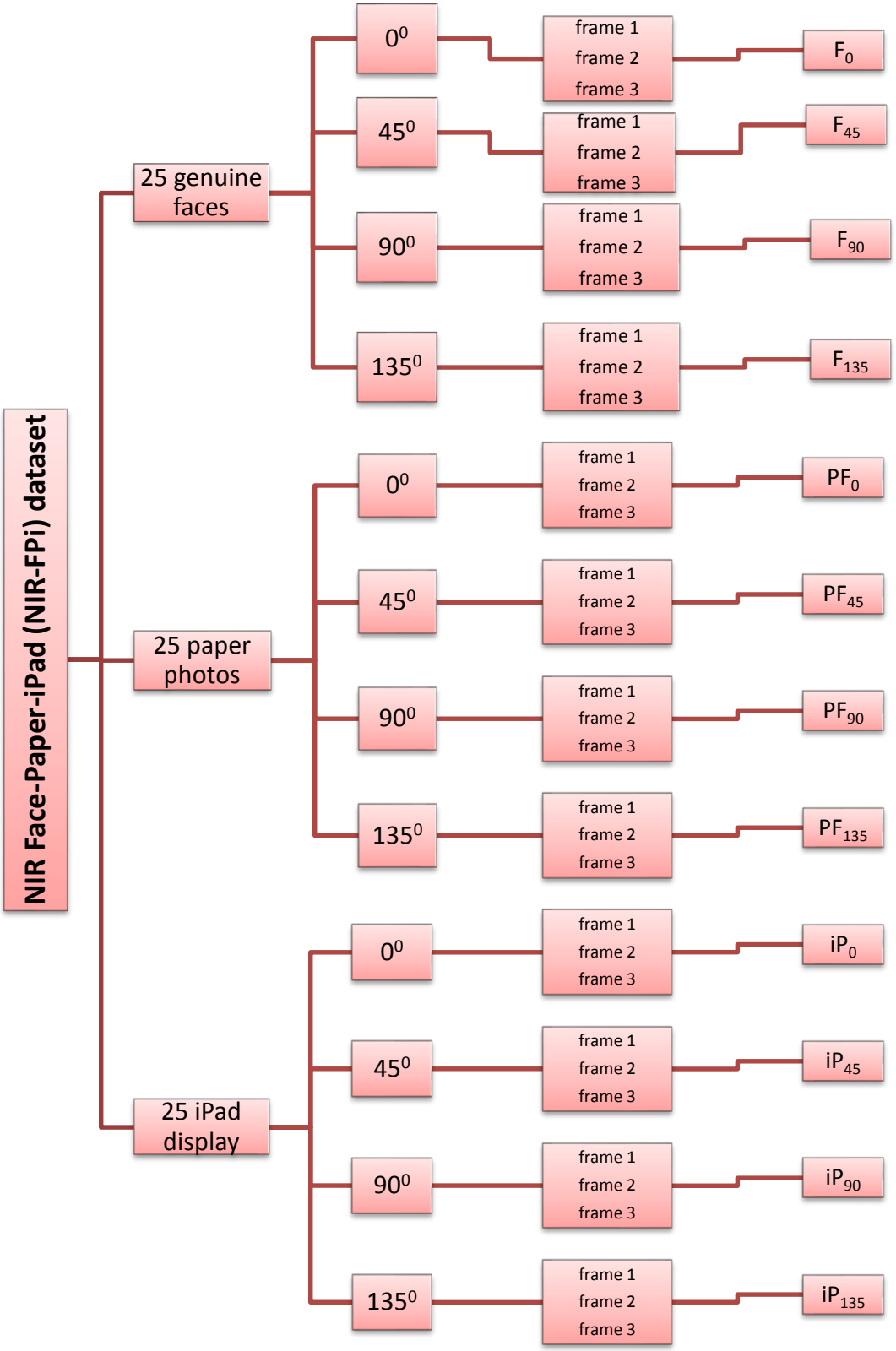

Figure 5.2: Structure of the NIR-FPi dataset

Since there were three different skin colours, one image from each colour group is presented throughout this chapter for comparison purposes. Figure 5.3 compares the NIR polarised images between the genuine subjects, the printed photo faces and the iPad displayed faces at four polarisation angles. As depicted in Figure 5.3, the appearance of the genuine face images and the paper photos are more or less similar. In contrast, the iPad display images seem darker than the genuine faces. The most apparent result to emerge from the images is the iP_{90} images became completely dark, similar to the iP_{90} images in the previous chapter. However, further analysis might be able to describe the difference between the three materials. The next section will discuss on the analysis of the degree of polarisation (DOP) for genuine and fake traits as trials to differentiate between them.

5.4 The degree of polarisation (DOP)

As explained in Chapter 3, the degree of polarisation (DOP) was used to measure the partially polarised light reflected from a material surface. In this chapter, the effect of using a single wavelength light source, for example the near infrared (NIR) light, on the DOP of the genuine human face, printed photo and iPad displayed faces was investigated. The DOP value was evaluated from an image known as polarisation image, I_{pol}. To generate the I_{pol}, two components of images were required: S_0 and S_1. These two image components were derived from equation (3.2). Finally, I_{pol} of each genuine and fake faces were obtained by using equation (3.6). The S_0, S_1 and the I_{pol} images are presented in Figure 5.4. As presented in Figure 5.4, polarisation image for the real face, photo face and iPad face are labelled as F_{pol}, PF_{pol} and iP_{pol}, respectively. From the images in Figure 5.4, it is apparent that there are no significant difference between the F_{pol}, PF_{pol} and iP_{pol}. The mean intensity of each F_{pol}, PF_{pol} and iP_{pol} was recorded as 0 which indicates that the reflected light from the material surfaces was completely unpolarised [Sarkar et al. (2011)].

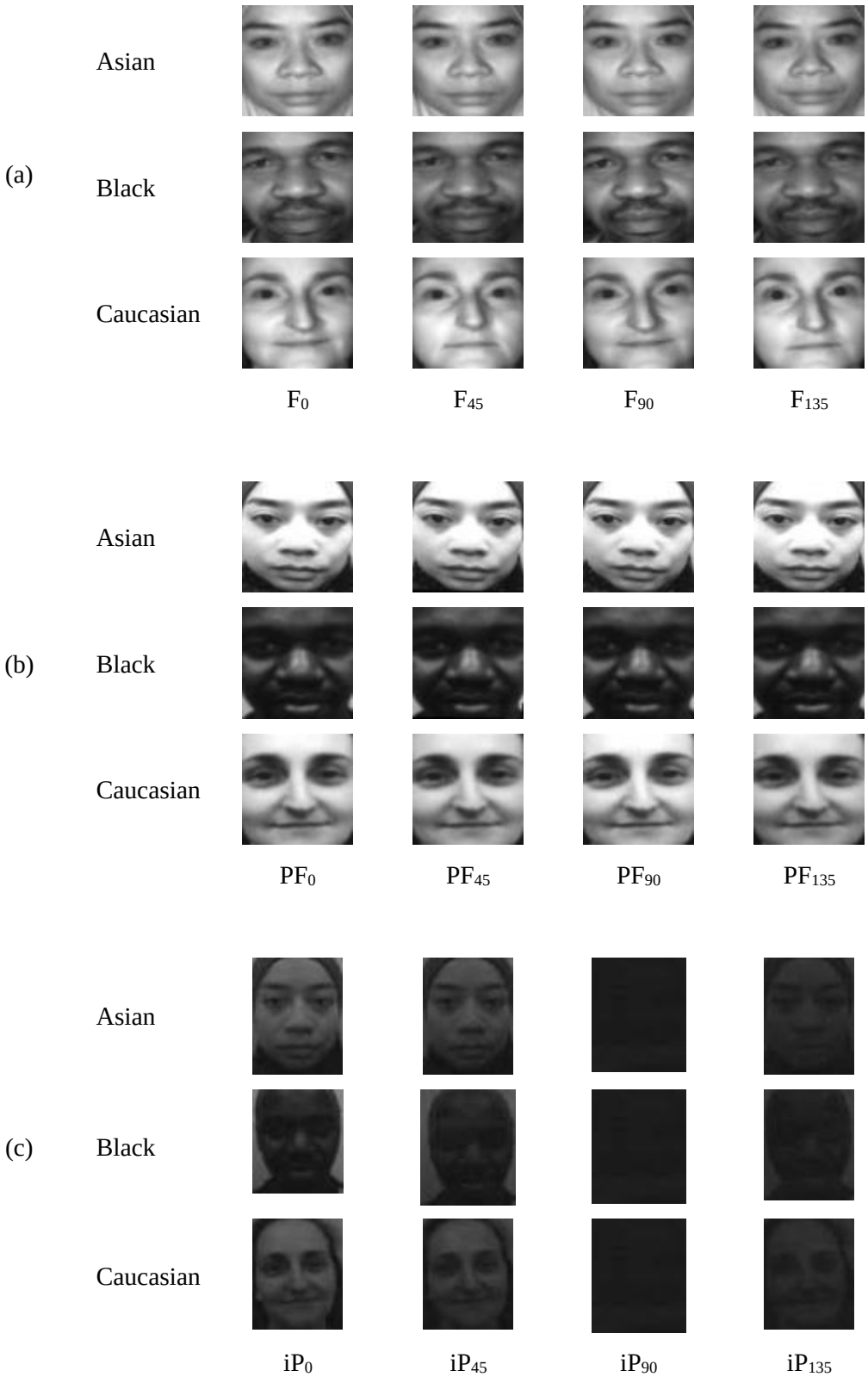

Figure 5.3: The NIR polarised images at four polarisation angles of (a) the genuine faces, (b) printed photo faces and (c) iPad displayed faces.

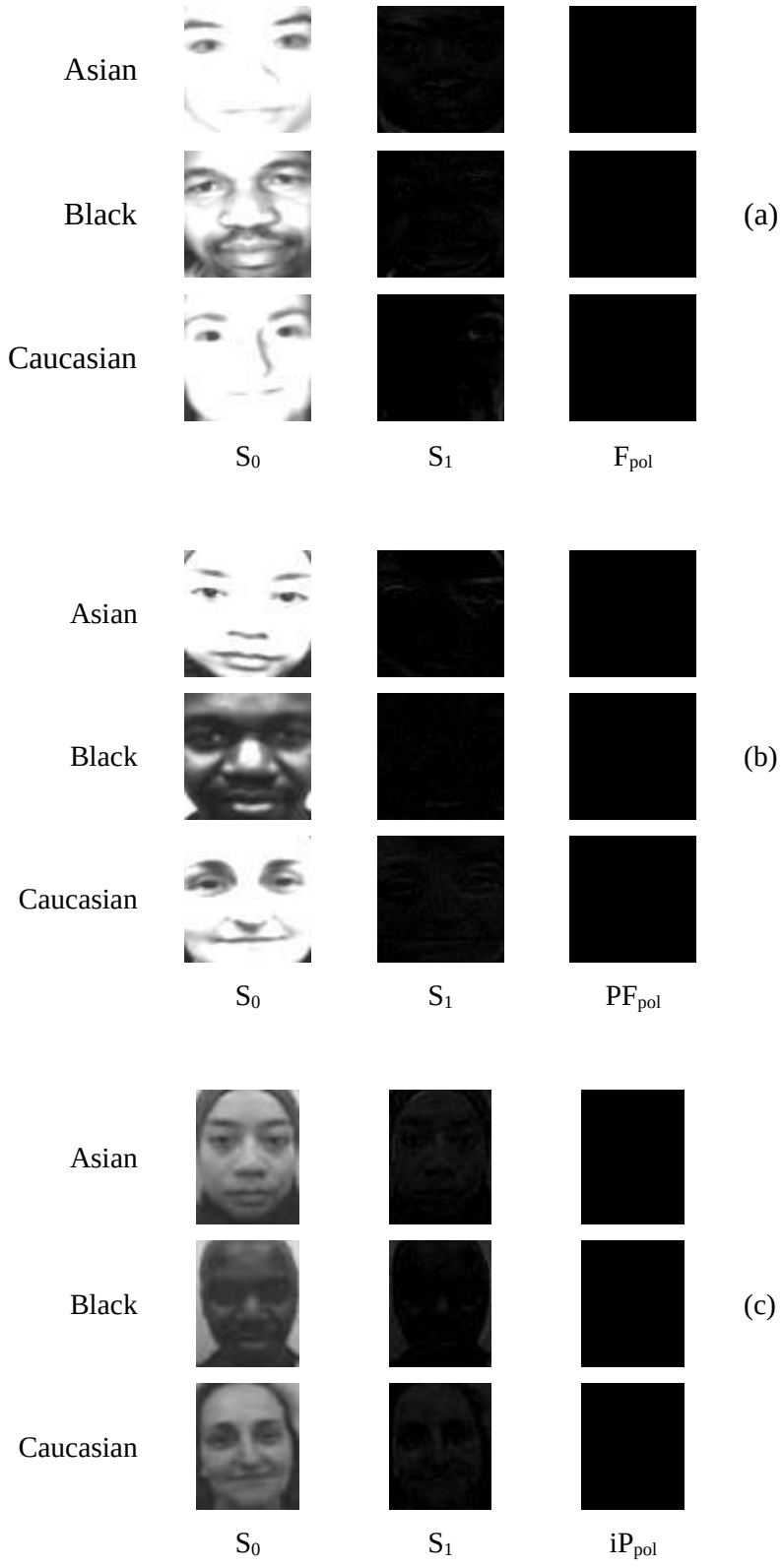

Figure 5.4: The S_0, S_1 and I_{pol} images for the (a) real faces, (b) printed photo faces, and (c) iPad displayed faces

From the results in this section, the DOP value for all polarisation images, I_{pol} of the genuine face, the printed photo faces and the iPad displayed faces was zero. The DOP value of zero indicates that the reflected light of the materials surface was completely unpolarised [Sarkar et al. (2011)]. This result may be explained by the fact that the polarisation of the reflected light depends on the materials' physical properties. As been discussed in Chapter 4, the physical properties of the genuine face and printed photo are relatively similar. The human skin consists of multilayer structures and the paper is made up of multiple ingredients such as fibre composition. Both materials obtained two types of reflections: surface and subsurface reflections. Although the interaction between NIR light and the human skin is similar as the visible light, NIR light penetrates deeper into human skin compared to visible light [Jaminet (2015)]. In Section 4.3.2, I_{pol} under visible polarisation achieved more than 90% detection accuracy rate between genuine and photo faces. However, in this chapter, no degree of polarisation was recorded due to the dark intensity of the NIR I_{pol}.

5.5 The Stokes parameters

As implemented in Chapter 4, the second parameter used to detect spoofing faces is the Stokes parameters. In this chapter, the Stokes parameters were applied as trial to distinguish between real and fake faces in the NIR-FPi dataset. As explained in Section 3.2.1, the Stokes parameters consisted of four components: S_0, S_1, S_2 and S_3. Since linear polarizer was used in this study, the S_3 component was omitted. The other three Stokes components were generated by using equation (3.2). Then, an image known as the Stokes degree of linear polarisation, I_{SDOLP} was obtained using equation (3.3). Figure 5.5 presents the Stokes components (S_0, S_1, S_2) and the I_{SDOLP} images for the real and fake faces.

Figure 5.5 shows that the I_{SDOLP} between real faces and printed photo faces seem relatively similar to each other. The I_{SDOLP} of the iPad displayed faces was slightly brighter compared to the I_{SDOLP} of the genuine faces. However, that was just a coarse comparison based on human eye. To visualise the distribution of data for each I_{SDOLP}, histogram of each image was plotted. Figure 5.6, Figure 5.7 and Figure 5.8 provides the histograms of each I_{SDOLP} for all real and fake faces in NIR-FPi dataset.

As can be seen in Figure 5.6, Figure 5.7 and Figure 5.8, the shapes of the histograms amongst each material are uneven. For example, some of the histograms in Figure 5.6 have sharp peak with small distributions while the others show wider data distributions with more than one peak. Similar description goes to the histograms in Figure 5.7 and Figure 5.8. To further verify the distributions between the materials, three measures or algorithm were applied: (1) the statistical analysis; (2) the bimodality coefficient (BC); and (3) the density of distribution mode.

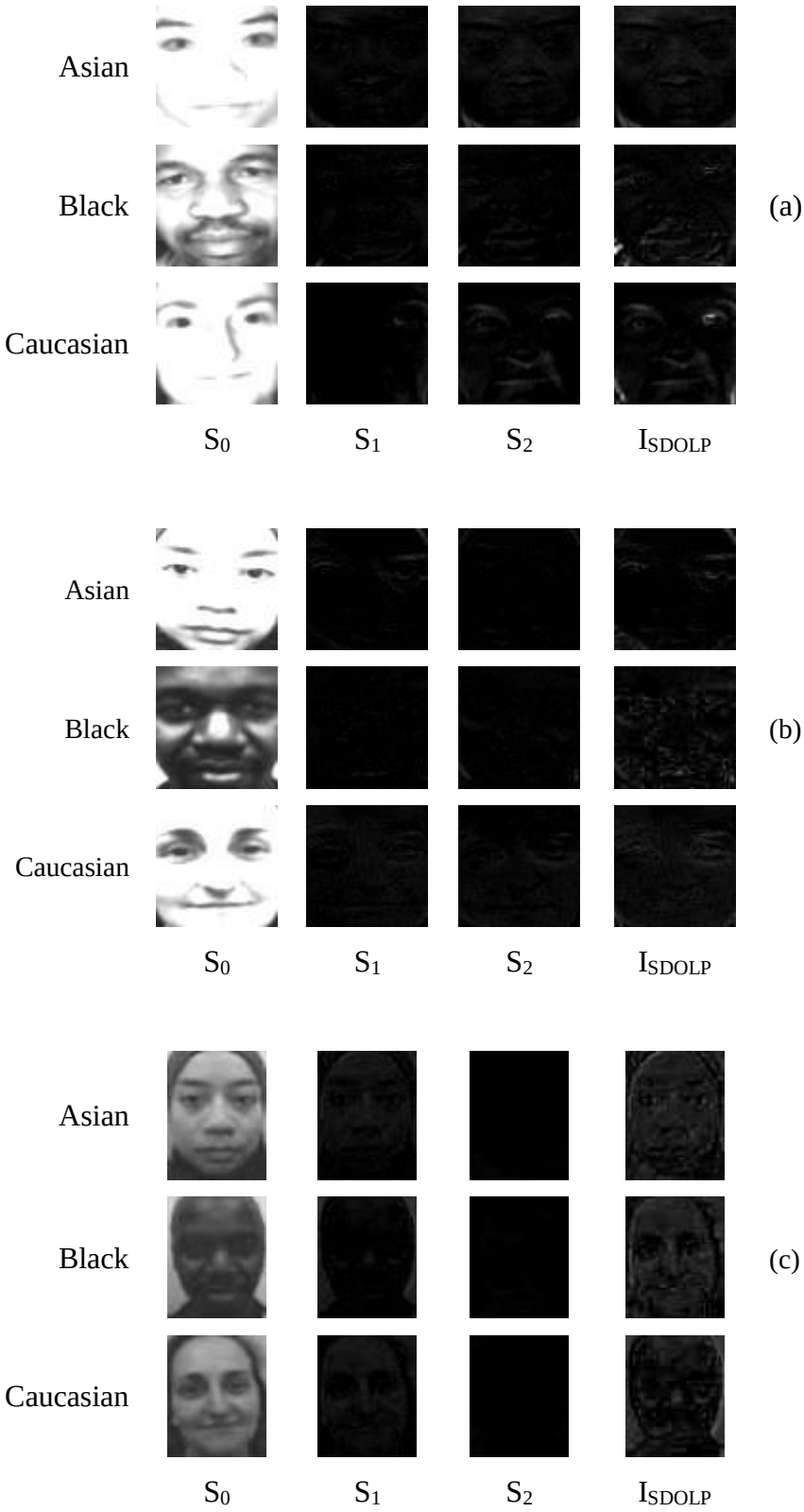

Figure 5.5: The S_0, S_1, S_2 components and the I_{SDOLP} for the (a) real faces, (b) printed photo faces, and (c) iPad displayed faces

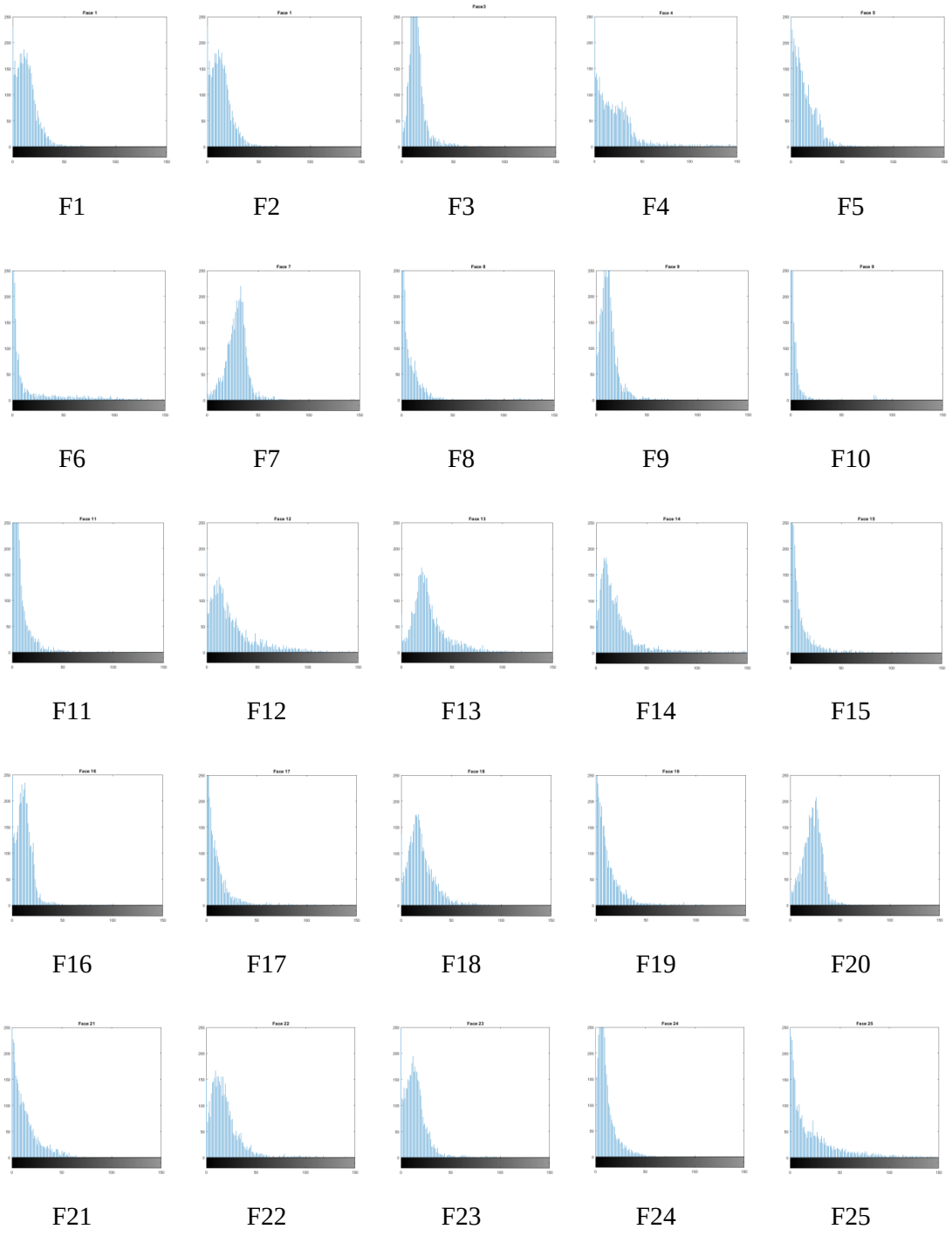

Figure 5.6: Histograms for I_{SDOLP} genuine faces

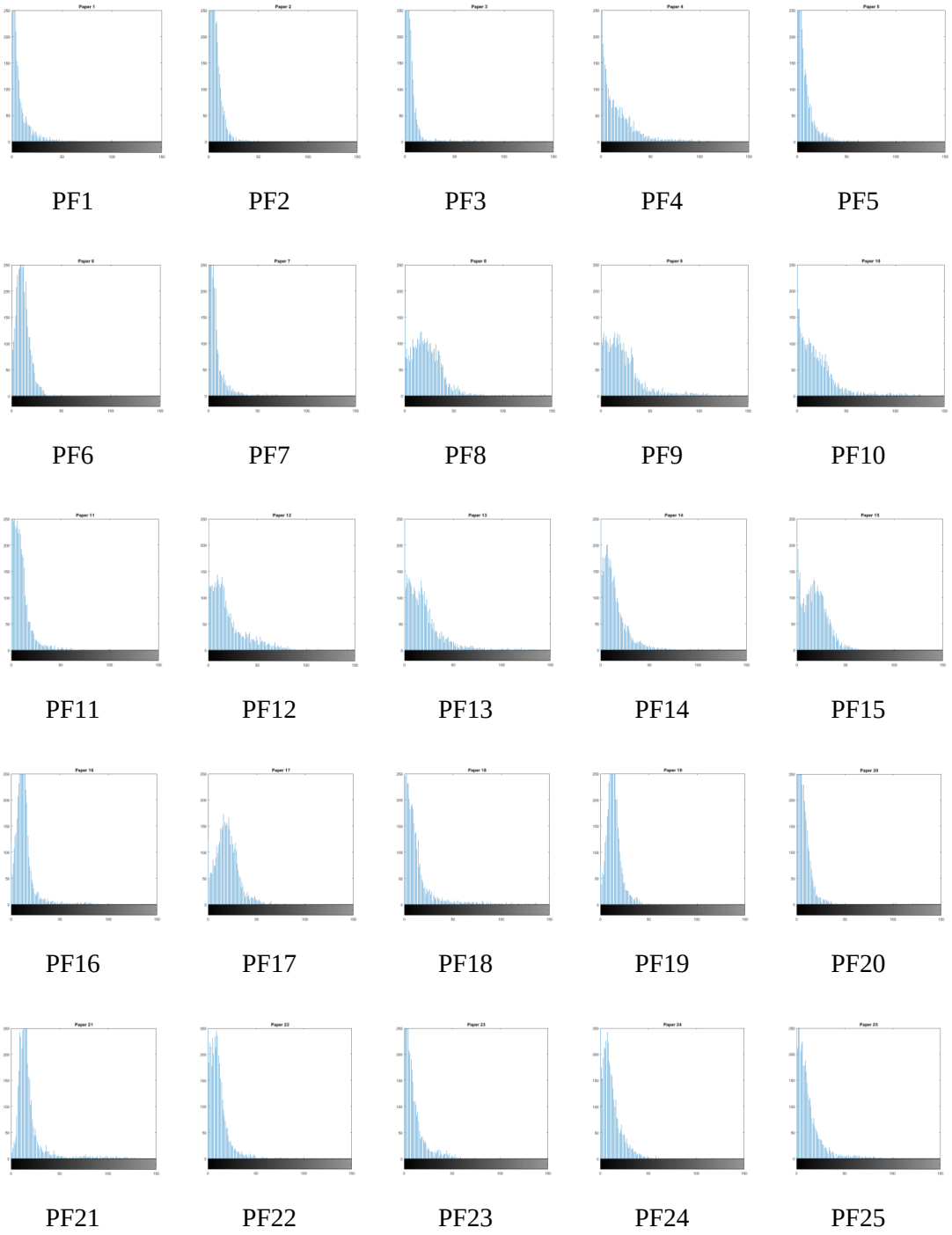

Figure 5.7: Histograms for I_{SDOLP} printed photo faces

Figure 5.8: Histograms for I_{SDOLP} iPad displayed faces

5.5.1 Statistical analysis

Similar to the analysis in Chapter 4, the statistical analysis was the first measure used to interpret the data distribution of each I_{SDOLP}. Four statistical moments (mean, standard deviation, skewness and kurtosis) were applied to measure distributions of each I_{SDOLP}. The mean, standard deviation, skewness and kurtosis were calculated using equations 3.9, 3.10, 3.11 and 3.12, respectively. The statistical results can be compared in Figure 5.9.

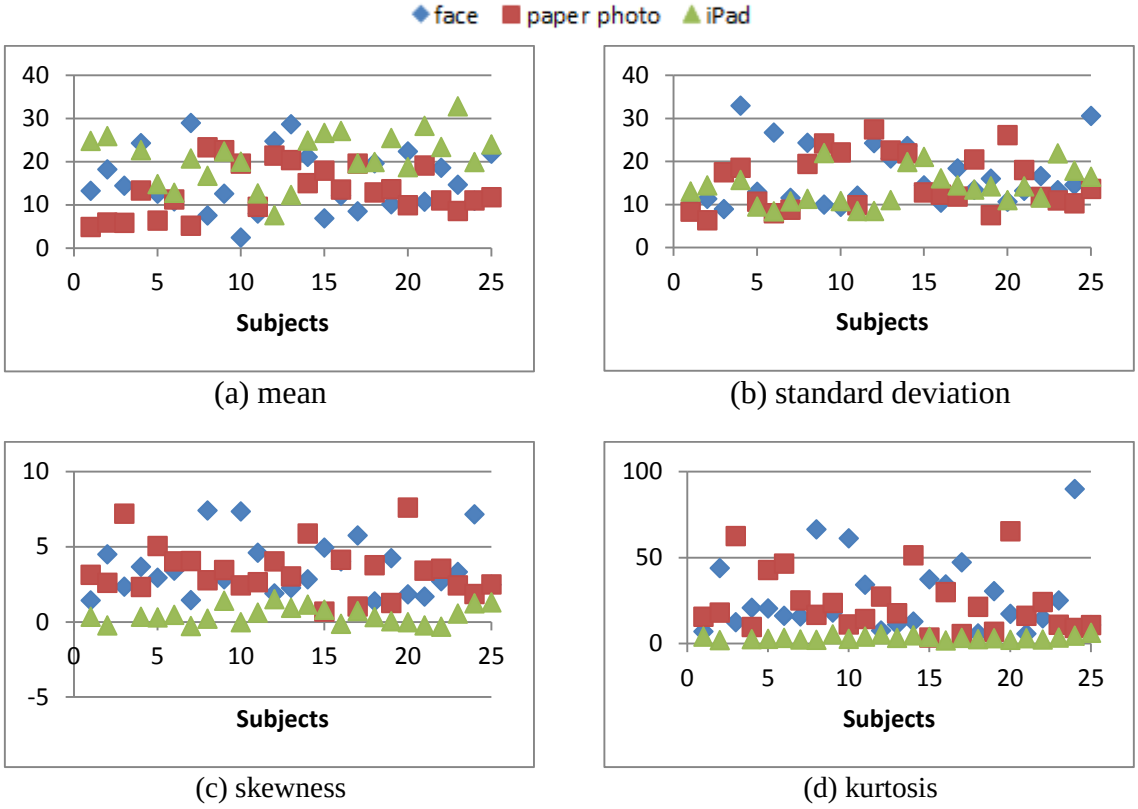

(a) mean (b) standard deviation

(c) skewness (d) kurtosis

Figure 5.9: The statistical analysis of NIR I_{SDOLP}

The results in Figure 5.9 will now be explained individually. Firstly, the mean of each material shows relatively similar values as shown in Figure 5.9 (a). Secondly, the standard deviation scores for the three materials are scattered and mixed among each other as shown in Figure 5.9 (b). Turning now to the results for the skewness as illustrated in Figure 5.9 (c). The skewness values for the genuine faces and the paper photos are approximately similar; however, there are slight skewness value differences between the real faces and the iPad images. Most of the skewness values of the iPad images are lower than the real faces. The

fourth plot as presented in Figure 5.9(d) represent the kurtosis scores for each subject. From the figure, it is apparent that the kurtosis value for the real faces and printed photo faces are within the same range. Meanwhile, the iPad fake faces have lower kurtosis than the real faces which could be used to differentiate between them.

Due to the results in Figure 5.9, the mean and the standard deviation were omitted from further investigations. In addition, none of the four statistical results were able to differentiate between genuine faces and the photo faces. Therefore, the I_{SDOLP} for both genuine and printed photo faces were statistically indistinguishable. Turning now to the results for the iPad attacks. Since the skewness and the kurtosis value for the iPad faces are different compared to the skewness and kurtosis value of the genuine faces, these differences could be adopted as one of the classification parameters. Moreover, both skewness and kurtosis scores of the iPad images were consistent and relatively even. Next, a threshold value for each skewness and kurtosis that was considered as the most significant boundary between the two materials was chosen as classification threshold. From the data in Figure 5.9, two values were selected as the threshold: 1.5 for the skewness; and 6.0 for the kurtosis.

The I_{SDOLP} is classified as a real face if the skewness and the kurtosis scores are more than the corresponding thresholds. Otherwise, the image is identified as an iPad attack. By using the confusion matrix in Table 4.1, the predicted results are presented in Figure 5.10. From the data in Figure 5.10, the true positive rate (TPR) and the false positive rate (FPR) for both were calculated by using equation (4.1) while the accuracy rate was measured by using equation (4.2). The detection results are presented in Table 5.1.

	Predicted: Real face	Predicted: iPad attack	
Actual: Real face	22	3	25
Actual: iPad attack	1	24	25

(a)

	Predicted: Real face	Predicted: iPad attack	
Actual: Real face	23	2	25
Actual: iPad attack	1	24	25

(b)

Figure 5.10: The prediction scores for the (a) skewness and (b) kurtosis

From the data in Table 5.1, the TPR scores for the skewness and the kurtosis are 88% and 92%, respectively. Meanwhile, the FPR for both skewness and kurtosis is 4%. In addition, both measures show high accuracy rates with 92% for skewness and 94% for kurtosis. According to the high accuracy rates, the skewness and kurtosis may be applied to differentiate between the genuine face and iPad attack under NIR polarisation imaging. Since the statistical measures were not able to distinguish between the paper photo image and the real face, further investigations were conducted. Next, the shape of histograms of the real and fake faces was investigated for any possible significant values that could be applied as a classification parameter.

Table 5.1: Detection rates for the skewness and kurtosis of the I_{SDOLP} between real faces and iPad displayed faces

	TPR	FPR	Accuracy (AC)
	in percentage (%)		
Skewness	88.0	4.00	92.00
Kurtosis	92.0	4.00	94.00

5.5.2 The bimodality coefficient (BC)

The bimodality coefficient (BC) was the second measure used to determine the modality of a distribution. The data distributions of the I_{SDOLP} for the real faces, the printed photo faces and the iPad displayed faces were visualised in the form of histograms as presented in Figure 5.6, Figure 5.7 and Figure 5.8, respectively. From the figures, it is quite revealing that the shapes of histograms between the real and fake faces were uncertain. For a clearer comparison, probability density function (PDF) was generated for all genuine and fake traits. The PDF plots for some of the real and fake faces are set out in Figure 5.11: real faces were labelled as F; the printed photo faces were denoted as P; and the iPad displayed faces were named as iP. From the plots in Figure 5.11, the appearance of the PDF plots between the materials are relatively similar, for example, most of the plots have one sharp peak. However, the plots shape of each material seemed uneven. The plots for the real faces, for instance, some

of the plots are symmetrical while the others are skewed to the right. The plot patterns are also similar to the printed photo and the iPad attacks.

In this study, NIR light was used in the polarisation imaging system to capture polarised images. The I_{SDOLP} images obtained were relatively similar amongst the real and fake faces. Unlike the study that used polarised visible light in Chapter 4, no modality assumption on the distributions can be made for NIR I_{SDOLP} in this chapter. This is due to the PDF shape similarities between the real and fake traits as shown in Figure 5.11. Therefore, further assessment using the bimodality coefficient (BC) and the Hartigan's dip statistic (HDS) algorithms was carried out to evaluate the modality of each distribution. The BC was examined by using equation (4.3) and the algorithm for the HDS measure was proposed by Hartigan and Hartigan (1985) namely as R diptest-package algorithm.

As explained in Chapter 4, the empirical values of BC more than 0.555 suggests bimodal distribution; the p-values of HDS that is less than 0.5 are considered as bimodal distribution. The results of the BC and the HDS for the PDF plots in Figure 5.11 are summarized in Figure 5.12. The results in Figure 5.12 are consistent with the earlier assumption that there would similarities in the shape of the PDF plots of the three faces. For instance, the HDS algorithm classified almost all of the distributions as multimodal distributions. Meanwhile, the BC identified more than half of the distributions for the real faces and the printed photo faces as multimodal distributions whereas the others have been determined as unimodal distributions. For the iPad attacks, the BC classified almost all of the distributions as unimodal.

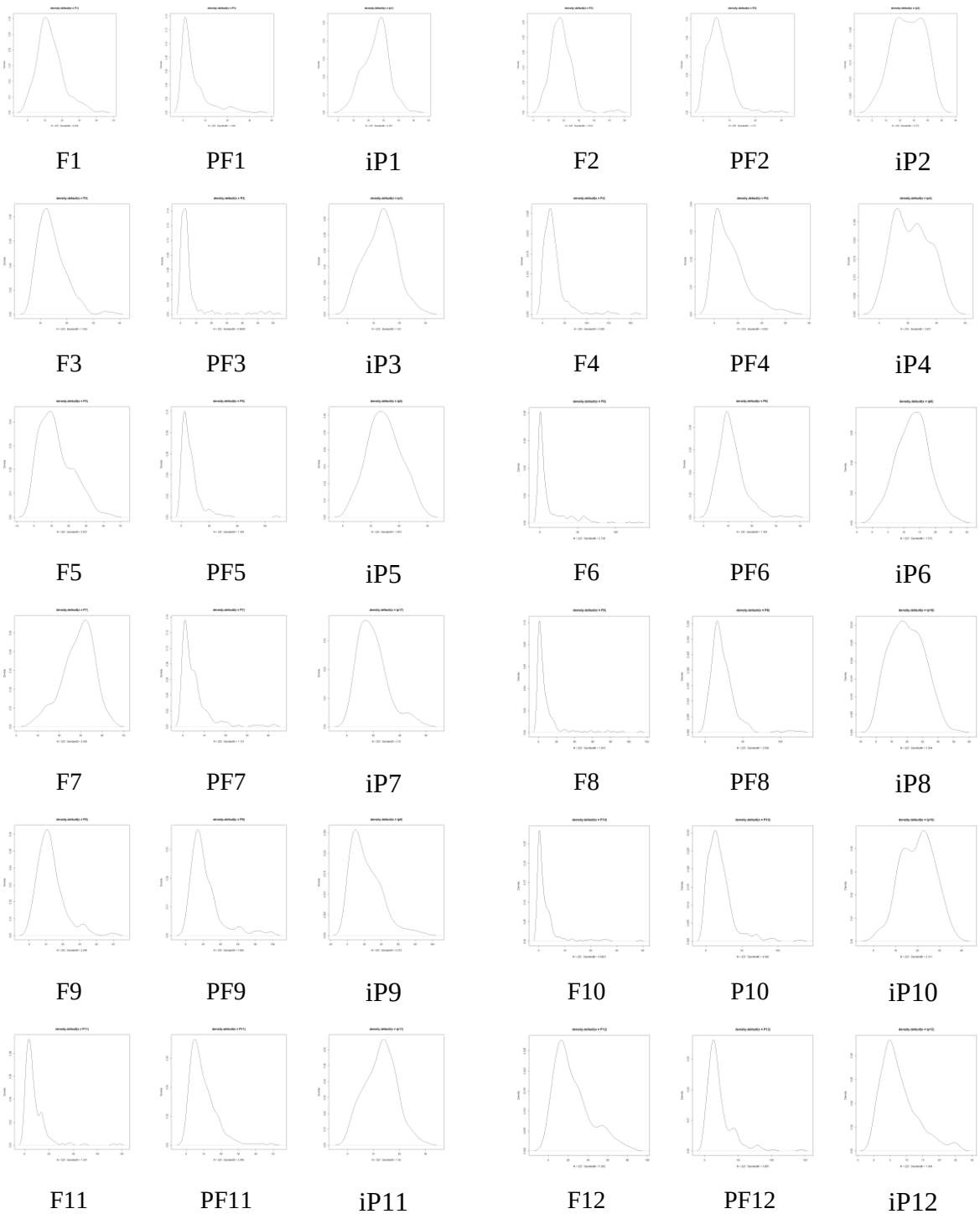

Figure 5.11: The probability density function (PDF) for the genuine faces (F), the printed photo faces (PF) and the iPad displayed faces (iP)

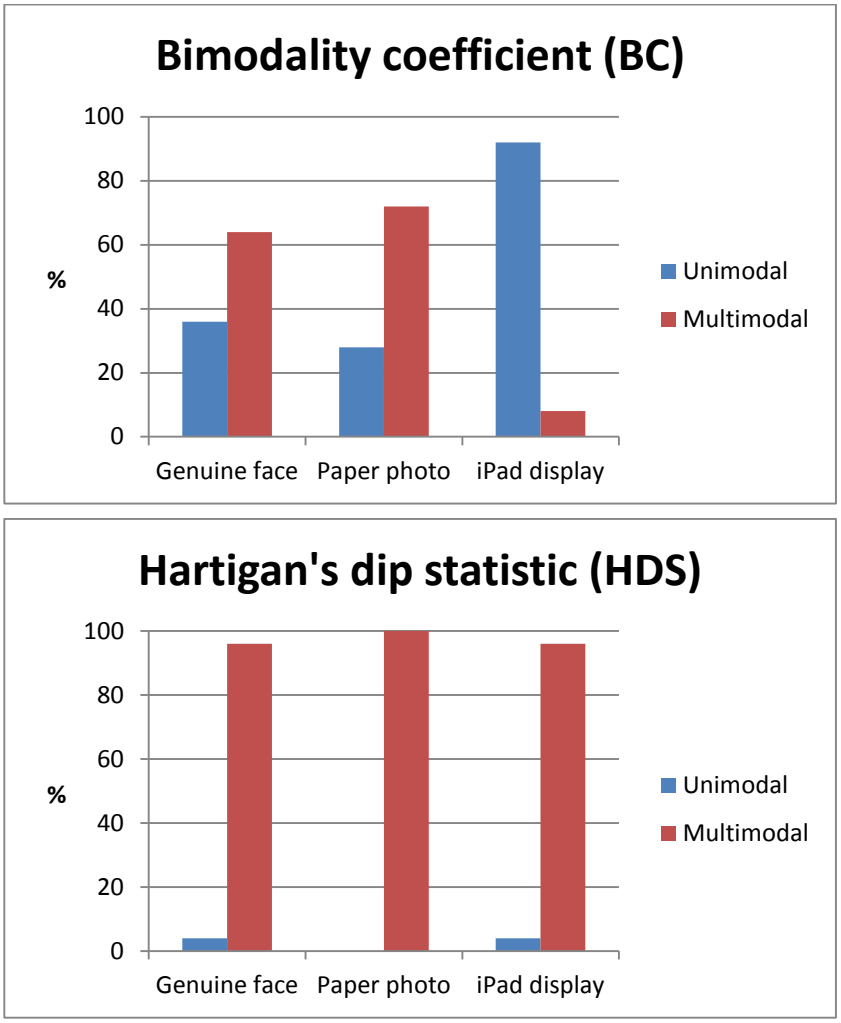

Figure 5.12: The distributions modality results from the BC and the HDS

The results of the modality analysis did not show any significant difference between the real faces and the fake traits. The results suggest that the modality of distributions could not be implemented as one of the classification parameters. The next section will discuss on the density of distribution mode for each distribution.

5.5.3 The density of distribution's mode

As been applied in Chapter 4, the density value of the I_{SDOLP} distribution mode may be useful in distinguishing between the real and fake faces. Mode is the most frequent number to appear in a set of distribution. From Figure 5.11, the highest peak in each distribution is the mode. By using this measure, the density value *f(x)* was obtained based on the mode. The results are illustrated in Figure 5.13. Data from Figure 5.13 indicate that no significant differences were found that may be used as a threshold to separate between the real faces, the printed photos and the iPad attacks. Thus, the density of distributions mode has also failed to separate the genuine trait from the fake traits.

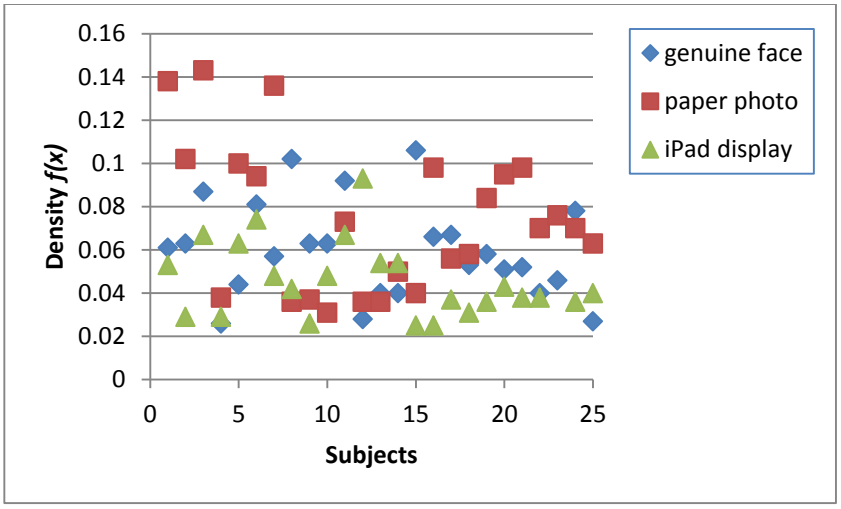

Figure 5.13: The density of the distributions mode

In the literature review, it was discussed that NIR light penetrates deeper into living tissue such as human skin [Jaminet (2015)]. Human skin also produces multi-reflections due to the multilayer structure. The effect of using polarised NIR light on genuine face, printed photo face and iPad displayed face is investigated in the next section based on the surface and subsurface NIR polarised images.

5.6 Surface and subsurface images

Surface and subsurface images can be obtained by using polarisation imaging system. In Chapter 4, visible polarised light was applied to capture the surface and subsurface images. The surface and subsurface images are known as S_1 and Img_{90}, respectively. However, no significant difference was found between the real faces and the printed photo faces based on the S_1 and Img_{90}. In contrast, S_1 and Img_{90} could be used differentiate between real face and iPad displayed face. In this chapter, similar approach was implemented but using NIR polarised images. Figure 5.14 presents images with surface reflection, S_1 and image with subsurface reflection, Img_{90} of a genuine subject, the printed photo and iPad displayed face.

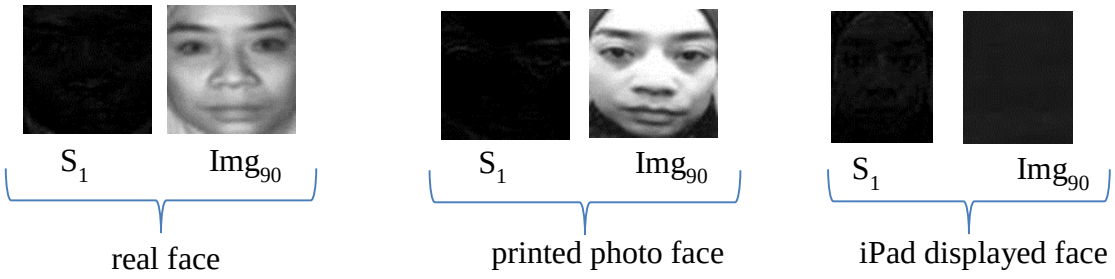

Figure 5.14: The surface, S_1 and subsurface, Img_{90} images

In Figure 5.14, there is no difference of the S_1 images between the real and fake faces. Similarly, Img_{90} of the genuine face and the printed photo face seemed similar to each other. In contrast, Img_{90} for the iPad faces are completely different than the Img_{90} for the real face. First comparison between the real and fake faces was statistically done on the S_1 and the results are presented in Figure 5.15. From the plot in Figure 5.15, it is apparent that the values of each measure are relatively similar amongst the real and fake faces. In addition, there is no value that could be used as a threshold to classify between the subjects. Due to low intensity values, no histogram could be generated for each S_1 distribution.

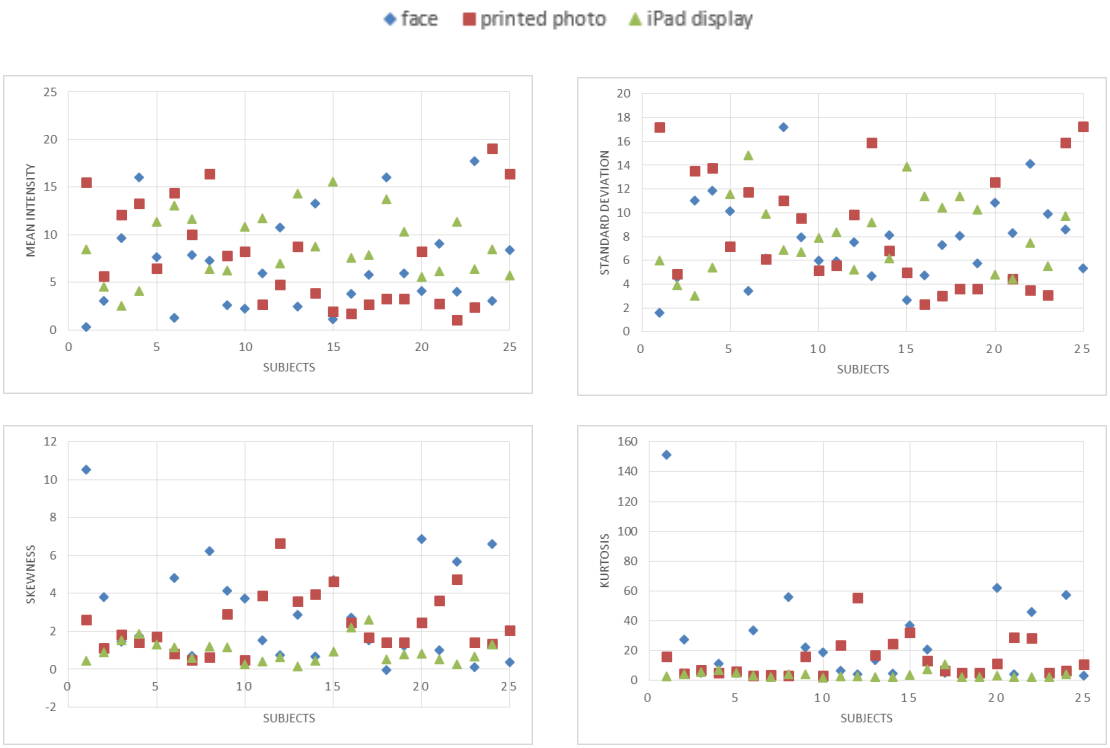

Figure 5.15: Statistical analysis on the NIR S_1 images for the real face, printed photo faces and iPad displayed faces

The next statistical analysis was carried out on the subsurface images. The subsurface images are images captured under polarisation angle of 90^0. As shown in Figure 5.14, Img_{90} for the real and printed photo faces seem similar to each other while the Img_{90} for the iPad displayed faces are completely different. Therefore, Img_{90} was statistically analysed in which the results are presented in Figure 5.16. The data in Figure 5.16 show that there are no significant differences found in each measure between the real faces and the printed photo faces. In contrast, the mean intensity and standard deviation of the iPad displayed faces show clear differences compared to the genuine faces. These results are consistent with the Img_{90} images shown in Figure 5.14. Driven by these results, the Img_{90} or subsurface images could be applied to detect iPad face attacks under NIR polarisation imaging system. The possible explanation for these results is discussed in the next section.

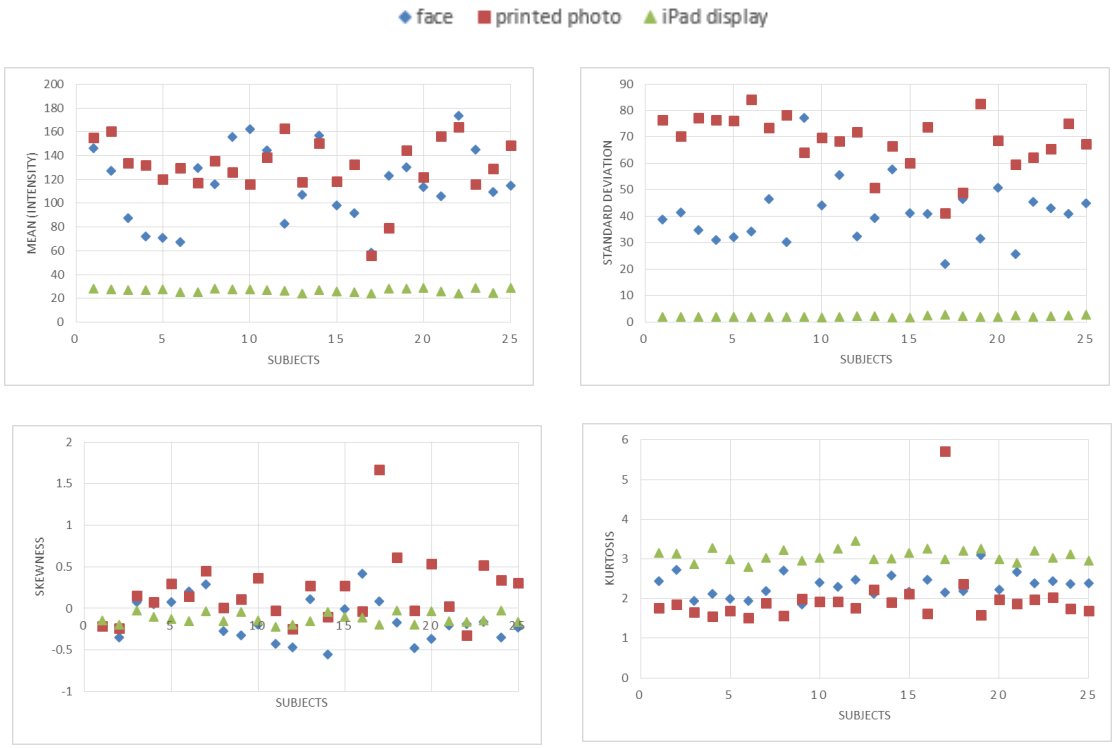

Figure 5.16: Statistical analysis on the NIR Img_{90} images for the real face, printed photo faces and iPad displayed faces

In the literature review, it has been explained in detail about the fundamentals of NIR light. The NIR wavelength range is between 750 to 1400 nm [Liew (n.d.)] compared to the visible light which is around 400 to 700 nm. Wavelength is the distance between peaks of the light waves as the light travels. Although the wavelength of the NIR light is longer than the visible light, the interaction of both lights with human skin remains similar. The NIR light that hits the skin surface is reflected, transmitted, scattered and re-emerged from inside the skin to the air surface. However, in the NIR spectrometry, human skin can be described constituting a six-layer structure: (1) stratum corneum; (2) living epidermis; (3) papillary dermis; (4) upper blood net dermis; (5) reticular dermis; and (6) deep blood net dermis [Nunez and Mendenhall (2008), Meglinski and Matcher (2002)]. Each layer transmits and reflects light according to the absorption coefficient. According to Henderson and Morries (2015), penetration of NIR through tissues is determined by several factors, for instance wavelength, energy, coherence and area of irradiance. In addition, the NIR wavelength can penetrate deeper into the tissue up to 1 mm [Shao et al. (2010)]. Contrary to the interaction between visible light and human skin, the interaction between NIR light with human skin is not affected by the skin chromophores,

such as haemoglobin, collagen and melanin inside the skin structure [Nunez and Mendenhall (2008)]. Thus, the amount of the chromophore can be ignored.

5.7 Conclusion

In Chapter 4, the SDOLP feature fusion formula (SDOLP3F) was introduced to differentiate between the genuine face and the paper photo captured using the visible light polarisation imaging system. The similar six individual measurers which were the mean, standard deviation, skewness, kurtosis, the BC and the density of distribution mode were examined. Measures with the accuracy rate more than 90% were then selected for the fusion formula. From the investigations, only two out of the six measures had the accuracy rates of more than 90%: standard deviation and the density of distribution mode. These two measures were formulated into a new fusion algorithm, the SDOLP3F. The accuracy rate for the SDOLP3F formula was found to be higher than the individual parameters.

Contrary to expectations, the study in this chapter did not find any significant difference between the genuine face and the printed photo faces that were recorded under NIR polarisation imaging system. Neither of the DOP and the Stokes parameters were able to distinguish between genuine and photo faces. These findings are rather disappointing. Further statistical observation on the surface and subsurface images also indicate that none of the measures were able to differentiate between real faces, printed photo faces and the iPad attacks. As expected, iPad attacks can be easily detected based on the Img_{90}.

The study in this chapter was designed to determine the effect of polarised single wavelength light source, such as the NIR light to the degree of polarisation of three different subjects: genuine face, printed photo face and iPad displayed face. The findings from the investigations suggest that in general, a single wavelength light could not be used to evaluate the degree of polarisation on each subject based on the two selected parameters: the DOP and the Stokes parameters. One of the significant findings to emerge from this study is that the different skin colours of the genuine faces could not be differentiated under polarised NIR light. As mentioned earlier, the haemoglobin, collagen and melanin in the skin layers do not give any effect to the penetration of NIR light [Nunez and Mendenhall (2008)]. This factor

explained the similarities of the NIR I_{SDOLP} amongst different skin colours. The second major finding was that the NIR penetrated deeper through a tissue sample and absorbed by the water density in the deep tissues. An implication of this is less or no subsurface reflection was produced. Taken together, although the study was based on a small sample of participants, it is recommended that the NIR images should be examined using other parameters than the DOP and the Stokes parameters since there was no polarised reflection under the NIR spectroscopy. In addition, the findings also suggest that the NIR is more suitable for a study involving biological deep tissues.

Proposed countermeasures against printed photo and iPad displayed attacks in Chapter 3, Chapter 4 and in Chapter 5 were mainly based on the polarised reflectance analysis. The degree of polarization (DOP) and the Stokes parameters were used to distinguish between a genuine face and fake traits. The printed photo faces and iPad displayed face were basically 2D facial spoofing attacks. However, when 3D mask was introduced as one of the spoofing attacks, some of the anti-spoofing techniques for 2D attacks were no longer relevant [Kose and Dugelay (2014)]. One of the publicly available 3D face mask database that was introduced is known as 3D Mask Attack Database (3DMAD). The images in the database were captured using a depth sensor, Microsoft Kinect for Xbox 360. However, questions were raised about the accuracy of the data generated by the sensor for depth image analysis. More information on the depth data accuracy of the 3D face images recorded using the Kinect for Xbox 360 would help researchers to establish a greater degree of accuracy on this matter. Hence, in the next chapter, an experimental study of different consumer depth sensors was carried out.

Chapter 6: An Evaluation of Depth Accuracy in Consumer Depth Sensors

6.1 Introduction

In 2D face recognition, photo faces and video representations are the most popular spoofing attacks due to the low cost and the availability of the validate user's photo which could be acquired using a digital device or downloaded from the internet [Chakka et al. (2011)]. There are various countermeasure techniques against face spoofing attacks that have been proposed. Other than the photo faces and video attacks, 2D face recognition systems are also vulnerable to 3D face mask attacks. According to Kose and Dugelay (2014), some of the countermeasure techniques that were developed against 2D spoofing attacks, are no longer relevant to counter the 3D face masks. To manufacture a 3D face mask, essential processes such as 3D reconstruction and 3D printing techniques are required. Equipment such as 3D scanner and 3D printer are usually used in the processes. The equipment are generally expensive. In addition, user cooperation is required during the 3D scan procedure which and handled by an expert. Due to these factors, the number of 3D spoofing face database is limited. One of the 3D masks databases is known as Morpho database developed by MORPHO[1] which consists of 207 real faces and 199 3D mask attack samples. The Morpho database is not publicly available.

Applications such as biometric, surveillance and robotics, low-cost technologies that can perform similar task as the expensive equipment are highly anticipated. For example, a depth sensor has become an alternative to replace 3D scanner because of the cheaper price and can be easily obtained online or from shops. Erdogmus and Marcel (2013) developed a 3D spoofing database known as the 3D Mask Attack Database (3DMAD) which was recorded using a depth sensor called Microsoft Kinect for Xbox 360. The depth images available in the 3DMAD database were used to differentiate between real and fake faces in several studies [Erdogmus and Marcel (2013), Erdogmus and Marcel (2014)]. One of these studies shows that

[1] http://www.morpho.com

images from the 3DMAD pose a serious threat to 2D face recognition systems, however, LBP has been able to eliminate 3D attacks [Erdogmus and Marcel (2013)]. The LBP anti-spoofing technique was proposed based on the depth images captured by the Kinect for Xbox 360 depth sensor.

There are several versions of depth sensors introduced by different consumers. In 2010, Microsoft launched the Kinect for Xbox 360 which was primarily designed for natural user interface (NUI) in a computer game environment [Khoshelham (2011)]. In 2011, Asus launched its very own depth sensor called Xtion Pro Live[2], the world's first and exclusive professional personal computer (PC) motion sensing development solution. Later in 2012, Microsoft introduced the second generation of Kinect sensor called the Kinect for Windows, which was developed to enable users to connect the sensor to a PC in order to get better depth information compared to the Kinect for Xbox 360 version. Recently in 2014, the latest version of Kinect sensor was launched by Microsoft known as Kinect for Windows version 2 (v2). In this study, the depth accuracy was compared between three depth sensors: Microsoft Kinect for Xbox 360, Microsoft Kinect for Windows v2 and Asus Xtion Pro Live.

Figure 6.1 presents three depth sensors that were used in the experiments throughout this chapter. As can be seen in Figure 6.1, each of the depth sensors has three main elements. One is the IR (infra-red) projector, second is the IR camera and the other is the RGB camera. For the Microsoft Kinect for Windows v2, there is one extra element added, which is the microphone located at the bottom part of the sensor. The microphone allows sound to be recorded with the images.

[2] http://www.asus.com/3D-Sensor/Xtion_PRO_LIVE

Microsoft Kinect for Xbox 360

Microsoft for Windows version 2

Asus Xtion Pro Live

Figure 6.1: Different versions of depth sensors

Due to the affordable price and easy installation, depth sensor was chosen to develop a face spoofing database known as 3D Mask Attack Database (3DMAD) [Erdogmus and Marcel (2013)]. The 3DMAD is the first public database available and each image in the database was captured using Microsoft Kinect for Xbox 360. With the availability of the 3D face spoofing database instigated more researchers from various fields to exploit the images in 3DMAD for further analysis. Therefore, the accuracy of the depth image is doubtful. Since depth data captured by Kinect depth sensor have been used widely in various research areas, such as face biometrics and 3D object reconstruction [Erdogmus and Marcel (2014), Chen et al. (2013)], questions were raised about the depth pixels stability generated by the Kinect depth sensor.

Several studies have been reported on the accuracy of depth pixels generated only by Kinect for Xbox 360. For instances, a number of authors have reported on the analyses of the depth data accuracy acquired by the Kinect for Xbox 360 sensor [Khoshelham (2011), Andersen et al. (2012)]. Other than that, a study by Macknojia et al. (2012) examined the characteristics between two versions of Kinect sensors: the Kinect for Xbox 360 and the Kinect for Windows. The results show that the best functional object-distance for both sensors was up to 2000 mm. Besides these two depth sensors, there is another depth sensor that was introduced by different company known as the ASUS Xtion Pro Live. Moreover, Microsoft has launched the latest version of Kinect named as the Kinect for Windows v2.

Insufficient information on the accuracy of a depth image acquired by different versions of depth sensors has led this study to be carried out. More information on this matter would help researchers to establish a greater degree of accuracy on the images. The main concern is on the depth image accuracy acquired from the Kinect for Xbox 360 device in the 3DMAD database introduced by Erdogmus and Marcel (2013). The 3DMAD database has been used in several studies on spoofing attacks against face biometric systems [Erdogmus and Marcel (2013), Erdogmus and Marcel (2014)].

Hence, in this chapter, experimental studies were carried out to examine pixels fluctuation in depth images captured by three depth sensors: the Kinect for Xbox 360, the Kinect for Windows v2 and the ASUS Xtion Pro Live.

6.2 Mathematical Model for Depth Estimation

The depth sensors capture depth and colour images simultaneously at a frame rate of 30 fps. Each sensor measures the depth with the help of an infrared projector and an infrared camera. The measurement of depth has been described as a triangulation process by [Freedman et al. (2012)]. Each of the elements in the sensors has its own function. The IR projector projects a pattern of IR light speckles on the scene. Since IR spectrum is invisible to human eye, the dots could not be seen. The IR camera captures the red dots pattern while the RGB camera captures coloured images. The captured pattern is correlated against a reference pattern which is obtained by recording a plane at a known distance from the depth sensor. The

reference pattern is stored in the memory of the sensor. Figure 6.2 illustrates the relationship between the distance of an object point P to the sensor comparative to a reference plane and the measured disparity d.

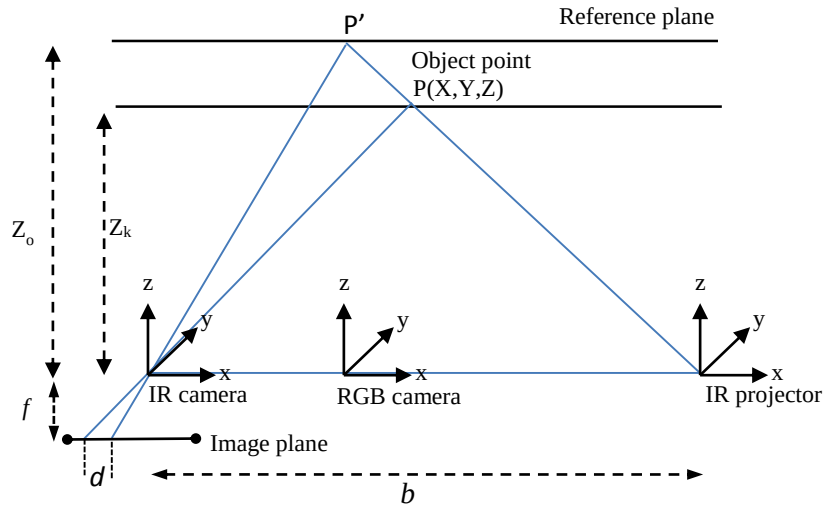

Figure 6.2: Depth and disparity relationship used for depth estimation

6.3 Experiments and Results

Experiments were carried out to evaluate the pixels fluctuation for a Kinect for Xbox 360, a Kinect for Windows v2 and an Asus Xtion Prolive. The results between the three sensors were then analyzed and compared. OpenNI was used to capture the data from the Kinect for Xbox 360 and the Asus Xtion Prolive. The depth data generated by Kinect for Windows v2 was examined by using the Microsoft SDK. The following sections discuss the experiment setup, the selection of the depth pixels and the measurement used to evaluate the pixels fluctuation.

a) Experiment setup

To measure the pixels' stability of the three depth sensors, the recording process was carried out in a room without the presence of anyone. The condition of the room was controlled

with all doors and windows closed to avoid any disturbances such as the wind and sound. The experiment setup used for the recording processes is presented in Figure 6.3, which shows that the depth sensor was pointed towards a planar surface, a wall. A rectangular box size 512 x 424 pixels was placed on a table in front of the wall. At first, the Kinect for Xbox 360 sensor was positioned in front of the wall. The distance between the sensor and the box was initially set to 800 mm. This distance was based on the suggested distance, between 0.8m and 3.5m [Kinect for Windows (2014)]. The sensor was removed away from the box repeatedly between 800mm to 3000mm, with a step size of 550mm. Therefore, the recording was done at five different distances: 800mm, 1350mm, 1900mm, 2450mm and 3000mm. At each distance, recording was carried out for 60 seconds. Once the depth video of the box was recorded, the similar processes were repeated for the next two sensors, the Kinect for Windows v2 and the ASUS Xtion Pro Live. As mentioned earlier, each video was recorded for duration of 60 seconds at each distance; depth sensor captured 30 frames per second resulted in 1800 frames in total per distance for each sensor.

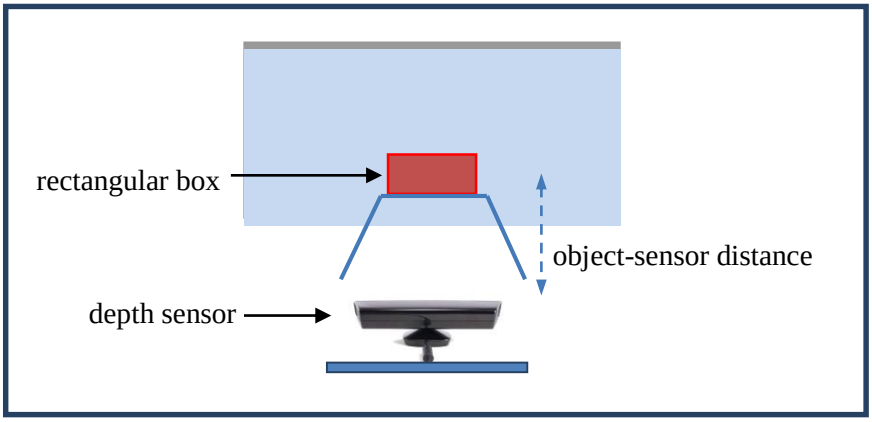

Figure 6.3: The experiment setup

Figure 6.4 presents an average scene over 1800 frames from a recording where the depth sensor was pointed directly at a rectangular box. The sensor was located at five different distances from the box: 800mm, 1350mm, 1900mm, 2400mm and 3000mm. The edges of the rectangular box are straight lines; however, as can be seen from the images in Figure 6.4, the sensor introduces noise to the edges. In addition, it can also be seen from the scene that the noise appears mostly at the edges of the object, such as at the edges between the ceiling and the wall. The depth pixels in the rectangular box could have behaved differently. Some of the

pixels might have small fluctuation and the others with a large error in terms of depth distances. Therefore, to measure the depth data flexibility, several pixels have been randomly selected. The next section of this study explains the methods in selecting pixels for fluctuation analysis.

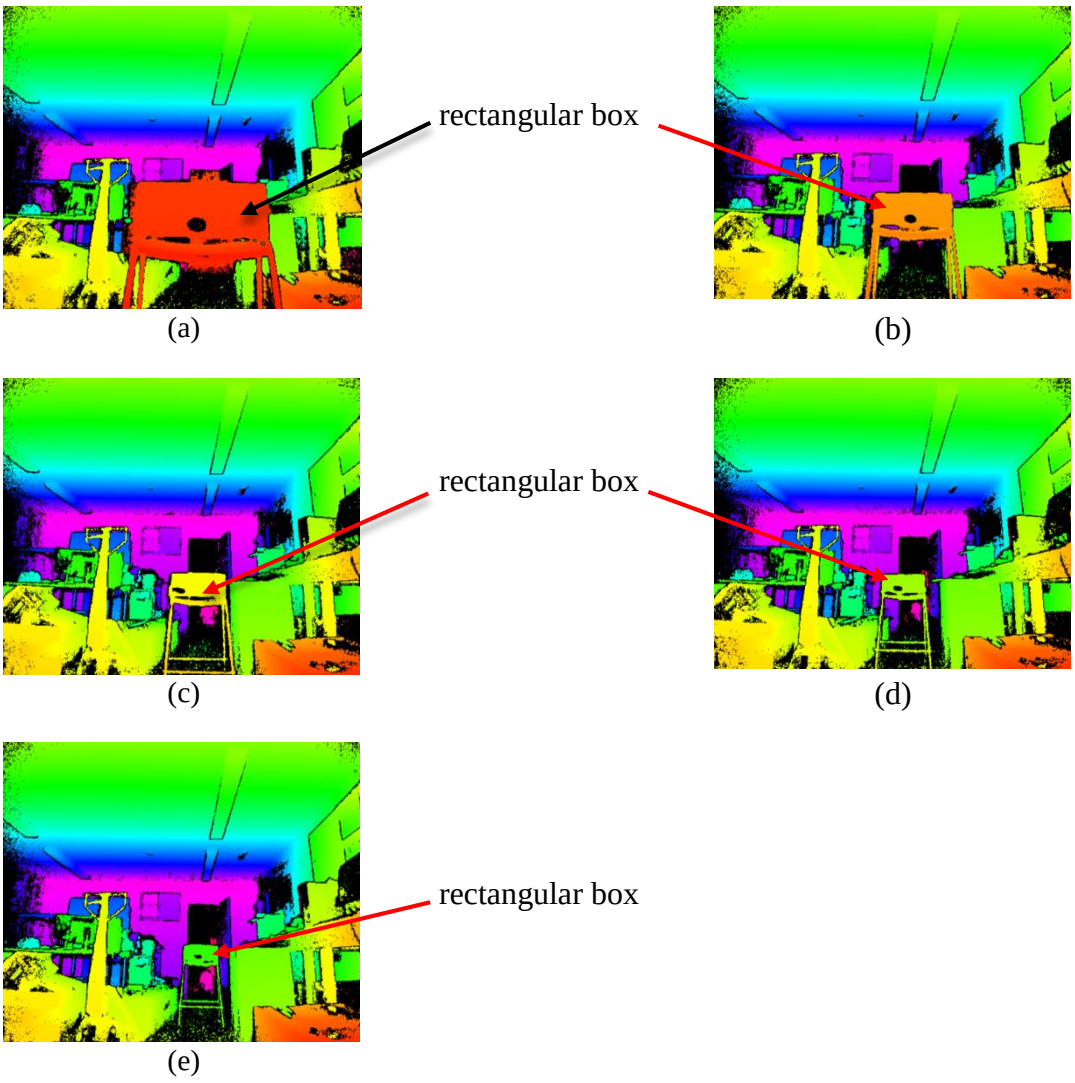

Figure 6.4: The colour depth images of a rectangular box recorded at five different object-sensor distances: (a) 800mm, (b) 1350mm, (c) 1900mm, (d) 2400mm and (e) 3000mm

b) Selection of pixels

As pointed out in the previous section, the depth sensor was placed facing a box as an object at five different object-sensor distances in an empty room. Depth image of the box was recorded for a duration of 60 seconds at each distance. In order to understand the fluctuation of depth pixel, twelve pixels were selected within the box area. Although the pixels were randomly selected, two patterns in selecting those pixels were introduced. Firstly, six pixels were chosen within the centre of the target area based on a circle pattern as illustrated in Figure 6.5. The target area was divided to four parts vertically: a, b, c and d; the area was also split to five horizontal parts labelled as e, f, g, h, and i. As can be seen in Figure 6.5, six pixels located approximately at the meeting points for the two parts were selected. The pixels were denoted as px_1, px_2, px_3, px_4, px_5 and px_6.

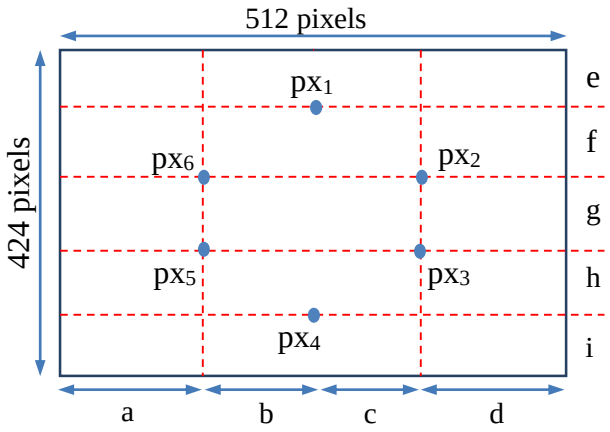

Figure 6.5: Six randomly selected pixels within the box

Secondly, four more pixels located at the vertices of the target area were selected. These pixels were labelled as px_7, px_8, px_9 and px_{10}. In addition, two additional pixels denoted as px_{11} and px_{12} were randomly chosen in between the midpoint and pixel px_8. The positions of the six pixels are presented in Figure 6.6. The pixel selection process was repeated for each video captured at five different wall-sensor distances. Once the pixels were selected, the pixels' fluctuation was measured as explained in the next section.

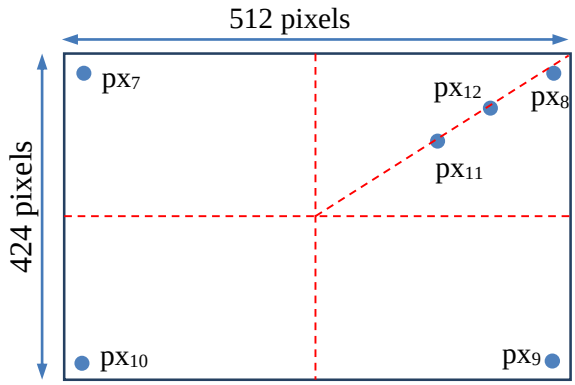

Figure 6.6: Pixels located at the edge of the box, px_7, px_8, px_9 and px_{10}, and two randomly selected pixels px_{11} and px_{12}

c) Pixels fluctuation measurement

For the purpose of pixel fluctuation measurement, the raw distance data recorded by the depth sensor need to be converted to real world distance unit, for example in meters (m), centimetres (cm) or millimetres (mm). The OpenNI framework, an open source Software Development Kit (SDK), was used for development of programming to access the depth data provided by Kinect for Xbox 360 and ASUS Xtion Pro Live sensors. To convert the depth data captured by Kinect for Windows v2 sensor, a Microsoft SDK with application programming interfaces (APIs) and device interfaces which supports applications on Windows computer was used. The depth distance was converted to real world distance in unit millimetres (mm) and saved in the database. To visualize the real distance of a pixel within the 60 seconds recording time, the distance in mm was plotted in graphs. For instance, Figure 6.7 illustrates the distance in mm of pixel px_1 at different object-sensor distances recorded by the three depth sensors. The y-scale for each graph in the same object-sensor distance was scaled at same value for comparison purposes.

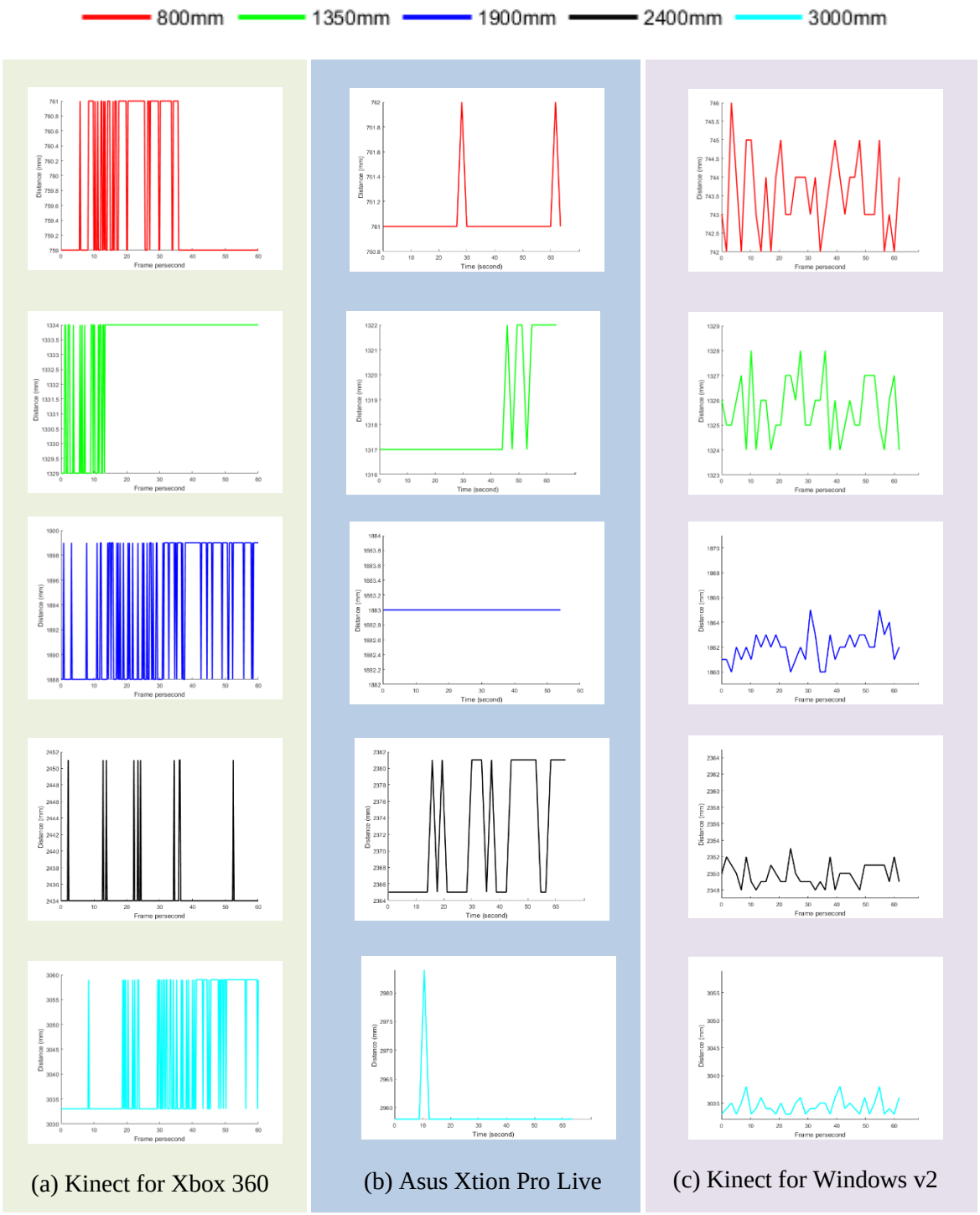

(a) Kinect for Xbox 360 (b) Asus Xtion Pro Live (c) Kinect for Windows v2

Figure 6.7: Pixel px_1 fluctuation in five different distances captured by different depth sensors

In Figure 6.7(a), fluctuations of px_1 was recorded using Kinect for Xbox 360 sensor. Figure 6.7(b) and Figure 6.7(c) illustrate the fluctuations of px_1 captured by Asus Xtion Pro Live and Kinect for Windows v2, respectively. The comparison is presented between the three depth sensors and five different object-sensor distances. From the graphs in Figure 6.7, the px_1 fluctuations for Kinect for Windows v2 are relatively similar in all five object-sensor distances. In each distance, the fluctuations of px_1 is within 4-5mm. In contrast, the fluctuation of px_1 recorded by Kinect for Xbox 360 sensor is 2mm at the distance of 800mm, but the fluctuations began to increase when the sensor was moved further away from the object. The Asus Xtion Pro Live sensor presents similar px_1 fluctuations pattern as the Kinect for Xbox 360 sensor. As depicted in Figure 6.7(b), the stability of px_1 starts to change as the sensor was moved away over 200mm from the object.

From the graph in Figure 6.7(c), it is apparent that the fluctuations of px_1 at each distance were very minimal. Since there were six pixels within the centre area of the box as shown in Figure 6.5, the processes of converting the depth distance of px_2, px_3, px_4, px_5 and px_6 to real distances in mm were repeated. Similarly, the distances in mm were then visualized and compared among the depth sensors in the form graphs. From the results, px_2, px_3, px_4, px_5 and px_6 pixels show similar fluctuation patterns as the px_1 at each distance. To further demonstrate the pixel fluctuation, the average fluctuations of each pixel is graphically shown in Figure 6.8.

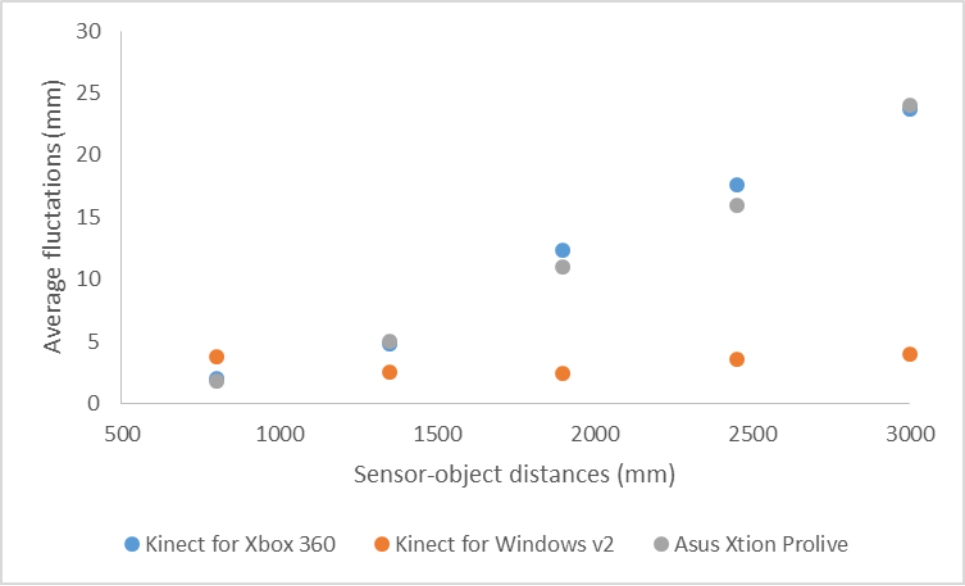

Figure 6.8: The average fluctuations of px_1, px_2, px_3, px_4, px_5 and px_6 at five distances

The results, as shown in Figure 6.8, indicate that Kinect for Windows v2 is the most stable depth sensor compared to the Kinect for Xbox 360 and ASUS Xtion Pro Live sensors. On average, px_1, px_2, px_3, px_4, px_5 and px_6 of Kinect for Windows v2 were shown to have less than 5 mm fluctuations at all distances. In contrast, similar pixels of Kinect for Xbox 360 and ASUS Xtion Pro Live show a clear trend of fluctuation increasing in line with the addition of the object-sensor distances.

Next, the same analysis was carried out for the other six pixels located at the vertices of the object. The pixels were denoted as px_7, px_8, px_9, px_{10}, px_{11} and px_{12}. For comparison purposes, one pixel, p_8 was chosen to demonstrate the fluctuation differences between the depth sensors at five object-sensor distances. The depth data of p_8 were firstly converted to the real world distance in mm. Figure 6.9 shows the fluctuation of px_8 at five distances for the three depth sensors. As shown in Figure 6.9(a), px_8 was quite stable at the shortest distance with only 1mm fluctuations. However, the stability of px_1 was disrupted by the increasing of the object-sensor's distances. The largest recorded px_8 fluctuation value was 22mm when the sensor was placed 3000mm from the object.

Turning now to the behaviour of px_8 captured by the ASUS Xtion Pro Live sensor. In Figure 6.9(b), the fluctuations were stable at the shortest distance, 800mm. However, px_8 started to fluctuate when the object-sensor distance increased to 1350mm to 3000 mm. In Figure 6.9(c), px_8 recorded by the Kinect for Windows v2 fluctuates in small value range for all distances. The px_8 fluctuation patterns between 800mm, 1350mm and 1900mm seem relatively similar with average fluctuations of 5mm. At the longer distances of 2400mm and 3000mm, px_8 seems quite stable with low fluctuation values. Taken together, these results suggest that there is an association between a depth-sensor, an object-sensor distance and the position of a selected pixel in producing the pixel stability during the recording process. Further discussions and conclusion are presented in the following section.

Figure 6.9: px_8 fluctuation in five different distances captured by the depth sensors

6.4 Conclusion

In this chapter, the study was designed to determine the effect of object-sensor distance to the stability of pixels in an object recorded by three different depth sensors namely as Kinect for Xbox 360, ASUS Xtion Pro Live and Kinect for Windows v2. A rectangular box was used as an object placed on a table in front of a wall in a controlled room. The depth sensors were mounted in front of the box at five different distances from 800 mm to 3000 mm, one at a time. The image of the box was recorded for 60 seconds in each session. Six pixels located at the middle area of the box and the other six pixels around the box vertices were selected to be examined. Erdogmus and Marcel (2013) introduced the 3DMAD database which was recorded by using the Kinect for Xbox 360 device. However, the object-sensor distance was not stated in their study. Thus, the stability of the pixels within the real face and the face mask detailed in their study can be debated. In relation to this, the findings in this chapter confirms that:

1. The ideal working distance for the Kinect Xbox 360 is less than 1500 mm.

2. It was also found that the instability of the depth distance of the pixels occurs nearer to the edges of an object.

3. Pixel's fluctuation recorded by the Kinect for Xbox 360 and the ASUS Xtion Pro Live became coarser as the distance increased. In contrast, the fluctuation of similar depth pixel acquired from the Kinect for Windows v2 sensor remained at the same fluctuation rate although the object-sensor increased in distance.

This is the first study to report the differences of depth pixel accuracy between three different depth sensors. Despite the object-sensor distance and the pixel location factors, the findings in this study provide a new understanding that the accuracy of the depth images is dependent on the sensors used. The following conclusions can be drawn from the results in this study:

1. The position of the depth pixels contributed to the depth measurements during the recording by the three depth sensors. Pixel located within the centre area of an object had less fluctuation compared to the pixel at the edge of the similar object.

2. The Kinect for Windows v2 device is suggested as the most stable device able to produce minimum depth pixel fluctuation for depth image analysis.

3. Although the Kinect for Windows v2 produces the most stable depth pixels among the other two sensors, however, none of these sensors were suitable for 3D face reconstruction for the purpose of spoofing face detection according to the potential errors made by the fluctuated pixels.

As mentioned in Section 6.1, Microsoft Kinect for Xbox 360 was used to record images in the 3DMAD spoofing database. The 3DMAD was used in several studies to detect spoofing face attacks in face recognition systems. In the recording process of the 3DMAD, Erdogmus and Marcel (2013) did not mention the distance between the subjects and the depth sensor. Meanwhile, from the investigations on pixel stability that was carried out in Section 6.3, the results showed that Kinect for Xbox 360 sensor did not produce stable depth pixels with fluctuations value up to 20mm for the largest object-sensor distance. Due to 20mm potential errors, the recording is not suitable for 3D face reconstruction for 3D and 2D face spoofing detection. From these findings, the accuracy depth images in the 3DMAD database is doubtful. Spoofing face detection methods against 3D face masks captured by Kinect for Xbox 360 as in the 3DMAD might suffer due to pixel inaccuracy.

Chapter 7: Conclusions

In this chapter, the findings with regard to the research questions are summarized and general conclusions based on the findings of the investigations presented in this thesis are described. Furthermore, the research contribution to knowledge is discussed as well as the limitations of this study. This chapter concludes with recommendation for future research.

7.1 Findings with regard to the research questions

7.1.1 Research question 1

What are the effects of using normal visible light in a polarisation imaging system in which a polariser is mounted only in front of the camera lens, to detect genuine and fake faces? (Chapter 3)

To answer this research question, two different types of lights were used in the experiments. One was fluorescent ceiling light and the other was a table light. A typical polarisation imaging system requires installation of polariser in front of each light source and also in front of the camera lens. In Chapter 3, no polariser was installed in front of lights in order to investigate the effect on the polarisation images. There were several results from the experiments. Firstly, the mean intensity of the I_{pol} images for all real and fake faces under both fluorescent ceiling and table lights were very small within the range value of 0.0029 to 0.1155. Similarly, there was no difference of the I_{SDOLP} images between the real and fake traits. Thus, the real face and the spoofing face could not be differentiated due to the similarities of the I_{pol} and I_{SDOLP} images. These findings indicate that normal (unpolarised) visible light could not be used in a polarisation imaging system to capture polarised images for the designated purpose.

7.1.2 Research question 2

What is the impact of using polarized visible light in a polarisation imaging system to separate between the surface and subsurface reflections as one of the classification methods between genuine face, printed photo paper and iPad displayed image? (Chapter 4)

Results of the experiments in Chapter 4 include the investigations to separate surface and subsurface reflections of each real and fake faces. An image that consists of only surface reflection was denoted as S_1 while an image that contains subsurface reflection was known as Img_{90}. In Figure 4.30, S_1 and Img_{90} for real face were significantly different. Although the intensity of S_1 for real face was low, it still displayed a clear texture of the face. These findings support that surface and subsurface reflections of human skin can be differentiated by using polarised light.

S_1 and Img_{90} for the printed photo face were also different from each other as shown in Figure 4.30. The S_1 was darker than the Img_{90}. However, S_1 for the printed photo face did not show significant texture of the photo face. Apart from that, S_1 for the iPad displayed face was completely different than the Img_{90}. The intensity of the Img_{90} for the iPad attack was very low while the S_1 shows high intensity value.

From the discussion in Section 4.5, printed photo face consisted multi-reflections due to the physical properties of the paper. S_1 and Img_{90} for the printed photo face represented surface and subsurface reflections, respectively. Meanwhile, iPad emitted its own polarised light thus no surface or subsurface reflection occurred. The intensity of the S_1 for the iPad image was the lights emitted by the iPad.

Further analysis was carried out by comparing S_1 and Img_{90} between the real face, printed photo and iPad displayed faces. The results indicated that iPad attacks can be easily detected by using both S_1 and Img_{90}. However, since real face and photo paper consisted similar reflection properties, S_1 and Img_{90} could not be applied as one of the classification methods between the two materials.

7.1.3 Research question 3

How do the polarised images correlate with the spoofing face detection performance in a face recognition system? (Chapter 4)

Polarised image is defined as an image captured under polarised lights. As explained in Section 3.2, polarised images used in this thesis were captured at four polarisation angles: 0^0, 45^0, 90^0 and 135^0. These polarised images were analysed based on two parameters: the degree of polarisation (DOP) and the Stokes parameters.

Polarised images of each real and fake traits were processed to create new images denoted as I_{pol} and I_{SDOLP} which represent polarisation image and Stokes degree of linear polarisation image, respectively. The I_{pol} intensity values indicated the portion of the reflected light that was perfectly polarized compared to the total intensity of the reflected light. The results from the investigations showed that the I_{pol} images of the real and the fake faces had low intensity values with small differences between them.

Meanwhile, the intensity of the I_{SDOLP} images of the iPad displayed faces was much higher than the I_{SDOLP} of the real faces. Furthermore, the intensity differences of the I_{SDOLP} between real faces and photo papers were also significant. Besides the intensity of the images, other analysis such as the standard deviation, the skewness, the kurtosis, the modality of the I_{SDOLP} data distribution and the density of the distribution mode were carried out. For better detection accuracy rate, two of the measures with highest detection accuracy rates were selected to be fused in a newly proposed algorithm named as SDOLP3F. The detection accuracy rate of the SDOLP3F formula increased to 93.9% compared to the individual measures.

To answer research question 3, the use of polarised image could contribute to enhance the performance of face recognition system against spoofing face attacks. The proposed fusion formula, SDOLP3F of the I_{SDOLP} achieved higher detection accuracy rate. However, I_{pol} could not be used to detect spoofing faces due to the ratio of polarised reflected light to the total reflected light was very small and close between each materials.

7.1.4 Research question 4

What are the effects of implementing polarized near infrared (NIR) light in the polarization imaging system on polarization images between genuine faces and non-genuine traits? (Chapter 5)

From the experiments results presented in Chapter 5, the I_{pol} and I_{SDOLP} of genuine face, printed photo paper and iPad displayed face which were captured under NIR light polarization imaging system, did not provide significant differences that could be used to differentiate between them. However, there were slight differences of the skewness and kurtosis values of I_{SDOLP} between real faces and iPad display images. One of the reasons behind these findings was the deep penetration of NIR light into skin tissues and paper. In contrast, iPad emits its own polarized light thus no penetration of the NIR light occurred.

7.1.5 Research question 5

What is the relationship between multiple versions of depth sensors and the sensor-subject distances with the fluctuations of centre depth pixels and pixels at the edges of the subject? (Chapter 6)

The findings from the investigations in Chapter 6 suggest that the Kinect for Windows v2 was the most stable depth sensor compared to the Kinect for Xbox 360 and ASUS Xtion Pro Live sensors. The Kinect for Windows v2 produced the average centre depth pixels fluctuations less than 5mm at object-sensor distances up to 3m. However, the fluctuations of the centre depth pixels captured by the Kinect for Xbox 360 and ASUS Xtion Pro Live sensors had escalated with the increase of the object-sensor distances. In the analysis of the stability of pixels at the edges of the subject, the results showed that these pixels were significantly not stable at any object-sensor distances captured by the three depth sensors. However, none of these sensors were suitable for 3D face reconstruction for the purpose of spoofing face detection according to the potential errors made by the fluctuated pixels.

7.2 Research contribution to knowledge

The main contribution to knowledge in this thesis is the application of the polarisation imaging system to detect fake faces in face recognition system without going through a classification algorithm. The polarised reflection was able to differentiate between real face, photo paper and iPad attacks. This technique is assumed to work well in detecting other types of face spoofing attacks such as 3D face mask. As a record, the polarisation imaging technique has never been applied in previous studies of face spoofing detection. By using the proposed polarisation imaging technique, polarized images of the real faces and the fake traits were captured and analysed. The results have led to contributions to knowledge as listed:

1. The reflected light from the genuine face, photo paper and iPad displayed face is not polarised according to very low intensity values of the I_{pol} images.

2. The newly proposed fusion formula, SDOLP3F achieved highest spoofing face detection accuracy rate compared to individual measures between the I_{SDOLP} images of the real face and printed photo face. However, the mean and standard deviation measures for the I_{pol} and I_{SDOLP} can also be used to differentiate between real and photo faces due to the high accuracy rates.

3. The iPad or portable LCD screen spoofing attacks could be easily detected by using polarised images captured at polarisation angle that is perpendicular to the direction of polarised light wave emitted by the iPad or LCD devices. Polarised image is an image captured by polarised light at different polarisation angles. In this study, 90^0 polarisation angle was the angle perpendicular to the direction of polarised light wave from the iPad. Thus, the distinguishable polarised image was labelled as Img_{90}. In addition, iPad spoofing face can be statistically eliminated by I_{pol} and I_{SDOLP} images.

4. The I_{SDOLP} data distributions between the genuine black skin faces and their printed photo were very similar in which the black genuine faces have been erroneously identified as photo attacks. By using the bimodality coefficient (BC) algorithm, this problem could be resolved.

7.3 Research limitations

Several limitations to this study need to be acknowledged. The limitations are listed as:

1. The first limitation is the small sample size with only 37 participants. Since there was no polarisation image database, the polarisation images in this study were self-collected. The participants were randomly selected among the members of the faculty on a voluntary basis.

2. The types of face spoofing attacks were restricted to printed photo paper and iPad displayed faces due to cost factor. It is expensive to get 3D face masks made of various materials such as latex, silicon or rubber which mimic the real face of the participants.

3. The third limitation is the lack of experimental equipment that caused the angles of polariser in front of the camera lens to be manually changed.

7.4 Conclusion and future work

The main aim of this research was to reduce spoofing impact on 2D face recognition systems. Looking at the research questions posed at the beginning of this study, it is now possible to state that the visible polarisation imaging technique that was tested on printed photo and iPad spoofing faces, was able to detect these 2D spoofing attacks in 2D face recognition systems.

In contrast, NIR polarisation imaging system showed negative detection results, which suggest that the NIR light should not be used in a polarisation imaging system for spoofing face detection. On the other hand, the appearance of 3D face mask attacks on both 2D and 3D face recognition systems has triggered concern amongst the biometric community. Several 3D mask databases were created for research purposes. One of the databases is the 3DMAD in which the images were captured using Microsoft Kinect depth sensor. The stability of the depth pixels became an issue. Thus, part of the studies in this thesis was directed to investigate the fluctuations of the depth pixels among several types of cost effective depth sensors. The findings suggest the ideal object-sensor distances and the best depth sensor with less pixels fluctuation which could be a clue for an upcoming study.

More research is required to determine the efficacy of the polarisation imaging technique to reduce spoofing attacks in face recognition performances. Therefore, a list of future work is suggested as follows:

1. Further investigations should be continued on larger sample size with variety of skin colours and age groups. Besides investigation on spoofing face detection, it would be interesting to assess the abilities of polarisation methods in separating human skin colours and classifying different age groups.

2. 3D face mask is another types of spoofing attacks to a face recognition system. A 3D face mask is expensive and high cost is needed to produce 3D masks for each subject in a spoofing database. Since 3D Mask Attack Database (3DMAD) which was developed by Idiap Research Institute, consists of seventeen 3D face masks, a research collaboration with the institute is therefore recommended. A 3D polarised spoofing dataset can be recorded by using the existing 3D face masks, hence the efficacy of the SDOLP3F algorithm can be tested.

3. Experiments in this thesis were carried out in indoor lighting controlled environment. In real world application, face recognition system is usually installed for security purposes such as in a building or an airport. The proposed polarisation imaging technique should also be tested in a real world face recognition system. Any opportunity of collaboration with existing security face recognition system, is suggested.

4. Apart from the reflectance based analysis, further study can be carried out by analysing the texture of I_{SDOLP} and I_{DOP} images. Then, spoofing face detection accuracy of the newly proposed SDOLP3F algorithm can be tested.

References

Xtion PRO LIVE. Online at https://www.asus.com/3D-Sensor/Xtion_PRO_LIVE/, accessed 10 March 2015.

(2014) *Kinect for Windows.* Online at http://www.microsoft.com/en-us/kinectforwindows, accessed 10 March 2015.

Akaike, H.,"Akaike's information criterion," in *International Encyclopedia of Statistical Science*: Springer, 2011, pp. 25-25.

Akhtar, Z. & Foresti, G. L., (2016). Face Spoof Attack Recognition Using Discriminative Image Patches. *Journal of Electrical and Computer Engineering, vol.* 2016.

Ali, J., Wang, W., Zevallos, M. & Alfano, R., (2004). Near Infrared Spectroscopy and Imaging to Probe Differences in Water Content in Normal and Cancer Human Prostate Tissues. *Technology in cancer research & treatment, vol.* 3**,** pp**.** 491-497.

Almoussa, N., (2008). Variational retinex and shadow removal. *The Mathematics Department, UCLA, vol.*

Andersen, M. R., Jensen, T., Lisouski, P., Mortensen, A. K., Hansen, M. K., Gregersen, T. & Ahrendt, P., (2012). Kinect depth sensor evaluation for computer vision applications. *Electrical and Computer Engineering Technical Report ECE-TR-6, vol.*

Andrei, E. (n.d.) *Fresnel's Equations for Reflection and Refraction.* Online at http://www.physics.rutgers.edu/ugrad/389/FresnelsEqns.ppt, accessed 17 April 2017.

Ashish. (2016) *Why Does The Sun Reflect Off Seas And Oceans?* Online at https://www.scienceabc.com/nature/why-does-the-sun-reflect-off-seas-and-oceans.html, accessed 25 May 2017.

Bae, E. J., Seo, S. H., Kye, Y. C. & Ahn, H. H., (2010). A Quantitative Assessment of the Human Skin Surface using Polarized Light Digital Photography and its Dermatologic Significance. *Skin Research and Technology, vol.* 16**,** pp**.** 270-274.

Bagga, M. & Singh, B. (2016). Spoofing Detection in Face Recognition: A review, in: *3rd International Conference on Computing for Sustainable Global Development (INDIACom)*. March 16-18, 2016, New Delhi, India, pp. 2037-2042. IEEE.

Bakker, A., Smith, B., Ainslie, P. & Smith, K.,"Near-infrared spectroscopy," in *Applied Aspects of Ultrasonography in Humans*: InTech, 2012.

Bao, W., Li, H., Li, N. & Jiang, W. (2009). A Liveness Detection Method for Face Recognition Based on Optical Flow Field, in: *Image Analysis and Signal Processing, IASP*. April 11-12, 2009, Linhai, China, pp. 233-236. IEEE.

Bay, H., Ess, A., Tuytelaars, T. & Van Gool, L., (2008). Speeded-up robust features (SURF). *Computer vision and image understanding, vol.* 110**,** pp**.** 346-359.

Biggio, B., Akhtar, Z., Fumera, G., Marcialis, G. L. & Roli, F., (2012). Security Evaluation of Biometric Authentication Systems under Real Spoofing Attacks. *IET Biometrics, vol.* 1**,** pp**.** 11-24.

Bin, Z., Jianhua, X., Hongzhi, Z., Chepko, G. J., Freedman, M. T. & Kevin Yingyin, Z. (2007). Polarization Imaging for Breast Cancer Diagnosis using Texture Analysis and SVM, in: *Life Science Systems and Applications Workshop, LISA*. Nov 8-9, 2007, Bethesda, MD, USA, pp. 217-220. IEEE.

Boulkenafet, Z., Komulainen, J. & Hadid, A. (2015). Face Anti-spoofing Based on Color Texture Analysis, in: *Image Processing (ICIP)*. Sept. 27-30, 2015, Quebec City, Canada, pp. 2636-2640. IEEE.

Britannica, T. E. o. E. (2007) *Paper*. Online at https://www.britannica.com/technology/paper, accessed 5 February 2017.

Britt, K. W. (2012) *Papermaking*. Online at https://www.britannica.com/topic/papermaking, accessed 5 February 2017.

Brown, S. (2016) *Measures of Shape: Skewness and Kurtosis*. Online at https://brownmath.com/stat/shape.htm, accessed Feb 11 2017.

Chakka, M. M., Anjos, A., Marcel, S., Tronci, R., Muntoni, D., Fadda, G., Pili, M., Sirena, N., Murgia, G. & Ristori, M. (2011). Competition on Counter Measures to 2-D Facial Spoofing Attacks, in: *Biometrics (IJCB)*. Oct. 11-13, 2011, Washington, DC, USA, pp. 1-6. IEEE.

Chen, C., Zou, W. & Wang, J. (2013). 3D surface reconstruction based on Kinect, in: *2013 IEEE Third International Conference on Information Science and Technology (ICIST)*. 23-25 March 2013, 2013, pp. 986-990.

Chen, H., Lin, Z., Mo, L., Wu, T. & Tan, C., (2015). Near-infrared Spectroscopy as a Diagnostic Tool for Distinguishing between Normal and Malignant Colorectal Tissues. *BioMed research international, vol.* 2015.

Collett, E. (2005). Field guide to polarization, in. 2005, pp.: SPIE Bellingham, WA.

Davies, A. M. C. (n.d.) *An Introduction to Near Infrared (NIR) Spectrometry*. Online at https://www.impublications.com/content/introduction-near-infrared-nir-spectroscopy, accessed 10 January 2017.

Demos, S. G., Papadopoulos, A. J., Savage, H., Heerdt, A. S., Schantz, S. & Alfano, R. R., (1997). Polarization Filter for Biomedical Tissue Optical Imaging. *Photochemistry and Photobiology, vol.* 66**,** pp**.** 821-825.

Dryden, J. (2014) *Human eye can see 'invisible' infrared light.* Online at www.sciencedaily.com/releases/2014/12/141201161116.htm, accessed 3 February 2017.

Duffy, A. (2000) *Interference of Waves.* Online at http://physics.bu.edu/~duffy/py105/WaveInterference.html, accessed 20 January 2017.

Erdogmus, N. & Marcel, S. (2013). Spoofing in 2D Face Recognition with 3D Masks and Anti-spoofing with Kinect, in: *Biometrics: Theory, Applications and Systems (BTAS)*. Sept. 29 - Oct. 2, 2013, Arlington, VA, USA, pp. 1-6. IEEE.

Erdogmus, N. & Marcel, S., (2014). Spoofing Face Recognition With 3D Masks. *IEEE Transactions on Information Forensics and Security, vol.* 9**,** pp**.** 1084-1097.

Feng, L., Po, L.-M., Li, Y., Xu, X., Yuan, F., Cheung, T. C.-H. & Cheung, K.-W., (2016). Integration of image quality and motion cues for face anti-spoofing: A neural network approach. *Journal of Visual Communication and Image Representation, vol.* 38**,** pp**.** 451-460.

Freedman, B., Shpunt, A., Machline, M. & Arieli, Y. 2012. Depth mapping using projected patterns. Google Patents.

Freeman, J. B., Ambady, N., Rule, N. O. & Johnson, K. L., (2008). Will a category cue attract you? Motor output reveals dynamic competition across person construal. *Journal of Experimental Psychology: General, vol.* 137**,** pp**.** 673.

Freeman, J. B. & Dale, R., (2013). Assessing bimodality to detect the presence of a dual cognitive process. *Behavior research methods, vol.* 45**,** pp**.** 83-97.

Frischholz, R. W. & Werner, A. (2003). Avoiding Replay-attacks in a Face Recognition System using Head-pose Estimation, in: *Analysis and Modeling of Faces and Gestures, AMFG*. Oct. 17, 2003, Nice, France, pp. 234-235. IEEE.

Galbally, J., Marcel, S. & Fierrez, J., (2014). Biometric Antispoofing Methods: A Survey in Face Recognition. *IEEE Access, vol.* 2**,** pp**.** 1530-1552.

Ghassemi, P. & Miranbaygi, M. H., (2009). Towards Skin Polarization Characterization using Polarimetric Technique. *Journal of Zhejiang University-Science B, vol.* 10**,** pp**.** 602-608.

Hadid, A. (2014). Face Biometrics Under Spoofing Attacks: Vulnerabilities, Countermeasures, Open Issues, and Research Directions, in: *Computer Vision and Pattern Recognition Workshops (CVPRW)*. June 23-28, 2014, Columbus, OH, USA, pp. 113-118. IEEE.

Hanrahan, P. & Krueger, W. 1993. Reflection from Layered Surfaces Due to Subsurface Scattering. *Computer Graphics and Interactive Techniques.* Anaheim, CA: ACM.

Hartigan, J. A. & Hartigan, P., (1985). The Dip Test of Unimodality. *The Annals of Statistics, vol.***,** pp**.** 70-84.

Hébert, M. & Hersch, R. D., (2009). Reflectance and Transmittance Model for Recto-verso Halftone Prints: Spectral Predictions with Multi-ink Halftones. *JOSA A, vol.* 26**,** pp**.** 356-364.

Henderson, T. A. & Morries, L. D., (2015). Near-infrared photonic energy penetration: can infrared phototherapy effectively reach the human brain. *Neuropsychiatr Dis Treat, vol.* 11**,** pp**.** 2191-2208.

Hersch, R. D., Emmel, P., Collaud, F. & Crété, F., (2005). Spectral Reflection and Dot Surface Prediction Models for Color Halftone Prints. *Journal of Electronic Imaging, vol.* 14**,** pp**.** 033001-033001-12.

Hoffman, M. (2014) *Picture of the Skin.* Online at http://www.webmd.com/skin-problems-and-treatments/picture-of-the-skin#1, accessed 6 May 2017.

Hua, C. & Wolff, L. B. 1996. Polarization Phase-based Method for Material Classification and Object Recognition in Computer Vision. *Computer Vision and Pattern Recognition.* San Francisco, CA, USA: IEEE Computer Society Conference.

Huard, S. (1997). *Polarisation of Light*, New York: John Wiley & Sons.

Inhan, K., Juhyun, A. & Daijin, K. (2016). Face Spoofing Detection with Highlight Removal Effect and Distortions, in: *Systems, Man, and Cybernetics (SMC).* Oct. 9-12, 2016, Budapest, Hungary, pp. 004299-004304. IEEE.

Intelsat. (2013) *Circular Polarization vs. Linear Polarization* Online at http://www.intelsat.com/wp-content/uploads/2013/02/Polarization.pdf, accessed 5 Jan 2017.

Jacques, S. L. & Ramella-Roman, J. C., (2004). Polarized Light Imaging of Tissues. *Lasers and Current Optical Techniques in Biology, vol.***,** pp**.** 591-607.

Jacques, S. L., Ramella-Roman, J. C. & Lee, K., (2002). Imaging Skin Pathology with Polarized Light. *Journal of biomedical optics, vol.* 7**,** pp**.** 329-340.

Jacques, S. L., Roman, J. R. & Lee, K., (2000). Imaging Superficial Tissues with Polarized Light. *Lasers in surgery and medicine, vol.* 26**,** pp**.** 119-129.

Jain, A. K., Nandakumar, K. & Ross, A., (2016). 50 years of Biometric Research: Accomplishments, Challenges, and Opportunities. *Pattern Recognition Letters, vol.* 79**,** pp**.** 80-105.

Jain, A. K., Ross, A. & Prabhakar, S., (2004). An Introduction to Biometric Recognition. *IEEE Transactions on Circuits and Systems for Video Technology, vol.* 14**,** pp**.** 4-20.

Jaminet, P. (2015) *The Benefits of Near Infrared Light.* Online at http://perfecthealthdiet.com/2015/06/the-benefits-of-near-infrared-light/, accessed 13 January 2017.

Jee, H.-K., Jung, S.-U. & Yoo, J.-H., (2006). Liveness Detection for Embedded Face Recognition System. *International Journal of Biological and Medical Sciences, vol.* 1**,** pp**.** 235-238.

Kanzawa, Y., Kimura, Y. & Naito, T. (2011). Human Skin Detection by Visible and Near-infrared Imaging, in: *Machine Vision Applications (MVA)*. June 13-15, 2011, Nara, Japan, pp.: Citeseer.

Khoshelham, K. (2011). Accuracy Analysis of Kinect Depth Data, in: *ISPRS Workshop Laser Scanning*. August 29-31, 2011, Calgary, Alberta, pp. W12.

Kim, Y., Na, J., Yoon, S. & Yi, J., (2009). Masked Fake Face Detection using Radiance Measurements. *Journal of the Optical Society of America A, vol.* 26**,** pp**.** 760-766.

Kollias, N.,"Polarized Light Photography of Human Skin," in *Bioengineering of the Skin: Skin Surface Imaging and Analysis*, Klaus-P. Wilhelm, P. E., Enzo Berardesca, Howard I. Maibach, Eds., New York: CRC Press, 1996, pp. 384.

Kollreider, K., Fronthaler, H. & Bigun, J. (2005). Evaluating Liveness by Face Images and the Structure Tensor, in: *Automatic Identification Advanced Technologies*. Oct. 17-18, 2005, Buffalo, NY, USA, pp. 75-80. IEEE.

Komulainen, J., Hadid, A., Pietikäinen, M., Anjos, A. & Marcel, S. (2013). Complementary countermeasures for detecting scenic face spoofing attacks, in: *Biometrics (ICB), 2013 International Conference on*. 2013, pp. 1-7. IEEE.

Kose, N. & Dugelay, J.-L. (2013a). On the Vulnerability of Face Recognition Systems to Spoofing Mask Attacks, in: *Acoustics, Speech and Signal Processing (ICASSP)*. May 26-31, 2013a, Vancouver, BC, Canada, pp. 2357-2361. IEEE.

Kose, N. & Dugelay, J.-L., (2014). Mask Spoofing in Face Recognition and Countermeasures. *Image and Vision Computing, vol.* 32**,** pp**.** 779-789.

Kose, N. & Dugelay, J. L. (2013b). Countermeasure for the Protection of Face Recognition Systems Against Mask Attacks, in: *Automatic Face and Gesture Recognition (FG)*. April 22-26, 2013b, Shanghai, China, pp. 1-6. IEEE.

Kose, N. & Dugelay, J. L. (2013c). Reflectance Analysis Based Countermeasure Technique to Detect Face Mask Attacks, in: *Digital Signal Processing (DSP)*. July 1-3, 2013c, Fira, Greece, pp. 1-6. IEEE.

Lee, D.-w., Seo, K. & Min, B. (2006). Discrimination Between Cancer and Normal Tissue using Near Infrared Spectroscopy, in: *World Congress on Medical Physics and Biomedical Engineering*. Aug. 27 - Sept. 1, 2006, Seoul, South Korea, pp. 1341-1344. IEEE.

Li, L., Ng, C. S.-L., Mastorakis, N., Croitoru, A., Balas, V., Son, E. & Mladenov, V. (2009). A Physically-based Human Skin Reflection Model, in: *WSEAS International Conference. Proceedings. Mathematics and Computers in Science and Engineering*. March 23-25, 2009, Prague, Czech Republic, pp.: World Scientific and Engineering Academy and Society.

Liew, S. C. (n.d.) *Electromagnetic Waves. Centre for Remote Imaging, Sensing and Processing.* Online at https://crisp.nus.edu.sg/~research/tutorial/em.htm, accessed Jan 14 2017.

Lucas, J. (2015) *What is Visible Light?* Online at http://www.livescience.com/50678-visible-light.html, accessed 9 May 2017.

Määttä, J., Hadid, A. & Pietikäinen, M. (2011). Face spoofing Detection from Single Images Using Micro-texture Analysis, in: *Biometrics (IJCB)*. Oct. 11-13, 2011, Washington, DC, USA, pp. 1-7. IEEE.

Määttä, J., Hadid, A. & Pietikäinen, M., (2012). Face Spoofing Detection from Single Images using Texture and Local Shape Analysis. *IET biometrics*, *vol.* 1**,** pp**.** 3-10.

Macknojia, R., Chávez-Aragón, A., Payeur, P. & Laganière, R. (2012). Experimental Characterization of Two Generations of Kinect's Depth Sensors, in: *Robotic and Sensors Environments (ROSE)*. Nov. 16-18, 2012, Magdeburg, Germany, pp. 150-155. IEEE.

Madigan, J. (2017) *What Wavelength Goes With a Color?* Online at https://science-edu.larc.nasa.gov/EDDOCS/Wavelengths_for_Colors.html, accessed 12 April 2017.

Maechler, M., (2015). diptest: Hartigan's Dip Test Statistic for Unimodality—Corrected. *URL http://CRAN. R-project. org/package= diptest. R package version 0.75-7, vol.*

Mahendru, A. & Sarkar, M. (2012). Bio-inspired Object Classification Using Polarization Imaging, in: *Sensing Technology (ICST)*. Dec. 18-21, 2012, Kolkata, India, pp. 207-212. IEEE.

Matsubara, A., (2012). Differences in the Surface and Subsurface Reflection Characteristics of Facial Skin by Age Group. *Skin Research and Technology*, *vol.* 18**,** pp**.** 29-35.

Matsubara, A., Liang, Z., Sato, Y. & Uchikawa, K., (2012). Analysis of human perception of facial skin radiance by means of image histogram parameters of surface and subsurface reflections from the skin. *Skin Research and Technology*, *vol.* 18**,** pp**.** 265-271.

Matt. (2012) *The Difference Between Matt and Semi Gloss Finish Photo Paper.* Online at http://www.photopaperdirect.com/blog/?p=405, accessed 5 February 2017.

McHugh, S. (2005) *Cambridge in Colour: Noise Reduction by Image Averaging.* Online at http://www.cambridgeincolour.com/tutorials/image-averaging-noise.htm, accessed Oct 16 2015.

Meglinski, I. V. & Matcher, S. J., (2002). Quantitative assessment of skin layers absorption and skin reflectance spectra simulation in the visible and near-infrared spectral regions. *Physiological measurement*, *vol.* 23**,** pp**.** 741.

Nasr, A. H. (n.d) *In Vitro and in Vivo.* Online at http://science.jrank.org/pages/3541/In-Vitro-in-Vivo.html, accessed 1 April 2017.

Nave, C. R. (2012) *Classification of Polarization.* Online at http://hyperphysics.phy-astr.gsu.edu/hbase/phyopt/polclas.html, accessed 10 September 2016.

Nayar, S., Ramamoorthi, R. & Hanrahan, P. (n.d.) *Materials and Surface Appearance.* Online at http://www.cs.cmu.edu/afs/cs/academic/class/15462-f10/www/lec_slides/lec09.pdf, accessed 4 March 2017.

Nayar, S. K., Fang, X. S. & Boult, T. (1993). Removal of specularities using color and polarization, in: *Computer Vision and Pattern Recognition, 1993. Proceedings CVPR '93., 1993 IEEE Computer Society Conference on*. 15-17 Jun 1993, 1993, pp. 583-590.

Nixon, K., Aimale, V. & Rowe, R., (2008). Spoof detection schemes. *Handbook of biometrics, vol.***,** pp**.** 403-423.

Nunez, A. S. & Mendenhall, M. J. (2008). Detection of Human Skin in Near Infrared Hyperspectral Imagery, in: *Geoscience and Remote Sensing Symposium, IGARSS*. July 7-11, 2008, Boston, MA, USA, pp. II-621-II-624. IEEE.

Pan, G., Sun, L., Wu, Z. & Lao, S. (2007). Eyeblink-based Anti-spoofing in Face Recognition from a Generic Webcamera, in: *Computer Vision (ICCV)*. Oct. 14-21, 2007, Rio de Janeiro, Brazil, pp. 1-8. IEEE.

Pasquini, C., (2003). Near Infrared Spectroscopy: Fundamentals, Practical Aspects and Analytical Applications. *Journal of the Brazilian Chemical Society, vol.* 14**,** pp**.** 198-219.

Pfister, R., Schwarz, K. A., Janczyk, M., Dale, R. & Freeman, J., (2013). Good things peak in pairs: a note on the bimodality coefficient. *Frontiers in psychology, vol.* 4**,** pp**.** 700.

Polarizers. (n.d.) *Polarizers.* Online at http://opticalfiltersusa.com/polarisers.html, accessed Jan 17 2015.

Rudd, E. M., Günther, M. & Boult, T. E. (2016). PARAPH: Presentation Attack Rejection by Analyzing Polarization Hypotheses, in: *Computer Vision and Pattern Recognition Workshops (CVPRW)*. June 26 - July 1 2016, Las Vegas, USA, pp. 171-178. IEEE.

Ryer, A. (1997). *Light measurement handbook,* Newburyport, United States of America: International Light.

Sarkar, M., Bello, D. S. S. S. S., Van Hoof, C. & Theuwissen, A., (2011). Integrated Polarization Analyzing CMOS Image Sensor for Material Classification. *IEEE Sensors Journal, vol.* 11**,** pp**.** 1692-1703.

Schwartz, W. R., Rocha, A. & Pedrini, H. (2011). Face Spoofing Detection Through Partial Least Squares and Low-level Descriptors, in: *Biometrics (IJCB)*. Oct. 11-13, 2011, Washington, DC, USA, pp. 1-8. IEEE.

Shao, X., Zheng, W. & Huang, Z., (2010). Polarized Near-infrared Autofluorescence Imaging Combined with Near-infrared Diffuse Reflectance Imaging for Improving Colonic Cancer Detection. *Optics express, vol.* 18**,** pp**.** 24293-24300.

Singh, A., Tiwari, S. & Singh, S. K., (2013). Face Tampering Detection from Single Face Image using Gradient Method. *International Journal of Security and its Applications (IJSIA), vol.* 7.

Singh, M. & Arora, A., (2017). A Robust Anti-spoofing Technique for Face Liveness Detection with Morphological Operations. *Optik-International Journal for Light and Electron Optics, vol.* 139**,** pp**.** 347-354.

Sirohi, R. S. (1993). *Wave Optics and Its Applications*, Hyderabad, India: Orient Longman Limited.

So-Ling, C. & Ling, L. (2001). A Multi-layered Reflection Model of Natural Human Skin, in: *Computer Graphics International*. July 6, 2001, Hong Kong, China, pp. 249-256. IEEE.

Steiner, H., Kolb, A. & Jung, N. (2016). Reliable Face Anti-spoofing using Multispectral SWIR Imaging, in: *International Conference on Biometrics (ICB)*. June 13-16, 2016, Halmstad, Sweden, pp. 1-8. IEEE.

Sullivan, R. W., Ryzewski, M., Holland, M. G. & Marraffa, J. M., (2013). Compounded ointment results in severe toxicity in a pediatric patient. *Pediatric emergency care, vol.* 29**,** pp**.** 1220-1222.

Taylor, C. (2017) *What is Skewness in Statistics?* Online at https://www.thoughtco.com/what-is-skewness-in-statistics-3126242, accessed Jun 23 2017.

Tronci, R., Muntoni, D., Fadda, G., Pili, M., Sirena, N., Murgia, G., Ristori, M., Ricerche, S. & Roli, F. (2011). Fusion of Multiple Clues for Photo-attack Detection in Face Recognition Systems, in: *International Joint Conference on Biometrics (IJCB)*. Oct. 11-13, 2011, Washington, DC, USA, pp. 1-6. IEEE.

Vandergriff, L. J., (2008). Nature and properties of light. *Fundamentals of Photonics, vol.***,** pp**.** 1-38.

Wang, T., Yang, J., Lei, Z., Liao, S. & Li, S. Z. (2013). Face Liveness Detection using 3D Structure Recovered from a Single Camera, in: *International Conference on Biometrics (ICB)*. June 4-7, 2013, Madrid, Spain, pp. 1-6. IEEE.

Wang, W. B., Ali, J. H., Alfano, R. R., Vitenson, J. H. & Lombardo, J. M., (2003). Spectral Polarization Imaging of Human Rectum-membrane-prostate Tissues. *IEEE Journal of selected topics in quantum electronics, vol.* 9**,** pp**.** 288-293.

Wen, D., Han, H. & Jain, A. K., (2015). Face Spoof Detection With Image Distortion Analysis. *IEEE Transactions on Information Forensics and Security, vol.* 10**,** pp**.** 746-761.

Wolff, L. B. (1989). Using Polarization to Separate Reflection Components, in: *Computer Vision and Pattern Recognition*. June 4-8, 1989, San Diego, CA, USA, pp. 363-369. IEEE Computer Society Conference.

Wolff, L. B., (1990). Polarization-based Material Classification from Specular Reflection. *Pattern Analysis and Machine Intelligence, vol.* 12**,** pp**.** 1059-1071.

Wolff, L. B. & Boult, T. E., (1991). Constraining Object Features Using a Polarization Reflectance Model. *IEEE Transactions on Pattern Analysis and Machine Intelligence, vol.* 13**,** pp**.** 635-657.

Xia, G. (2014) *Polarization (Fresnel-Arago Laws).* Online at http://www.hep.manchester.ac.uk/u/xiaguo/waveoptics/Polarisation_supplement.pdf, accessed 15 January 2017.

Yan, J., Zhang, Z., Lei, Z., Yi, D. & Li, S. Z. (2012). Face Liveness Detection by Exploring Multiple Scenic Clues, in: *12th International Conference on Control Automation Robotics & Vision (ICARCV)*. Dec 5-7, 2012, Guangzhou, China, pp. 188-193. IEEE.

Yule, J. & Nielsen, W. (1951). The penetration of light into paper and its effect on halftone reproduction, in: *Proc. TAGA*. 1951, pp. 65-76.

Zaidi, Z., (2016). Characteristics of skin colour. *JPMA. The Journal of the Pakistan Medical Association, vol.* 66**,** pp**.** 914.

Zhang, Y., Chen, Y., Yu, Y., Xue, X., Tuchin, V. V. & Zhu, D., (2013). Visible and Near-infrared Spectroscopy for Distinguishing Malignant Tumor Tissue from Benign Tumor and Normal Breast Tissues In Vitro. *Journal of Biomedical Optics, vol.* 18.

Zhang, Z., Yi, D., Lei, Z. & Li, S. Z. (2011). Face Liveness Detection by Learning Multispectral Reflectance Distributions, in: *Automatic Face & Gesture Recognition and Workshops (FG 2011)*. March 21-25, 2011, Santa Barbara, CA, USA, pp. 436-441. IEEE.

Zhao, Y., Yi, C., Kong, S. G., Pan, Q. & Cheng, Y. (2016). *Multi-band Polarization Imaging and Applications,* Berlin Heidelberg: National Defense Industry Press and Springer.

Zitova, B. & Flusser, J., (2003). Image Registration Methods: A Survey. *Image and Vision Computing, vol.* 21**,** pp**.** 977-1000.

Appendix A

On Evaluation of Depth Accuracy in Consumer Depth Sensors

Published in Proceedings Volume 9875

Eight International Conference on Machine Vision (ICMV 2015)

Barcelona, Spain

December 2015

Appendix B

Face Anti-Spoofing Countermeasure: Efficient 2D Materials Classification Using Polarization Imaging

5th International Workshop on Biometrics and Forensics (IWBF)

Coventry, United Kingdom

4-5 April 2017